INFORMATION TO USERS

This manuscript has been reproduced from the microfilm master. UMI films the text directly from the original or copy submitted. Thus, some thesis and dissertation copies are in typewriter face, while others may be from any type of computer printer.

The quality of this reproduction is dependent upon the quality of the copy submitted. Broken or indistinct print, colored or poor quality illustrations and photographs, print bleedthrough, substandard margins, and improper alignment can adversely affect reproduction.

In the unlikely event that the author did not send UMI a complete manuscript and there are missing pages, these will be noted. Also, if unauthorized copyright material had to be removed, a note will indicate the deletion.

Oversize materials (e.g., maps, drawings, charts) are reproduced by sectioning the original, beginning at the upper left-hand corner and continuing from left to right in equal sections with small overlaps.

Photographs included in the original manuscript have been reproduced xerographically in this copy. Higher quality 6" x 9" black and white photographic prints are available for any photographs or illustrations appearing in this copy for an additional charge. Contact UMI directly to order.

ProQuest Information and Learning
300 North Zeeb Road, Ann Arbor, MI 48106-1346 USA
800-521-0600

UMI®

THE PHYSICAL VOLCANOLOGY AND PETROLOGY OF THE 3400 YBP CALDERA-FORMING ERUPTION OF ANIAKCHAK VOLCANO, ALASKA

A

DISSERTATION

Presented to the Faculty

of the University of Alaska Fairbanks

in Partial Fulfillment of the Requirements

for the Degree of

DOCTOR OF PHILOSOPHY

by

Scott Travis Dreher, B.A., B.S., M.S

Fairbanks, Alaska

May 2002

UMI Number: 3053228

UMI Microform 3053228

ProQuest Information and Learning Company
300 North Zeeb Road
P.O. Box 1346
Ann Arbor, MI 48106-1346

THE PHYSICAL VOLCANOLOGY AND PETROLOGY OF THE 3400 YBP CALDERA-FORMING ERUPTION OF ANIAKCHAK VOLCANO, ALASKA

By

Scott Travis Dreher

RECOMMENDED:

Advisory Committee Chair

Department Head

APPROVED:

Dean, College of Sciences, Engineering, and Mathematics

Dean of the Graduate School

4-16-02

Date

Abstract

Zoned ignimbrites are often interpreted as overturned "snapshots" of a compositionally zoned magma chamber. While ignimbrite zonation requires the spatial and temporal coexistence of diverse magmas, the origin of both the zonation and the diversity are poorly understood. While many studies have developed *in situ* differentiation models, these models do not explain composition gaps, commonly observed in the ignimbrites.

Aniakchak Caldera on the Alaska Peninsula was formed approximately 3,400 years ago. The eruption began with a plinian phase that deposited a thin rhyodacitic pumice fall deposit, and valley-filling rhyodacitic ignimbrites. A second phase is represented by a massive ignimbrite sheet (probably resulting from column collapse) comprising both rhyodacite and andesite. The eruption culminated in the collapse of the volcanic edifice and the deposition of a lithic-rich andesitic ignimbrite.

The andesite (~60 wt. % SiO_2) emplaced in the caldera-forming eruption, appears to have been produced by magma mixing. Although crystal-poor (~8 wt. % crystals), the andesite contains a bimodal plagioclase population and rare grains of both quartz and olivine. Self-contamination, wherein residual liquids from a crystallizing marginal boundary layer are reincorporated into the hybrid magma during successive basalt or rhyodacite injections, probably led to deviations from a binary mixing trend. The rhyodacite (~70 wt. % SiO_2), the most silicic magma erupted at Aniakchak is also crystal-poor (~2 wt. % crystals), but contains a single plagioclase population. The crystal poor

nature, simple mineralogy, and silicic composition of the rhyodacite imply an uncomplicated history. Geochemical models indicate partial melting of mafic plutons and fractional crystallization of a basaltic magma contributed to the rhyodacite erupted in caldera-forming eruption.

It appears that the andesitic composition was maintained by repeated injections of small volumes of both basaltic and rhyodacitic magmas. Each successive mixing event induced an increment of self-contamination in the andesite chamber. Increased pressure associated with an unusually large influx of rhyodacite, however, immediately induced an eruption, before significant mixing occurred. After the rhyodacitic magma was evacuated, and now destabilized the roof collapsed, leading to the eruption of the residence andesite.

Table of Contents

List Of Figures

List of Tables

Acknowledgments

No one has been more generous and enthusiastic about this work over the last six years than my advisor, Dr. John Eichelberger. From him, I have learned the value of creativity in scientific progress. My other committee members, Drs. Jim Beget, Mary Keskinen, and Chris Nye, have likewise offered invaluable assistance towards my completion of this research.

I would like to thank Dr. Tom Miller and Dr. Charles Bacon for indispensable field assistance and instruction. Their willingness to point me in the right direction is certainly appreciated. Dr. Jessica Larsen and Dr. Michelle Coombs also contributed a great deal in the field as well as offering insights into the petrology of Aniakchak volcano. Charles Bacon, Tina Neal, and Chris Nye graciously shared their pre-caldera and post-caldera data with me for comparison to the caldera-forming eruption products. My own data is much more meaningful in light of their contributions. This work was funded by the U. S. Geological Survey through the Alaska Volcano Observatory.

To my friends and fellow students, Darren Chertkoff, Michelle Coombs, Pavel Izbekov, Pete Stelling, and Lovro Valcic, your friendship is priceless. Jackie Caplan-Auerbach taught me to throw darts, which is probably the lynch pin in this whole thing.

I would be remiss if I neglected to thank my parents, Gary and Eulonda Dreher, who have loved me and supported me through many trials. Finally, to Catherine, the love of my life, thank you for helping me to see that unanswered questions are often better than unquestioned answers.

Chapter 1: Overview and Scope

Aniakchak Volcano, a roughly circular caldera 10 km in diameter, is located at 56.91 north latitude, 158.13 west longitude near the village of Meshik, Alaska. The caldera was explored extensively by Bernard Hubbard in 1930 just prior to its most recent eruption in 1931. The caldera was formed approximately 3400 years ago (Miller and Smith, 1987), in an eruption that also produced an extensive ignimbrite. The ignimbrite produced in the caldera-forming eruption (CFE) contains both rhyodacite (SiO_2 ~ 70 wt. %) and andesite (SiO_2 ~ 60 wt. %), but no intermediate hybrid. Little detailed work has been done to describe the CFE ignimbrite, or to reconstruct the timing of the caldera-forming event.

The ignimbrite sequence from the caldera-forming event comprises three separate units, and overlies a small-volume fall deposit. The stratigraphically lowest parts of the ignimbrite are composed of valley-confined rhyodacitic pyroclastic flow deposits. These are followed by a thick massive mixed ignimbrite, which contains both rhyodacite and andesite pumice. Finally, a lithic-rich andesite ignimbrite makes up the top portion of the ignimbrite package.

The goal of chapter 2 is to describe the extents and distributions as well as the juvenile and lithic componentry of the rhyodacite, mixed, and andesite ignimbrite units. These data are then used to develop an account of the caldera-forming eruption.

Chapter 3 investigates the petrology of the CFE andesite magma. Mineralogical and geochemical evidence suggest that the CFE andesite is a hybrid magma produced by mixing of basalt and rhyodacite. However, some chemical components show significant deviations from a binary mixing trend which must be

explained. Several options are explored, including a mixing end member with unusual composition, and which was never actually erupted independently or addition of an excess fluid. These however are found to be insufficient. A mechanism of mixing-induced self-contamination is then developed, in which intrusion of a new pulse of rhyodacite or basalt into the andesite chamber leads to the expulsion of interstitial liquids from a crystallizing boundary layer.

The petrology of the CFE rhyodacite is presented in chapter 4. The CFE rhyodacite composition is not well explained by fractional crystallization from the CFE andesite. Furthermore, the CFE rhyodacite is interpreted to have separated from its source and erupted with little modification, but colliding with eth CFE andesite in the process. Several late precaldera rhyodacite lavas and tephras are described as well. These rocks are constrained stratigraphically between an older andesite ignimbrite thought to be around 8000 years old and the CFE ignimbrite. The compositions of these rhyodacite units are distinct from each other, implying several independent sites of rhyodacite genesis. Geochemical modeling allows both fractional crystallization of high-alumina basalt (HAB) and partial melting of a young mafic pluton as possible mechanisms for producing the CFE rhyodacite. A model is developed, then, in which both basalt and rhyodacite periodically ascend into the shallow crust and mix with the resident andesite, maintaining the andesitic composition of the shallow magma body. Small additions may be insufficient to cause an eruption, thus allowing time for mixing. An unusually large influx of silicic magma, however, triggered the caldera-forming eruption immediately before mixing could occur. Representative major element analyses for CFE rhyodacite and andesite, as well as analyses of the late precaldera rhyodacites are given in table 1. Trace element data for these and all other

samples analyzed for this study can be found in appendix 1. Appendices 2 through 4 contain lists of microprobe analyses of plagioclase, pyroxenes, and Fe-Ti oxides, respectively. Appendix 5 gives locations and brief descriptions of field locations not mentioned explicitly in chapter 1.

The Aniakchak ignimbrite offers a superb opportunity to investigate the coexistence of chemically disparate magmas in both time and space. Historically, this type of magmatic coincidence has been interpreted as reflecting a zoned magma chamber, in which silicic liquids are derived from a more mafic parent through *in situ* crystallization. The silicic residual liquids are less dense, and rise to the top of the chamber to form a silicic cap (e.g., McBirney et al., 1985; Bacon and Druitt, 1988). The silicic portion, being at the top of the chamber, erupts first during an ingnimbrite eruption, followed by the denser, more mafic magma so that the ignimbrite is interpreted as an overturned snapshot of the magma chamber prior to eruption. The relationships between zoned chambers and zoned ignimbrites have become established in a circular manner: zoned ignimbrites are erupted from zoned chambers; zonation in the chamber then explains the chemical gradients in the ignimbrite. While it is clear that the two magmas contained in the CFE ignimbrite at Aniakchak must have been in the same chamber for at least a short period prior to the eruption, the idea of a long-lived zonation in a shallow chamber is questionable. Eichelberger et al. (2000) proposed that many zoned ignimbrites may represent the effects of "collisions" between independently formed magma bodies. Eichelberger and Izbekov (2000) further suggested that andesites are commonly the "normal" magma in shallow subduction-zone volcanic systems. According to this hypothesis, an andesite – rhyodacite eruption results when a rhyodacitic dike intersects a shallow andesite pod

(Eichelberger and Izbekov, 2000).

Magma mixing has been widely cited as the mechanism for intermediate magma formation in arc environments (e.g., Heiken and Eichelberger, 1980; Sakuyama, 1981; Brophy 1987; Schmitt et al., 2001). Recent studies of zoned ignimbrites in the Cascades (Conrey et al., 2001; Aubin et al., 2000) have documented not only a mixing origin for intermediate magmas in the ignimbrites, but have shown deviations from binary mixing trends similar to those observed in the Aniakchak CFE andesite. Notably, the Shevlin Park tuff (Conrey et al., 2001) and tuffs of the Deschutes Formation (Aubin et al., 2000), both in central Oregon have elevated phosphorus concentrations relative to a simple basalt – rhyolite mixture. These authors (Conrey et al., 2001; Aubin et al., 2000) have called upon various mechanisms of apatite addition to explain these chemical features, rather than mixing-induced self-contamination. In any event, the superimposition of secondary chemical processes over intermediate magma hybridization is not a feature peculiar to Aniakchak.

Table 1: representative major element analyses for Aniakchak ignimbrite and late precaldera rhyodacite pumice and lavas.

	AC-37A	99AC55	ACAF1A1	ACAF1A4	ACAF1E2
Lat.	57.05N	56.84N	56.88N	56.88N	56.88N
Long.	158.61W	158.19W	157.87W	157.87W	157.87W
Rock Unit	RD Fall	RD Ignim.	Mixed Ignim.	Mixed Ignim.	And. Ignim.
Rock Type	Rhyodacite	Rhyodacite	Rhyodacite	Andesite	Andesite
SiO2	69.19	68.76	69.27	58.97	58.82
TiO2	0.52	0.53	0.54	1.30	1.34
Al2O3	15.01	14.98	15.16	16.27	16.25
FeO	2.10	1.97	2.10	5.85	6.51
Fe2O3	0.54	0.51	0.54	1.19	1.29
MnO	0.16	0.15	0.15	0.20	0.20
MgO	0.60	0.54	0.68	2.67	2.95
CaO	1.97	1.96	2.02	5.95	6.28
Na2O	5.27	5.33	5.49	4.52	4.37
K2O	2.91	2.96	2.93	1.63	1.52
P2O5	0.11	0.10	0.12	0.55	0.55
Total	98.38	97.80	99.00	99.10	100.08
FeO/MgO	2.19	2.29	1.93	1.34	1.35
Mg#	0.34	0.33	0.37	0.45	0.45

	97AC-14	97AC-19	97AC-22	97ANB45	99AC26
Lat.	56.92N	56.92N	56.94N	56.93N	56.94N
Long.	158.10W	158.10W	158.01W	158.26W	158.01W
Rock Unit	Precald. Pum.	Precald. Pum.	Precald. Lava	Precald. Lava	Precald. Lava
Rock Type	Rhyodacite	Rhyodacite	Rhyodacite	Rhyodacite	Rhyodacite
SiO2	68.48	67.21	67.55	67.88	68.76
TiO2	0.73	0.85	0.83	0.71	0.69
Al2O3	14.87	15.37	15.53	15.35	14.81
FeO	3.26	3.46	3.50	3.28	3.38
Fe2O3	0.49	0.68	0.28	0.32	0.28
MnO	0.16	0.17	0.15	0.15	0.16
MgO	0.74	1.01	1.10	0.85	0.69
CaO	2.30	2.87	2.85	3.01	2.25
Na2O	5.20	5.24	5.10	4.92	5.21
K2O	2.98	2.73	2.98	2.63	3.09
P2O5	0.16	0.22	0.21	0.18	0.14
Total	99.38	99.81	100.08	99.28	99.46
FeO/MgO	2.64	2.09	1.85	2.26	2.85
Mg#	0.29	0.34	0.36	0.32	0.27

Chapter 2: Physical Volcanology and Stratigraphy of the Caldera Forming Eruption

2.1 Introduction

Zoned ignimbrite sheets have often been interpreted as representing inverted snapshots of a magma chamber (e.g.,Bacon and Druitt, 1988; Hildreth, 1979). Whether or not this is actually the case has important implications for the generation of compositional diversity in magmatic systems. Petrologists tend to view such diversity as differentiation of a single parent with varying amounts of crustal influence. As pointed out recently by Eichelberger et al. (2000), however, petrographic and geochemical observations often suggest arrested processes of homogenization of separate batches of compositionally diverse magmas. The presence of banded pumices, for example, composed of the end-member magmas involved in a zoned ignimbrite eruption, along with the lack of any homogenized mixtures of the two melts, indicates a short time of contact between the end-members prior to eruption. Production of any significant volume of evolved liquid by crystallization differentiation is a slow affair, according to experimental and theoretical work (Huppert and Turner, 1981; Sparks et al., 1984). These works would predict a more gradual zonation from parent magma in the bottom of the chamber to evolved melt near the roof.

The presence of large compositional gaps within products of a single eruption, as in the Aniakchak caldera-forming eruption, presents a problem for crystallization differentiation as a means of petrogenesis of the silicic component. Alternatively, Eichelberger et al. (2000) suggest the plausibility of catastrophic intrusion of silicic

magma from below into a more mafic resident magma, not only as the mechanism for juxtaposing contrasting magmas without creating a hybrid component, but also as the reason behind cataclysmic caldera-forming eruptions.

In addition to providing the focus for important work concerning the distribution and emplacement mechanisms of the caldera-forming eruption ignimbrites by Miller and Smith (1977), Aniakchak continues to garner interest from a volcano-monitoring standpoint as well. Its proximity to international air routes and demonstrated ability to erupt explosively, most recently in 1931, makes understanding its behavior, a clear consequence of its petrologic development, very important. Continued production of relatively silicic magmas throughout its post-caldera history makes this volcano one of the more hazardous volcanoes in the Aleutian Arc.

2.2 Geologic Setting

Aniakchak Volcano is a broad basalt to andesite shield located on the Alaska Peninsula (56.91N, 158.13E, see figure 1). A large, nearly circular caldera 10 km in diameter was formed ~3400 years BP (Miller and Smith, 1987). A United States Geological Survey party discovered the crater in August 1922 (Smith, 1925). Further detailed exploration by Bernard Hubbard revealed the active nature of the volcano (Hubbard, 1931). These early workers believed the crater to have been formed by explosion, rather than subsidence. The volume of lithic material in the ejecta surrounding the crater (~ 4 km^3, this study) is much too small to account for the missing volume of the volcano originally estimated by Smith (1925) to be around 15 cubic miles (~62 km^3). This discrepancy and analogy to Crater Lake Caldera, Oregon (Bacon, 1983), leaves little doubt that Aniakchak Caldera was formed by collapse of

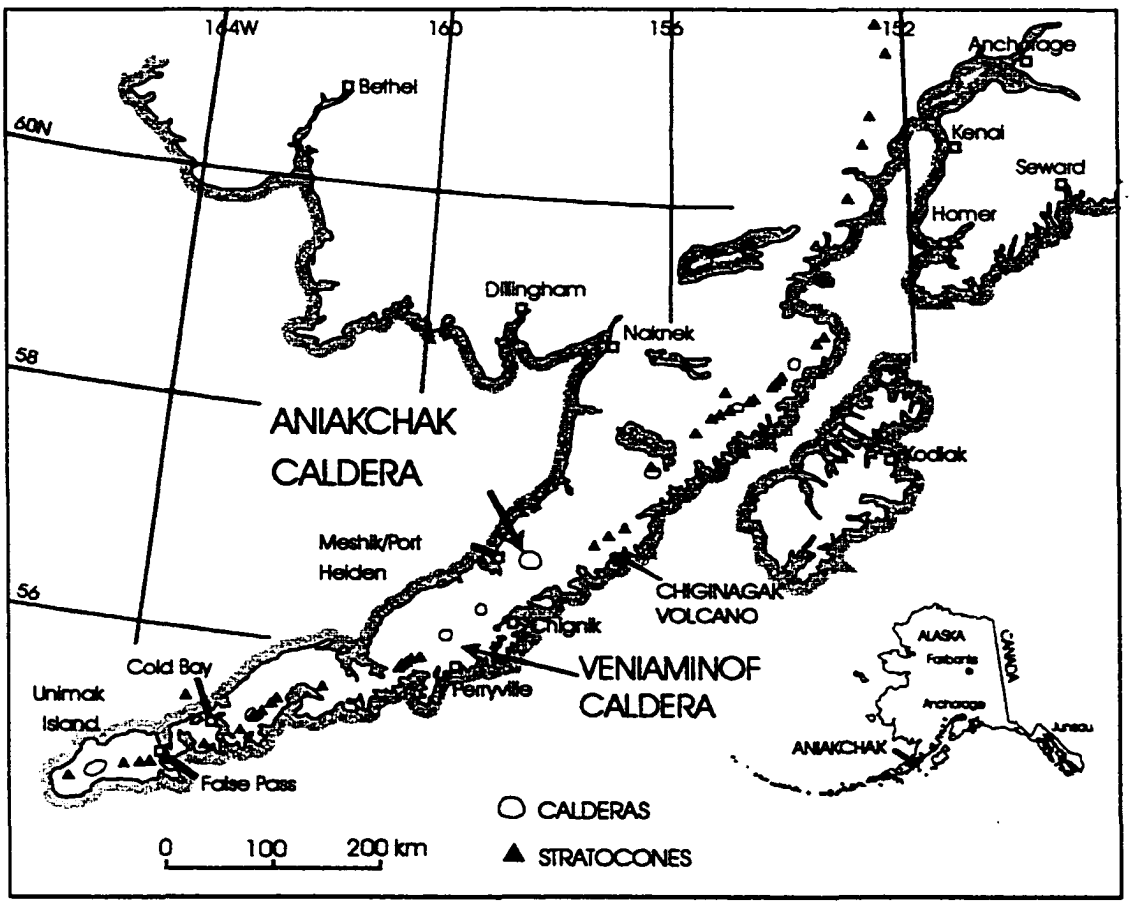

Figure 1: Map of the Alaska Peninsula showing the location of Aniakchak Caldera.

the volcanic edifice.

The caldera-forming eruption (CFE) resulted in the deposition of a layered ignimbrite, in which successive zones of rhyodacite, rhyodacite/andesite, and andesite are in sharp contact. This event produced the most silicic (~70 wt.% SiO_2) material associated with the volcano along with "normal" andesite (~60 wt.% SiO_2). Some mingling of the two magmas produced banded pumice; no intermediate hybrid (i.e., thoroughly mixed rather than mingled) pumice associated with the CFE has been discovered.

Pre-caldera lavas reveal a fluctuation from an initially calc-alkaline magmatic system to a tholeiitic system and back again to its present calc-alkaline state (Nye et al., 1993). Post-caldera pumices and lavas range continuously from 53 wt.% SiO_2 to 68 wt.% SiO_2 (Bacon et al., 1997b). Post-caldera activity has been extensive, with numerous pumice domes, maars, cinder cones, and composite cones including Vent Mountain, which rises nearly 500 m from the caldera floor. The most recent eruption took place in 1931 from a vent or vents near the base of the west wall inside the caldera.

Underlying earliest cone-building lavas at Aniakchak are Upper Jurassic and Lower Cretaceous sedimentary rocks (Detterman et al., 1981). Two stratigraphic units, the Naknek Formation and the Staniukovich Formation are exposed in the inner caldera walls in thicknesses equal to the thickness of the volcanic edifice in some places (Detterman et al., 1981). Jurassic plutonism, the earliest recognized widespread episode of magmatic activity on the Alaska Peninsula (Reed and Lanphere, 1973), is represented in the vicinity of Aniakchak by large granodioritic cobbles in Naknek conglomerate. Large boulders of Naknek conglomerate were included in lithic

breccias deposited on the caldera rim, presumably during caldera formation. The large size of the included plutonic clasts suggests a short transport distance from the sediment source, making it reasonable to assume that the Alaska-Aleutian Range Batholith described by Reed and Lanphere (1970; 1973) is present in the basement beneath Aniakchak. Naknek-derived arkosic sandstones have been found down most of the length of the Alaska Peninsula (McLean, 1979), suggesting the presence of granitic rocks in the subsurface. Deposits of the Eocene to Miocene Meshik volcanic arc are exposed around the southeast half of the present Aniakchak crater (Wilson, 1985). A relatively flat gentle slope forms the area to the northwest between Aniakchak and the Bering Sea. The northeast trending Aleutian Range stands between the southwest flank of the caldera and the Pacific Ocean. Aniakchak is situated approximately 25 km northwest of the axis of the Aleutian Range. Mt. Chiginagak, northeast of Aniakchak, and Mt. Veniaminof, southwest of Aniakchak are both on the Aleutian Range axis (figure 1).

2.3 Stratigraphy and Field Observations

The formation of Aniakchak Caldera was accompanied by the eruption of approximately 65 km^3 of tephra (bulk volume, see below), mostly as ignimbrites. Half of the tephra is rhyodacitic in composition, the remainder andesitic. The caldera is 10 km across, nearly circular and averaging 0.5 km in depth (Miller and Smith, 1987). The ignimbrites traveled to both the Bering Sea to the northwest and to the Pacific Ocean to the southeast. Ignimbrite can also be found in some (but not all) mountain passes between the caldera and the Pacific coast. Miller and Smith (1977) cited these observations as evidence that these ignimbrites originated from dense, momentum-

driven pyroclastic flows, rather than an expanded, low-density cloud. New data concerning the stratigraphy and componentry of the ignimbrite deposits as well as chemistry of the component magmas have been obtained, allowing a more detailed inference of the eruptive sequence and pre-eruptive state of the magmatic system. Sieving bulk samples of ignimbrite material, and separating and weighing the 8 mm and larger fractions into rhyodacite, andesite, and lithic groups was done to determine the componentry of deposits. Enough material was collected at each location so that no single clast accounted for more than a few percent of the volume of the sample. Sieving of 64 mm, 32 mm, 16mm, and 8mm sizes was done in the field. The remaining finer portion was retained, although large samples were quartered or eighthed. These were sieved at the University of Alaska Fairbanks Geophysical Institute through sieves with mesh sizes of 1.18 mm, 600 microns, 250 microns, 150 microns, and 75 microns.

Locations of described stratigraphic sections are shown in figure 2. Latitude and Longitude for each of the 8 numbered sections are given in table 2. A generalized cross section of the CFE ignimbrite (fig 3) begins with a relatively thin, lithic-poor fall unit composed entirely of rhyodacitic pumice. The base of the overlying ignimbrite sequence is also composed exclusively of rhyodacite and is lithic poor. The andesite-free section is typically several meters to tens of meters thick. Thick sections of mixed ignimbrite (i.e., ignimbrites comprising both andesite and rhyodacite as discrete clasts) are common at distances more than 10 km from the caldera. The overlying andesite ignimbrite is lithic rich, and virtually free of rhyodacite, except for small, very rounded lapilli that were likely recycled from the rhyodacite or mixed ignimbrites; in many proximal exposures, this portion of the ignimbrite is represented

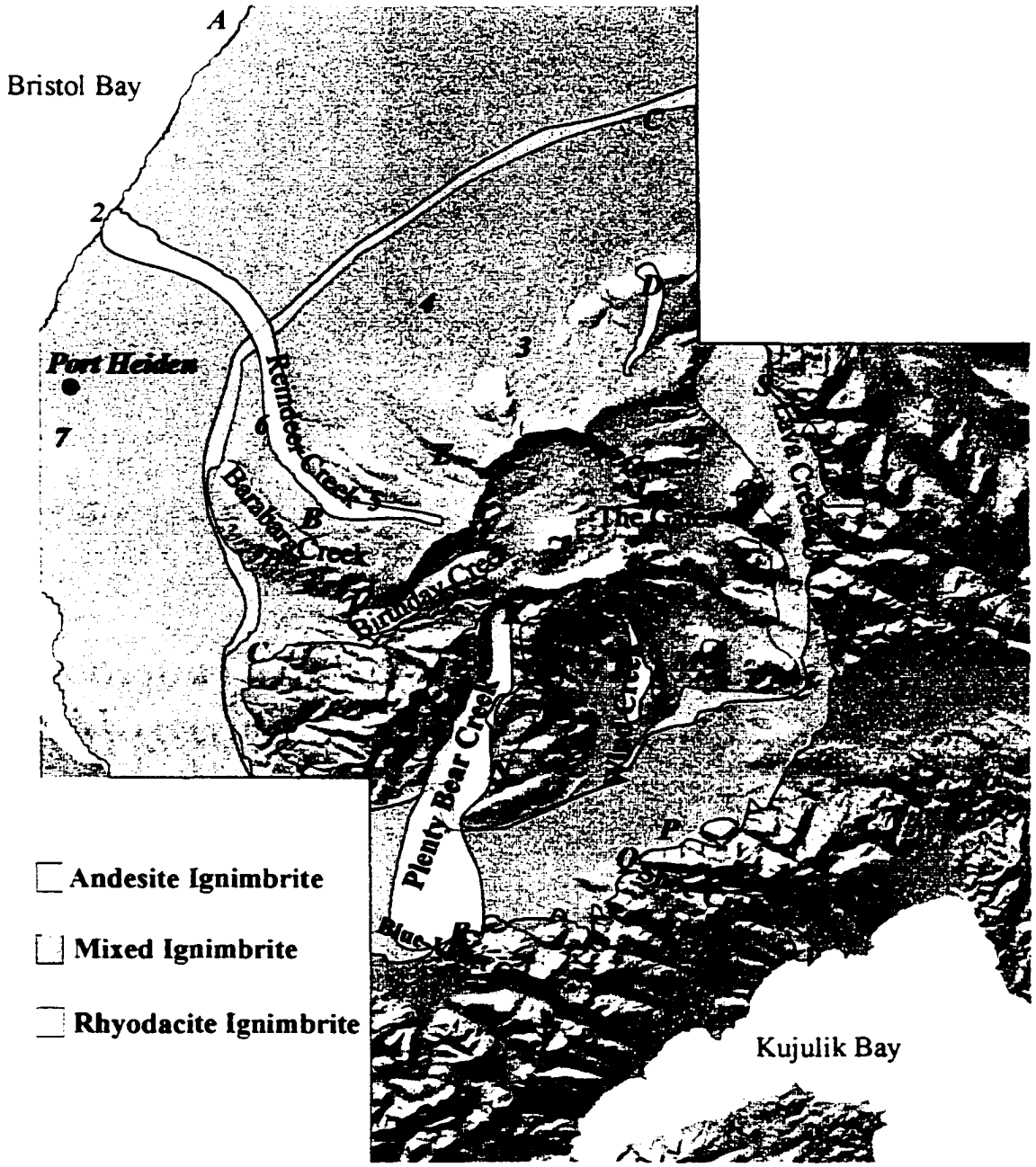

Figure 2: Digital elevation map of Aniakchak Caldera and vicinity. Numbers correspond to section numbers on figure 4. Letters mark locations of other sections detailed in Appendix 5.

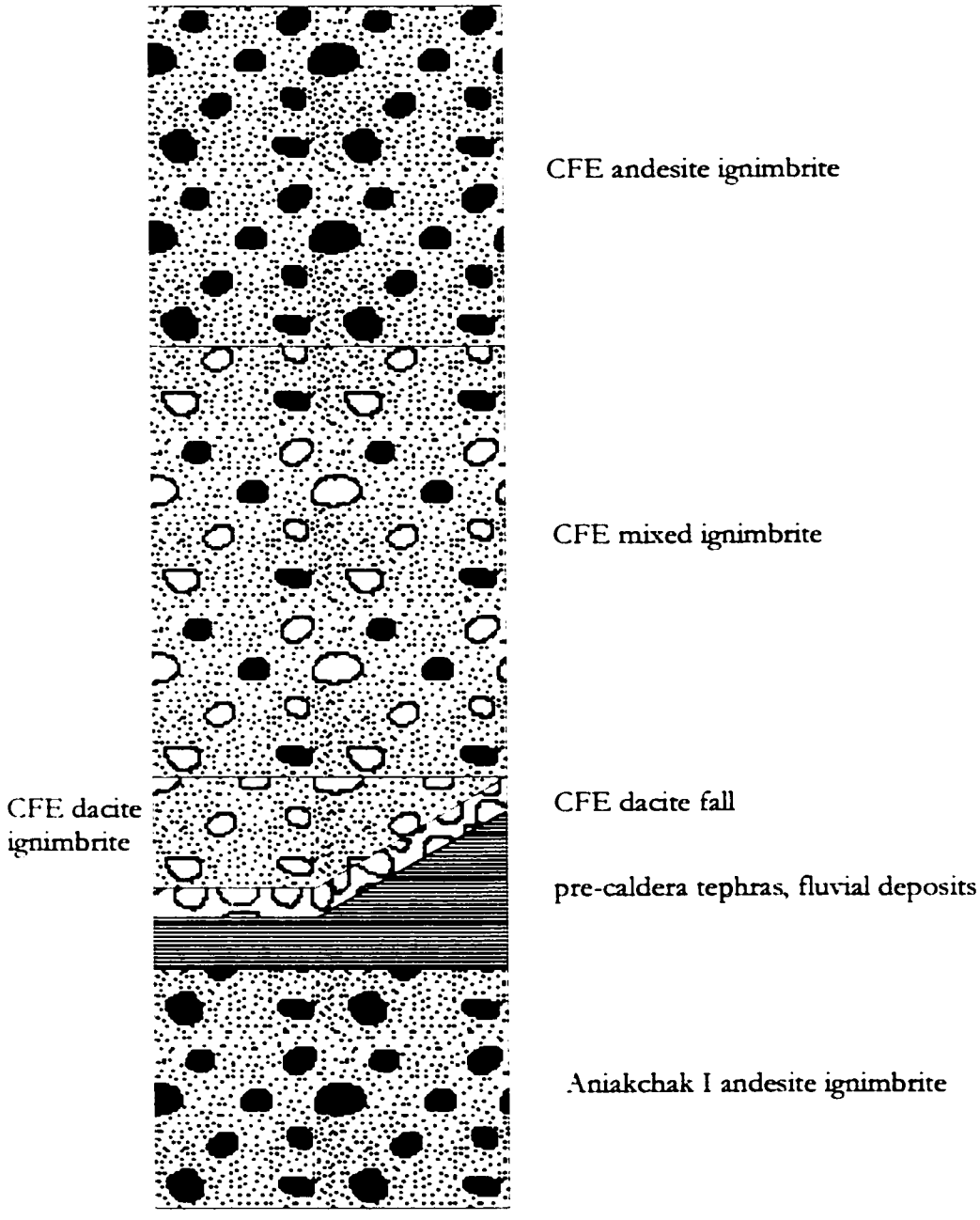

Figure 3: Generalized stratigraphic column of Aniakchak caldera forming eruption stratigraphy.

Table 2: Latitude and longitude of eight sections referred to in chapter 2 and shown on figure 2. Locations of remaining lettered sections on figure 2 are given in appendix 5.

Section	Latitude	Longitude
1	56.92N	158.10W
2	57.05N	158.61W
3	57.0N	158.16W
4	57.03N	158.25W
5	56.96N	158.39W
6	56.97N	158.43W
7	56.95N	158.62W
8	56.88N	157.87W

by a lithic breccia. All but one of the described sections contain abrupt transitions in the proportions of andesite to rhyodacite. Most exposures that contain both andesite and rhyodacite at the same stratigraphic level contain at least 25 percent andesite. For this reason, the term "mixed ignimbrite" will refer to ignimbrite exposures that are between 25 to 75 percent andesite. Rhyodacite ignimbrite will refer to exposures with less than 25 percent andesite, although most examples are completely free of andesite. Exposures that contain more than 75 percent andesite will be called andesite ignimbrite. An older andesite unit (Miller and Smith, 1987) is locally exposed in a stream gully north of the caldera, in the caldera walls, and in Birthday Creek Pass on the southeast caldera rim. In the north stream gully exposure, Aniakchak I ignimbrite is separated from CFE deposits by tephras from Black Peak and Veniaminof. Both of these volcanoes are to the south of Aniakchak, and the older of the two tephras, the Black Peak ash, has a ^{14}C age of about 4500 BP (Miller and Smith, 1987)

An immediately pre-caldera rhyodacite eruption is recorded in deposits on the

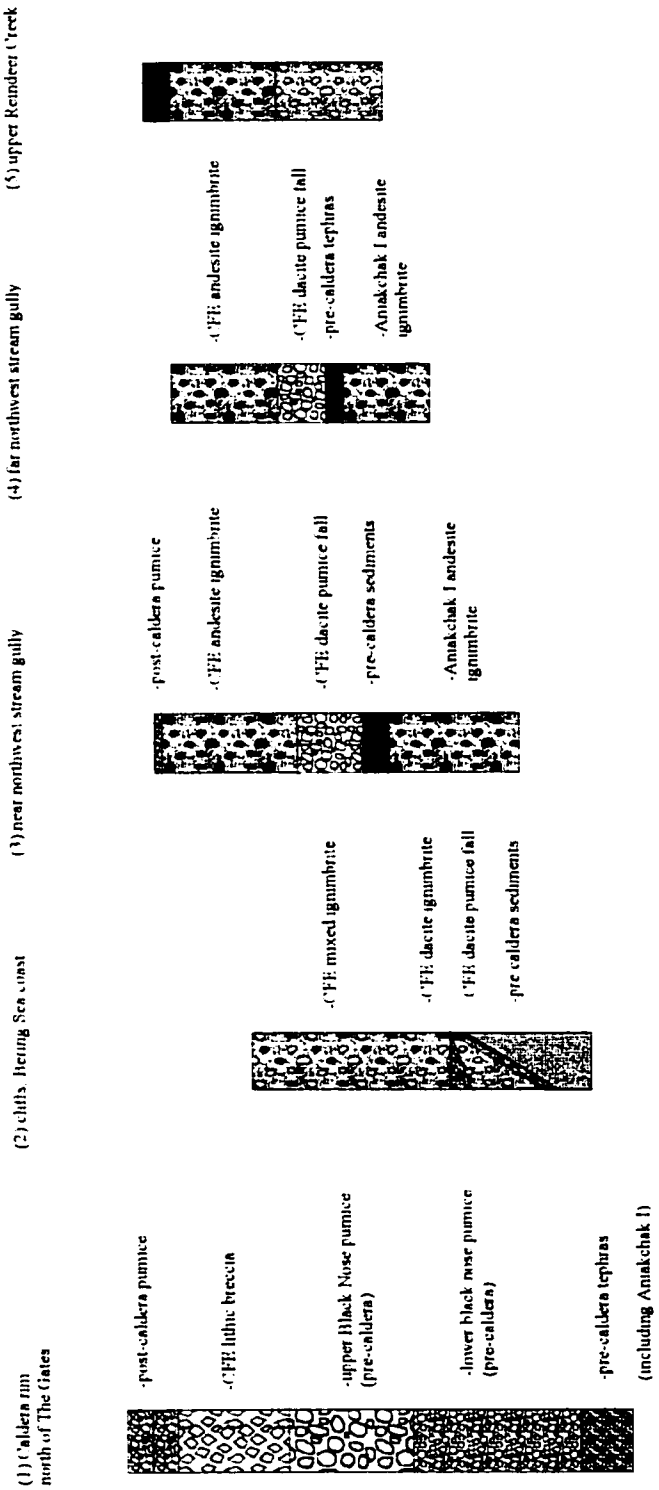

Figure 4: Correlation of described ignimbrite sections. Numbers at the left of section names correspond to numbered location on figure 2.

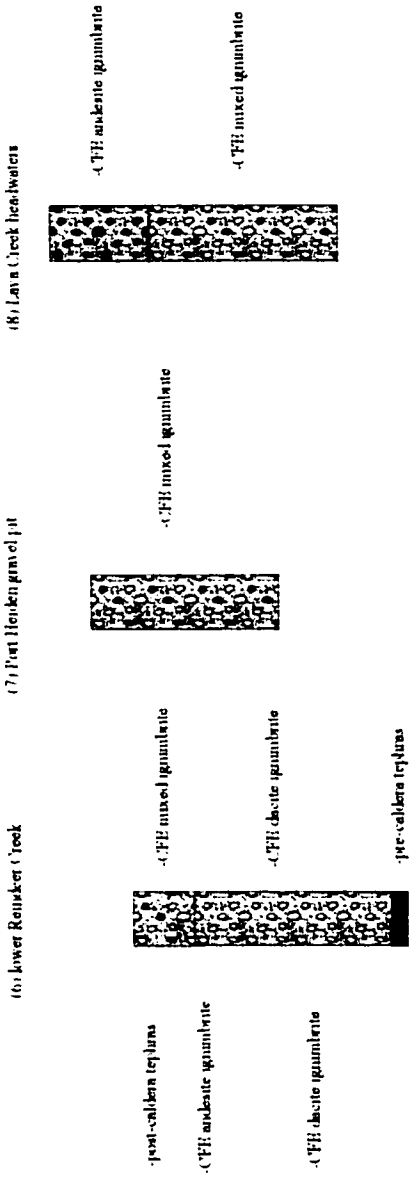

Figure 4. continued

east caldera rim north of The Gates (figure 4, section 1), where a >20 m thick section of rhyodacite fall is overlain by CFE lithic lag breccia. Although broadly similar to the CFE rhyodacites in bulk composition, this fall unit, herein referred to as the Black Nose Pumice, has higher abundances of FeO* and TiO_2 than well-established abundances in CFE rhyodacites, and lacks the trace amounts of hornblende present in CFE rhyodacites. The Black Nose Pumice overlies older, erosionally truncated pumice fall and flow layers, including an outcrop of agglutinated Aniakchak I andesite. The Black Nose Pumice fall consists of large pumices more than 30 cm in diameter. The lower half of the deposit consists of highly inflated, crystal-poor, buff-colored clasts with pink interiors. Most of the pumice blocks are fragile, easily breaking when removed from the deposit. The upper half of the layer is darker in color, and is more crystal rich. Chemical analyses, given in table 1 (97AC14: lower Black Nose pumice, 97AC19: upper blacknose pumice) show that these pumices are less evolved than CFE rhyodacite in terms of SiO_2 content, but are still considered rhyodacite. A densely welded pyroclastic flow was deposited concurrently with the deposition of the fall unit. Fiamme are present within a red oxidized welded matrix around the margins of this deposit. The degree of welding increases inward toward the center of the flow. A rhyodacite lava dome high in the caldera walls beneath the Black Nose Pumice has similar chemistry to the Black Nose Pumice. Two other rhyodacite flows were erupted onto the volcano flanks approximately 2 kilometers from the west-northwest rim and 5 kilometers from the northeast caldera rim. The northeast rhyodacite flow is directly overlain by CFE lithic breccia.

2.3.1 Fall Deposits

Exposures of CFE rhyodacite fall are restricted to the region to the north and northwest of the caldera. There is an excellent exposure 28 km west northwest of the caldera in the Bering Sea cliffs north of Pt. Heiden (figure 4, section 2). In this locality, the approximately 20-cm-thick fall deposit mantles preexisting topography. Pumice fragments are 3 to 5 cm in diameter and angular. The unit is laterally extensive throughout the cliffs in this area. Another two exposures are found northwest of the caldera, 7 and 10 km away, respectively. The more proximal of the two outcrops (figure 4, section 3) contains a 75-cm sequence of rhyodacite fall, which mantles preexisting topography. The lowermost 20 cm contain angular, buff colored pumice fragments that are mostly in the 1 to 2 cm size range, and very few lithics. Pumice size decreases upward to around 5 mm at the top of the unit. Lithic content increases slightly, but maximum lithic size is around 2 mm. The more distal of the two outcrops (figure 4, section 4) contains approximately 50 cm of buff colored, angular rhyodacite lapilli. Pumice fragments in this area are also 1 to 2 cm in size.

As discussed below, the volume of material deposited as pumice falls at Aniakchak appears to be small when compared to the volume of ignimbrite produced, although it is possible that a larger volume exists unexposed in the northern and western flats. This is unlike the 1912 eruption of Novarupta, in which the volume of fall deposits is more than 1.5 times that of the accompanying ignimbrites (Fierstein et al., 1997). Furthermore, all CFE fall deposits recognized on the flanks of Aniakchak volcano are exclusively rhyodacite. No fall deposits containing andesite have been discovered. Mixed rhyodacite and andesite ash has been reported on the Seward Peninsula in northwest Alaska and correlated to the CFE of Aniakchak, however

(Beget et al., 1992). The proportion of andesite in these far-removed deposits is between 10 and 20 % (J. Beget, pers. comm.), somewhat lower than observed proportions in mixed ignimbrites around the caldera. This observation is addressed later in this paper.

2.3.2 Rhyodacite Ignimbrites

Rhyodacite ignimbrites are found in a broad range of azimuths around the volcano, but are especially abundant in the deeply incised stream valleys on the south flanks, mostly at locations within 10 km of the caldera rim. Rhyodacite ignimbrites are well exposed in the heads of Plenty Bear and Wind Creeks, where the deposits are 30 to 40 meters thick, and overlain by lithic breccia with juvenile andesite. Birthday Creek also contains occasional outcrops of rhyodacite ignimbrite overlain by agglutinated CFE andesite ignimbrite. All of these exposures are thick, massive units with maximum pumice sizes around 20 cm. One small, 1.5 meter-thick outcrop of rhyodacite ignimbrite is found 26 km south of the caldera in Blue Violet Creek. The Blue-Violet Creek exposure contains complex layering, and may be a pyroclastic surge deposit. Alternatively, this outcrop may represent back-flow of a pyroclastic flow that failed to surmount the Aleutian Range. Small exposures of rhyodacite ignimbrites are observed 10 km north northeast of the caldera.

Although most rhyodacite ignimbrites have a restricted radial range, one deposit to the west-northwest extends from the caldera flanks to the Bering Sea cliffs in the Reindeer Creek channel. An exposure 12 km from the caldera (figure 4, section 5) reveals incipiently welded rhyodacite tuff at creek level. The degree of welding decreases up section. The rhyodacite tuff is 23 m thick at this location and is in sharp

contact with andesite ignimbrite. The mixed ignimbrite is absent. Large rhyodacite pumice fragments are often composite clasts as evidenced by relict clast boundaries visible in the interiors. These can have maximum dimensions of up to 20 cm. Lithics account for 8 to 13 wt. % of the clasts larger than 8 mm in the rhyodacite tuff, the balance being rhyodacite pumice fragments. The deposit is unsorted, and matrix supported; no stratification is present.

Four kilometers downstream, the base of the rhyodacite tuff is exposed (figure 4, section 6). The rhyodacite tuff overlies a 50-cm-thick fine lapilli (up to 1 cm) surge deposit. Between the surge and the rhyodacite tuff is a very thin dark-brown fine-grained tephra layer. The base of the tuff is nonwelded, unsorted, and contains pumice clasts up to a few centimeters. The deposit becomes progressively more welded and maximum clast size increases upward. The most highly welded portion forms vertical cliffs up to 3 meters thick. Pumice blocks in this section are as large as 20 cm in maximum dimension. Most pumice fragments in this portion of the tuff have been flattened so that aspect ratios are on the order of 1/2. Welding then decreases with height, until, at the top of the exposure, very little welding exists.

The most distal occurrence of this ignimbrite is exposed in the Bering Sea cliffs north of Pt. Heiden. In this location, a cross section of the rhyodacite tuff is exposed. The flow fills a preexisting channel in the underlying beach sediments, and is not laterally extensive. Maximum thickness is 2.5 m. Again, the tuff is unsorted, massive, and contains pumice fragments up to 6 cm. No welding has taken place at this location. This west-northwest rhyodacite pyroclastic flow is the largest of the four observed flows. It should be noted that other rhyodacite pyroclastic flows might be buried beneath the mixed ignimbrite.

2.3.3 Mixed Ignimbrite

The mixed ignimbrite can be found at nearly all azimuths around the caldera, and extends to both Bering and Pacific coasts. It is only found at distances greater than about 10 km, however. Only one outcrop 15 km southwest of the caldera in Barabara Creek contains mixed ignimbrite as a gradational contact between rhyodacite and andesite ignimbrites. All other instances of mixed ignimbrite are thick, massive, unsorted units. Gas escape pipes are common. Although both the top and bottom contacts of the mixed ignimbrite are rarely seen in a single outcrop, it is sharply overlain by andesite ignimbrite in the Lava Creek drainage 10 km to the east of the caldera (section 8 of figure 4 and figure 5).

At the Bering Sea coast north of Port Heiden, the mixed ignimbrite is tens of meters thick and forms a massive series of cliffs that extends at least 30 kilometers. Separation into three flow units, based on changes in grain size, is possible in the Bering Sea mixed ignimbrite. The bottom two thirds of the cliffs comprise unsorted nonstratified ignimbrite with pumice clasts 10 cm or more in diameter. Andesite accounts for 25% of the clasts larger than 8mm. The upper third of the cliff comprises an unsorted, nonstratified unit containing about 10% andesite. Pumice fragments are up to 3 cm in diameter. An exposure in a gravel pit in Pt. Heiden (figure 4, section 7) displays similar stratification, although the base of the lower unit is not exposed. In this gravel pit exposure, gas escape pipes beginning both in the lower and middle unit are truncated at the top of the middle unit. The top unit is a reversely zoned ignimbrite containing 30% andesite. Pumice fragments up to 6 cm occur in the top unit.

To the north and west of the caldera, where the previously described outcrops

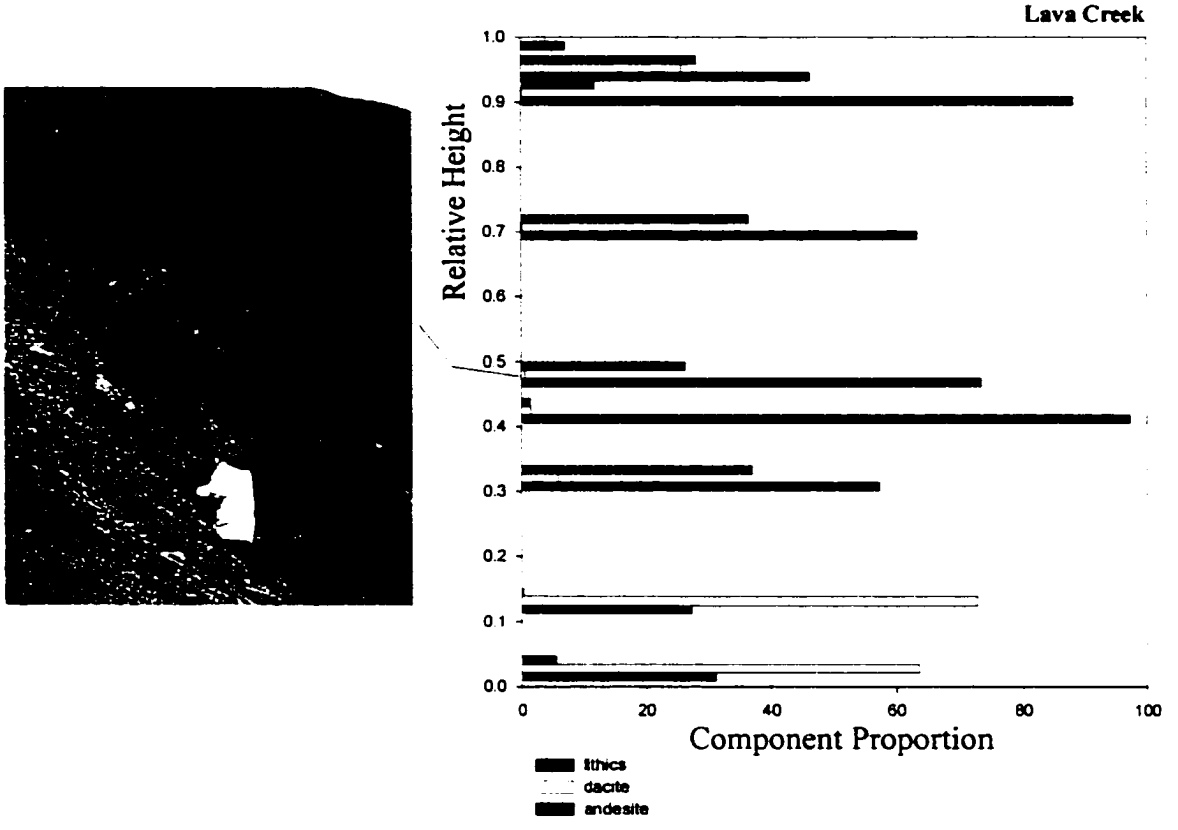

Figure 5: Photograph and componentry of Lava Creek outcrop. The outcrop consists of mixed ignimbrite overlain by andesite ignimbrite. Lithic content increases sharply at the base of the andesite ignimbrite.

are located, the topography is smooth, allowing the formation of the massive deposits. Between the caldera and the Pacific Ocean, however, topography is much more rugged. Accordingly, mixed ignimbrite exposures are confined to stream channels and mountain passes. A cross section of one such channelized flow is exposed on a beach at Kujulik Bay to the south of the caldera (location V of figure 4). This exposure has a maximum thickness of approximately 7 m. The bulk of the ignimbrite is massive and unsorted. Andesite represents 18 %, based on clast counts. Lithics are a minor component, accounting for 2 % of the clasts. Maximum pumice size in this main part of the outcrop is 30 cm. The top two meters comprise two layers of progressively smaller grain size. Andesite is more abundant, subequal to rhyodacite in clast number. Lithics are slightly more abundant, accounting for 7% of the fragments.

2.3.4 Andesite Ignimbrite

The andesite ignimbrite represents the culmination of the caldera collapse event. It is less radially extensive than the mixed ignimbrite, and less confined by topography than the rhyodacite ignimbrite. The andesite ignimbrite overlies rhyodacite fall or ignimbrite in exposures on the caldera flanks, and the mixed ignimbrite at more distal localities. A thin layer of andesite ignimbrite overlies mixed ignimbrite in the Kujulik Bay outcrop on the Pacific coast. Unlike the mixed unit, andesite ignimbrite can also be found near the caldera, sometimes in a lithic breccia or as an agglutinate of large deformed "cauliflower" bombs. In general, the nature of the andesite ignimbrite changes with distance from the caldera. The most proximal exposures are lithic breccias containing juvenile andesite, either as bombs, matrix, or both. Further out on the flanks of the volcano, agglutinated andesite is found. Distal

exposures are nonwelded, matrix supported ignimbrites.

Outcrops of nonwelded andesite ignimbrite in Reindeer Creek and in Birthday Creek contain conspicuous lithic breccia zones near the base of the unit, enclosed in nonwelded ignimbrite. These lithic breccias are 30 to 50 cm thick, and contain lithic blocks up to 15 cm maximum dimension. A zone of unusually large andesite bombs that can reach 50 cm maximum dimension overlies the breccia layers. Banded pumices are common throughout the andesite ignimbrite. The andesite is overlain by a series of post-caldera tephras.

The presence of lithic breccias and the abrupt increase in lithic concentration in the andesite ignimbrite are interpreted as recording the caldera collapse event (following Druitt, 1985; Druitt and Bacon, 1986). The variation of lithic concentration with stratigraphic height is shown in figures 5 and 6 for two representative outcrops. Data from the Lava Creek exposure (fig. 5) illustrates the difference between the rhyodacite pyroclastic flow and the andesite pyroclastic flow; data from the upper Reindeer Creek exposure (fig 6) illustrates the differences between mixed and andesite ignimbrite units. Weight percentages do not include the very large lithic blocks present within lithic breccias. There is a pronounced increase in lithic abundance at the bottom contact of the andesite unit, and even aside from the above mentioned lithic breccia zones, lithics can account for up to half of the mass of the deposit. The restriction of lithic breccia layers to the andesite ignimbrite suggests that the andesite ignimbrite is stratigraphically equivalent to the thick lithic breccias near the caldera rim. Neither rhyodacite nor mixed units has ever been observed to contain more than 14% lithics; there are often less than 10% lithics. The abrupt increase in lithic content in the andesite ignimbrite most likely represents the collapse of the

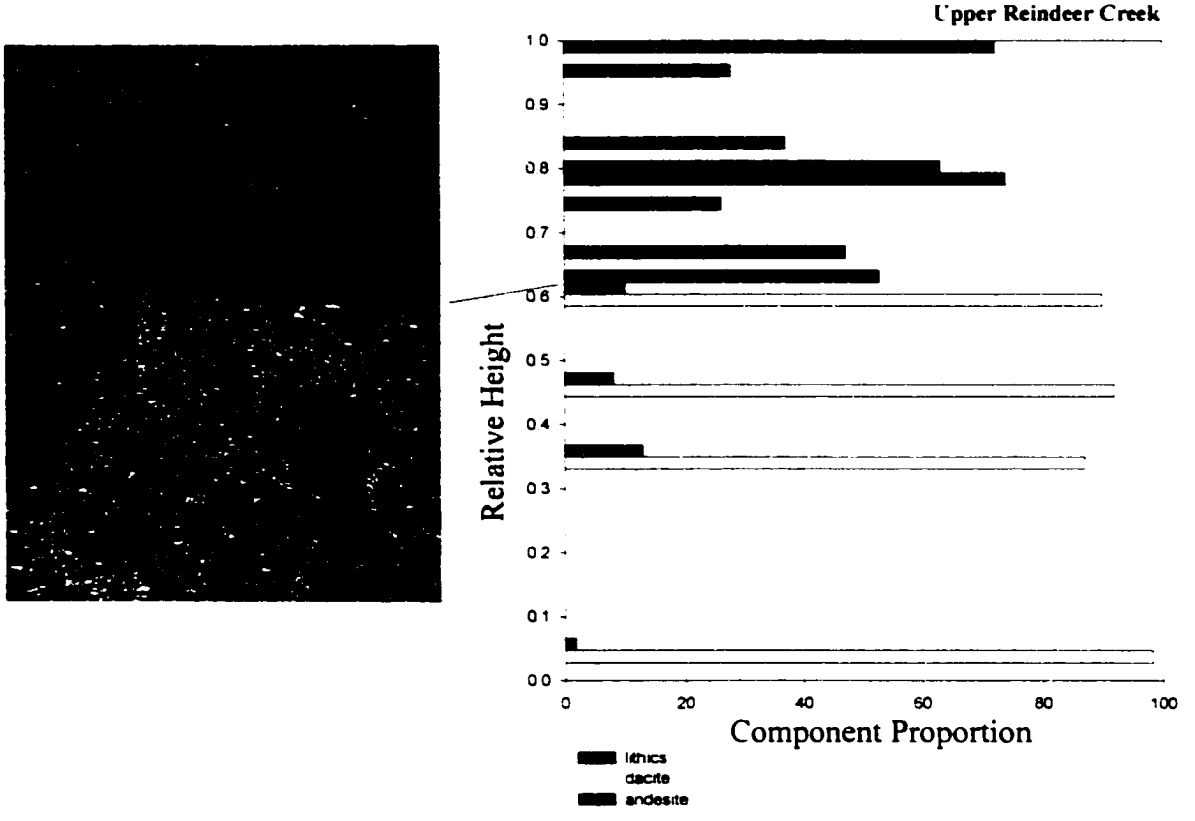

Figure 6: Photograph and componentry of the Reindeer Creek outcrop.

The exposure consists of rhyodacite ignimbrite overlain by andesite ignimbrite. As in the Lava Creek outcrop, lithic content increases abruptly at the base of the andesite ignimbrite.

caldera, rather than increased entrainment of lithic material from the surface over which it flowed. Reasons for this interpretation are: (1) the ground was already covered by previously-emplaced CFE deposits, and (2) the lithics are volcanics like those in the edifice, even in deposits greater than 10 km from the volcano.

2.4 Volume Estimate of CFE Tephra

Estimating the bulk volume of the CFE tephras is difficult because, at most outcrops, only part of the total thickness of the ignimbrite is exposed. Volume estimates are summarized in table 3. Only three exposures of the initial fall deposit are known, making a meaningful estimate of its volume impossible. Thicknesses of the three exposures are between 20 and 50 cm, and occur over an area of roughly 100 km^2. Assuming an average thickness of 30 cm over this area gives a minimum volume for the fall deposit of 0.03 km^3.

Table 3: Summary of volume estimates for juvenile and lithic components of CFE fall and ignimbrite units.

	Rhyodacite	Andesite	Lithics	Total
Fall Deposit	<<1	–	–	<<1
Rhyodacite ignimbrite	2	–	–	2
Mixed Ignimbrite	20	7	–	27
Andesite Ignimbrite		13	4	17
Total	~22	20	4	46

To determine the volumes of the rhyodacite and andesite ignimbrites, boundaries of the deposits were inferred from locations of exposures and of confining

topography. The area known to be covered by rhyodacite ignimbrite is approximately 190 km^2. The andesite ignimbrite covered an area of roughly 1660 km^2. An average thickness of 10 m was assumed. Maximum thicknesses in both of these deposits were 30 to 40 m, so 10 m is a conservative estimate for the average. The volume of rhyodacite ignimbrites is thus estimated to be ~2 km^3. The estimated volume of andesite ignimbrite is 17 km^3.

The volume of the mixed ignimbrite was estimated in a slightly different manner. Mixed ignimbrite is not present at proximal distances. A proximal boundary of the mixed ignimbrite was inferred from observed exposures. Maximum observed thickness in the mixed ignimbrite is 14 m. Based upon observed thicknesses and unpublished observations of T. P. Miller (personal communication), the position of a 10-m isopach was inferred. The area enclosed between the proximal boundary and the 10-m isopach was then estimated to be ~2650 km^2. Two further assumptions were applied to estimate the volume of the mixed ignimbrite. The first is that the area described represents half of the total area covered by the mixed ignimbrite. Starting at the most proximal exposures, the mixed ignimbrite tends to thicken with distance from the vent up to a maximum thickness around 10 m. Distal exposures are usually thinner than this, suggesting the deposit then thins with distance. Because the more proximal portion of the ignimbrite is better exposed, utilizing this assumption is a simple way to account for the poorly exposed areas of the deposit and the presumably significant volume that flowed into the Bering Sea. The second assumption is that the average thickness of the ignimbrite is 5 m. The resulting volume estimate is ~27 km^3.

The proportion of rhyodacite in the mixed ignimbrite is generally around 75 wt. %. Assuming the densities of the two pumice types to be roughly equal to 1 g/cm^3

(andesite pumice is slightly more dense, rhyodacite is slightly less dense), the total volume of rhyodacite is ~20 km^3. The andesite then accounts for 7 km^3 of the mixed ignimbrite.

Lithic concentrations in the rhyodacite fall, rhyodacite ignimbrites and mixed ignimbrites are low. The andesite ignimbrite, however, is lithic rich and includes deposits with up to 80 wt. % lithics, more appropriately termed lithic breccias. Using an average lithic content of the andesite ignimbrites of 40 wt. %, and average lithic density of 2.4 g/cm^3 as discussed below, this yields a total volume of 13 km^3 of andesite and 4 km^3 of lithic material.

The estimated total volume of juvenile material present in the ignimbrites is 42 km^3. Of this, 22 km^3 is rhyodacite and 20 km^3 is andesite. Lithics account for ~4 km^3 of the ignimbrites.

Field data of Sparks and Walker (1977), Rose and Chesner (1987) and Sigurdsson and Carey (1989) suggest that 35% of the total volume of juvenile material erupted will be removed in co-ignimbrite plumes. For an ignimbrite volume of 42 km^3, the total volume erupted is then 65 km^3, or 34 km^3 of rhyodacite and 31 km^3 of andesite. Given the vast distribution of tephra associated with the Aniakchak caldera-forming eruption (e.g., Beget et al., 1992), however, this estimate should be taken as a lower limit.

Smith (1925) estimated the altitude of the pre-caldera summit to have been around 1800 m above sea level. With an average depth of the crater of 450 m, Smith (1925) calculated the volume of removed material to be 62 km^3.

Finally, assuming that the caldera collapse began at the beginning of the andesite ignimbrite phase, and assuming a vesicularity of CFE pumice of 0.65, a

dense rock equivalent (DRE) volume of ~16 km^3 was removed from the magma chamber prior to the onset of collapse. An additional 7 km^3 (DRE) of magma, and 4 km^3 of lithic material were removed after caldera formation began.

2.5 Densities of Magmas and Edifice Rocks

Integral to the concept of a stratified magma body are the densities of magmas involved. Additionally, the average density of the overlying rock exerts a major control over both the depth at which a magma resides (Ryan, 1993) and when and how it erupts. If magma is less dense than typical upper crustal rocks, it will exert an upward buoyant pressure on the roof of the chamber. If the total upward pressure of the magma exceeds the tensile strength of the country rock, an eruption would be expected to ensue.

Densities of rhyodacite and andesite melts were calculated according to the method of Bottinga et al. (1982). Since water contents for the CFE melts are poorly known at this time, an initial value of 2 wt. % was assumed for the CFE andesite sample with the lowest Rb concentration. Using the Rb contents of the other CFE samples, the degree of fractionation was then calculated, assuming Rb to be perfectly incompatible. Assuming water to also be perfectly incompatible, water contents were predicted for each CFE pumice sample according to the calculated degrees of fractionation from the initial andesite. Although we later argue that the rhyodacite is not derived from andesite by closed system fractionation, this approximation is valid if both andesite and rhyodacite were derived from similar basaltic parents. The calculated water concentrations ranged from the assumed initial value of 2 wt. % to 4.44 wt. % in the rhyodacite. Water concentrations of 4.1 wt % in Aniakchak

rhyodacites erupted in 1931 have been determined by Bacon (2000). As discussed in later chapters, the plagioclase-melt equilibrium equations of Housh and Luhr (1991) predict water contents between 3.8 and 4.7 wt. % in the CFE rhyodacite. A similar calculation for the CFE andesite is not meaningful, since, as will be demonstrated, the plagioclase does not appear to have crystallized from that melt.

The density calculation is rather insensitive to temperature in the range appropriate for the CFE magmas. Temperatures of 900° C were used for all samples. Increasing the temperature to 950° C only decreased the calculated density by 0.01 g/cm^3. The calculated densities for the andesites range from 2.42 to 2.46 g/cm^3, with an average of 2.44 g/cm^3. For the rhyodacites, the calculated values range from 2.22 to 2.24 g/cm^3, with an average of 2.23 g/cm^3.

The average density of the edifice was estimated by averaging the densities of 49 lithic fragments extracted from the CFE ignimbrite. Fragments range from plagioclase-rich black pumice with a density of 1.3 g/cm^3, to dark gray andesite lava with density of 2.8 g/cm^3. The average of all 49 lithic densities is 2.4 g/cm^3. It is unknown, however, if the density distribution of this sample of 49 lithics is an accurate representation of the real density distribution of the rocks overlying the magma chamber, since nonvolcanic rocks (e.g. Naknek Formation) are also present in the underlying bedrock sequence.

2.6 Eruption Sequence

The caldera-forming eruption of Aniakchak began with a Plinian phase, in which crystal-poor rhyodacite was erupted. The plinian phase ended when the column quickly collapsed, producing topographically controlled rhyodacite pyroclastic flows.

These rhyodacite flows were deposited mostly on the volcano flanks, although at least one flow reached the Bering Sea.

Pyroclastic flows that deposited the mixed ignimbrites were markedly more energetic than those of the rhyodacite ignimbrites. Evidence for this is the thick, massive nature of the mixed ignimbrites at great distances from the vent, and that mixed deposits are completely absent on the flanks of the volcano, suggesting that the mixed ignimbrite completely drained from the slopes of the volcano. Because of the low lithic content of the mixed ignimbrites, similar to that of the rhyodacite ignimbrite, we infer this increased production of pyroclastic flows to have been caused by an increase in mass flux at the vent, rather than from vent widening. Increasing mass flux also encourages the drawing up of a denser magma into the conduit through a less dense magma (Blake and Ivey, 1986; Spera, 1984). The explosive interaction of the hot pyroclastic flows with the water of the Bering Sea and Pacific Ocean likely led to the generation of large co-ignimbrite columns (Woods and Wohletz, 1991). The lack of mixed pumice fall deposits near the volcano, and the presence of mixed tephras from Aniakchak as far away as the Seward Peninsula (Beget et al., 1992) support this conclusion. Sigurdsson and Carey (1989) inferred a similar process in the 1815 eruption of Tambora.

The onset of caldera collapse appears to have occurred after most of the rhyodacite magma was erupted, as indicated by the sudden increase in lithic content at the base of the andesite ignimbrites. The presence of agglutinated andesite ignimbrite in several exposures both to the north and south of the caldera demonstrates that the andesite pumice blocks were still plastic during flow and deposition. This, along with a presumably lower eruption column due to increased vent area or lower volume flux,

led to a shorter runout distance of the andesite ignimbrites. The sequence of events is summarized in figure 7.

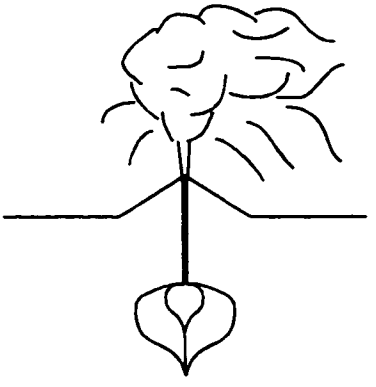

Stage 1: Eruption of dacite, deposition of dacite fall and pyroclastic flows

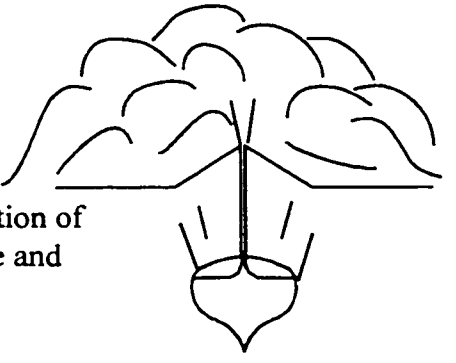

Stage 2: Increase in mass flux; eruption of dacite and andesite; column collapse and mixed ignimbrite deposition

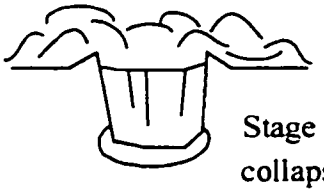

Stage 3: Depletion of dacite; deflation of magma chamber; collapse of caldera; andesite ignimbrite deposition

Figure 7: Summary diagram of caldera-forming eruption sequence.

Chapter 3: Petrology of the CFE Andesite

3.1 Introduction

Evidence of hybridization of andesitic arc magmas is widely recognized. Such events involve abrupt changes in magmatic composition, often toward a "less evolved" composition. Nevertheless, magmatic trends have historically been modeled as a liquid line of decent, in which composition marches irreversibly in infinitely small steps reflecting fractional crystallization and assimilation toward "petrogeny's residua". Although the importance of both fractionation and mixing cannot be doubted, it is important to understand their relative roles and the sequence in which these processes occur; that is, the path by which an individual erupted magma batch is created. There is evidence to suggest that at least some andesitic systems have shallow reservoirs and that input to these systems may be fundamentally bimodal in composition. One way in which such a situation might arise is if much of the melt/liquid segregation occurs when melt fraction is low: during melting in the mantle and crust and during crystallization of arc plutons. These processes may produce a wide spectrum of primary magmas, from basalt through rhyolite which hybridize in shallow subvolcanic systems (e.g., Class et al., 2000; Borg and Clynne, 1998; Muller et al., 2001).

Many aspects of the calcalkaline trend can be explained through either fractional crystallization or two-component mixing. Mixing is often required by the phenocryst assemblage. For some elements, however, non-linear variation precludes a simple mixing interpretation. In this paper, we explore the possibility that rather than recording an underlying liquid trend, the departures from linearity reflect chamber

fractionation processes superimposed on a mixing trend. To do this, we look at an arc system where there is: (1) geologic and/or petrologic evidence for bimodal inputs to a shallow chamber; (2) abundant evidence of hybridization in intermediate eruptives; and (3) a strong departure from chemical linearity in the latter. Aniakchak Caldera, Alaska satisfies all three of these criteria.

3.2 Mineralogy of the Aniakchak CFE Andesite

The phenocryst assemblage in the Aniakchak CFE andesite comprises plagioclase, clinopyroxene, magnetite, and traces of ilmenite. Groundmass phases include plagioclase, pyroxenes, oxides and glass. Mass balance calculations between the melt and observed crystal phases indicate that the andesites contain a total of 8 weight % phenocrysts.

Analyses of plagioclase cores in the CFE andesites reveals a bimodal population of compositions (figure 8). One mode, centered on An_{40} comprises plagioclase crystals which are typically free of sieve textures, although some rounded corners, indicating resorption, are present. The size, range, and position of the low-Ca plagioclase mode in the CFE andesite is quite similar to that of the single mode representing the plagioclase compositional distribution in both the CFE rhyodacite and the late precaldera Black Nose rhyodacite. Both of these rhyodacites, as well as several other late precaldera rhyoacite lavas (discussed in chapter 3), contain plagioclase populations with compositions centered around An_{40}. A second mode exists in the CFE andesites around An_{85}. These plagioclase crystals are characterized by coarse sieve textures throughout the crystals, indicative of disequilibrium with the host melt. Aniakchak high-alumina basalts, like sample 92CNA22 from the post-

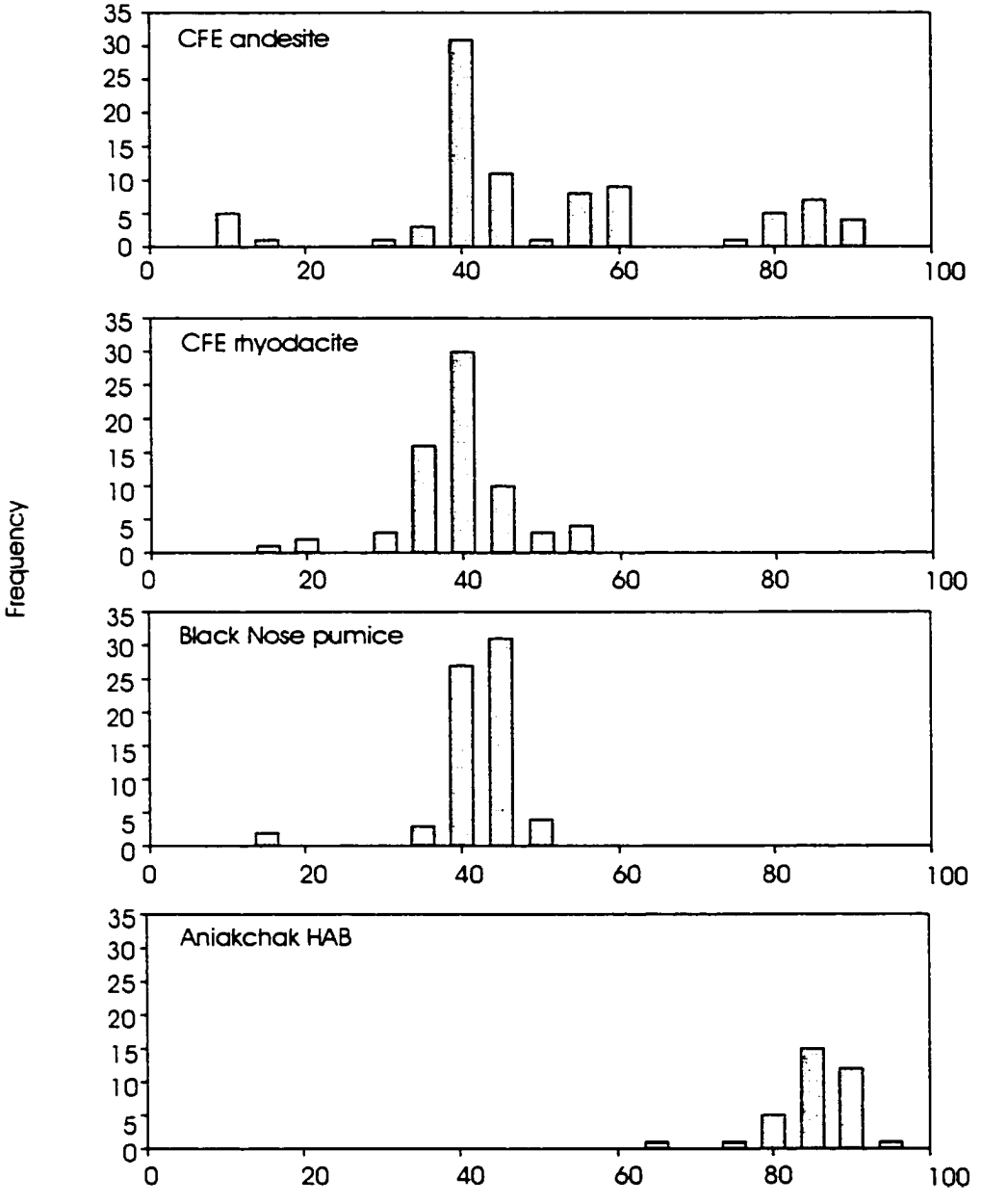

Figure 8: Comparison of plagioclase core compositions in CFE rhyodacites, andesites, precaldera rhyodacites, and high-alumina basalt.

caldera Blocky Cone, contain a similar population of plagioclase crystals with compositions around An_{85}. A variety of zonation styles is present in both low- and high-Ca plagioclase in the CFE andesites, with oscillatory zonation being the most common (figure 9). The only major ferromagnesian silicate in the CFE andesite is augite, with typical composition of $En_{44-48}Fs_{12-14}Wo_{40-43}$ and molar Mg # $\left(100 \times \frac{MgO}{MgO + FeO}\right)$ between 79 and 85. Augite crystals in the CFE andesite typically have molar Kd values $\left(\frac{FeO^{cpx}}{MgO} \Big/ \frac{FeO^{melt}}{MgO}\right)$ between 0.17 and 0.22. These values are low in comparison to equilibrium crystallization Kd between 0.23 to 0.26 (Grove and Bryan, 1983). These low values indicate equilibrium crystallization from a more magnesium-rich melt. Aniakchak magmas with appropriate FeO/MgO ratios to crystallize such clinopyroxenes are basalts with around 52 wt. % SiO_2.

The andesite contains trace amounts of both quartz, with which it is not saturated, and olivine, which should not be stable in so siliceous a melt. Both of these xenocryst types have corroded and embayed edges, indicative of disequilibrium.

3.3 Temperature Estimates for the CFE Andesite

Temperature estimates based on Fe–Ti distribution in two magnetite–ilmenite pairs (Andersen and Lindsley, 1988; Stormer, 1983) indicate temperatures of 889°C and 907°C. Ilmenite is rare in CFE products, magnetite-ilmenite pairs in contact with each other even more so. These pairs pass the equilibrium criterion proposed by Bacon and Hirschmann (1988) based on Mg-Mn partitioning between the two phases. Oxygen fugacities associated with these two pairs are –11.9 and –11.5 log units

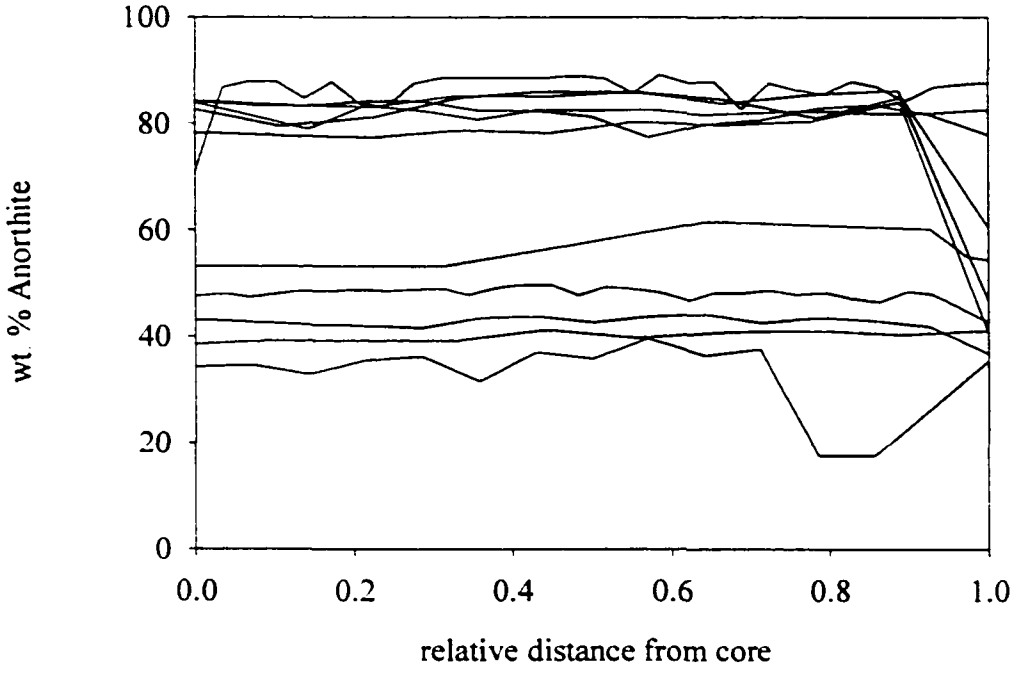

Figure 9: Plagioclase profiles from CFE andesite.

respectively, corresponding approximately to an NNO+1 buffer curve. One other pair, which also passes the Bacon-Hirschmann test, gives an anomalously high temperature of 1174 °C and log (fO_2) of –7.3.

Liquidus temperatures based on liquid-solid equilibrium using the MELTS program (Ghiroso and Sack, 1995) are estimated to be 1075°C at 3 kb pressure, and 1140°C at 7 kb pressure. Calculations were performed using bulk compositional data for individual samples, and assuming 2 wt. % H_2O. Temperature data for CFE andesite and rhyodacites, as well as from late precaldera rhyodacites are summarized in table 4. Despite the apparently near-liquidus condition of the andesite magma, as evidenced by its low crystallinity, oxide compositions disagree with calculated liquidus temperatures by as much as 246°C.

3.4 Phase Equilibria

Grove et al. (1982) have experimentally derived liquid lines of descent for calc-alkaline magmas. Using the projection scheme of Grove et al.(1982), CFE andesite and rhyodacite and typical Aniakchak HAB are plotted on a plagioclase-saturated olivine-augite-silica pseudo-ternary phase diagram in figure 10. The 1-atmosphere equilibrium phase boundaries determined by Grove et al. (1982) are included for reference. The CFE rhyodacites plot near the plagioclase + augite + pigeonite + silica eutectic. One of the basalts falls in the plagioclase + olivine field, another is located on the plagiocalse + olivine + augite cotectic, directly between the first basalt point and the silica corner. It should be noted that at higher pressures the cotectic boundaries become displaced towards the olivine corner, so the basalts also lie on a higher pressure plagioclase + olivine + augite cotectic, consistent with the

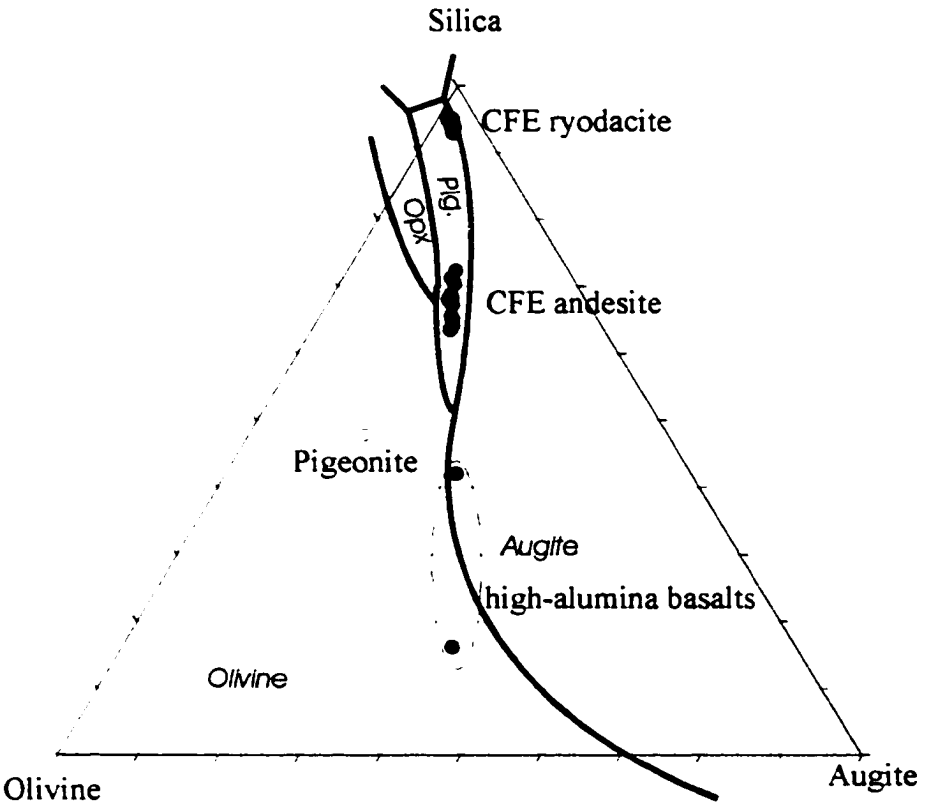

Figure 10: Pseudoternary projection of CFE andesites and rhyodacites, and high-alumina basalts. The projection scheme of Grove et al. (1982) is used to project the data from the plagioclase vertex.

observed phase assemblage in the basalts. CFE andesites, however, plot within the 1-atmosphere plagioclase + pigeonite phase volume. The CFE andesites are lacking pigeonite. Furthermore, the trend established by the andesite compositions does not project directly away from pigeonite, so removal of pigeonite from the melt

Table 4: Summary of temperature and oxygen fugacity data for CFE andesites and rhyodacites, and late precaldera rhyodacites. Magnetite and ilmenite compositional data are included in appendix 4.

Sample	Type	Temp (deg C) Fe-Ti oxides	log(fO2)	Temp (deg C) pyroxenes	MELTS liquidus, 3kb	MELTS liquidus, 7kb
99AC26 - 1	precaldera	979.7	-12.6	1082	978.9	987
99AC26 - 3	RD lava	1073.4	-12	1082	978.9	987
99AC26 - 8		1004.7	-12.2	1082	978.9	987
97ANB45 - 2	precaldera	971	-11.6	1018	970.11	977
97ANB45 - 6	RD lava	1072.5	-10.9	1018	970.11	977
97AC22 - 1	precaldera	899.8	-13	1040	982	1031
97AC22 - 2	RD lava	925.7	-12.4	1040	982	1031
97AC22 - 3		1006.9	-12.2	1040	982	1031
97AC22 - 4		1182.1	-10.2	1040	982	1031
97AC22 - 6		969	-11.3	1040	982	1031
97ACAF1a8	CFE RD	887.8	-11.8		929	953
97ACAF1b1	CFE RD				930.5	951
97AC36a - 2	CFE RD	897.6	-11.7			
97AC36a - 4		894.6	-11.8			
97AC36b - 1	CFE And	889.2	-11.9		1070	1135
97AC36b - 2		906.8	-11.5		1070	1135
97ACAF1e2	CFE And	1173.6	-7.3		1079	1146
97AC14 - 2	precaldera	938.6	-11.9		982	994
97AC14 - 3	RD pumice	933.2	-12		982	994
97AC14 - 4		947.6	-11.8		982	994
97AC19 - 1	precaldera RD pumice	935.1	-11.5	1059	995.6	1023

could not reproduce the observed trend. The data could coincide with a higher pressure plagioclase + pigeonite + augite cotectic; the paucity of pigeonite in the andesites makes such coincidence truly coincidental. At still higher pressures, the cotectics could shift enough to place the andesites in the plagioclase + augite phase volume. This would be consistent with the observed phase assemblages, but the data do not project directly away from augite compositions. The data cannot be explained easily by any closed system fractionation processes, a conclusion which is corroborated by other lines of evidence presented below. Magma mixing has been presented as a viable explanation for deviations from expected liquid lines of descent (Grove et al., 1982; Walker et al., 1979) and is particularly attractive in the case of the CFE andesites in light of the petrographic and mineralaogical evidence for mixing (e.g., both rhyodacite- and basalt-derived plagioclase in CFE andesite).

3.5 Whole Rock Geochemistry

Andesite compositions from the caldera-forming eruption show broadly consistent major element trends to those established by pre- and post-caldera data (figure 11, unpublished data of C.R. Bacon, C.A. Neal, and C.J. Nye). There is more scatter in the pre-caldera data, and the data set is sparse relative to the post-caldera data. Although there is no obvious chemical distinction between the pre-caldera calc-alkaline data and post-caldera data, the post-caldera data are primarily used to compare with the CFE andesites. MgO has been chosen as a measure of differentiation, where decreasing concentrations of MgO correspond to increasing degree of differentiation. As MgO decreases, SiO_2, K_2O, and Na_2O in the post-caldera data increase. For all three of these oxides, the slope of the trend changes at MgO

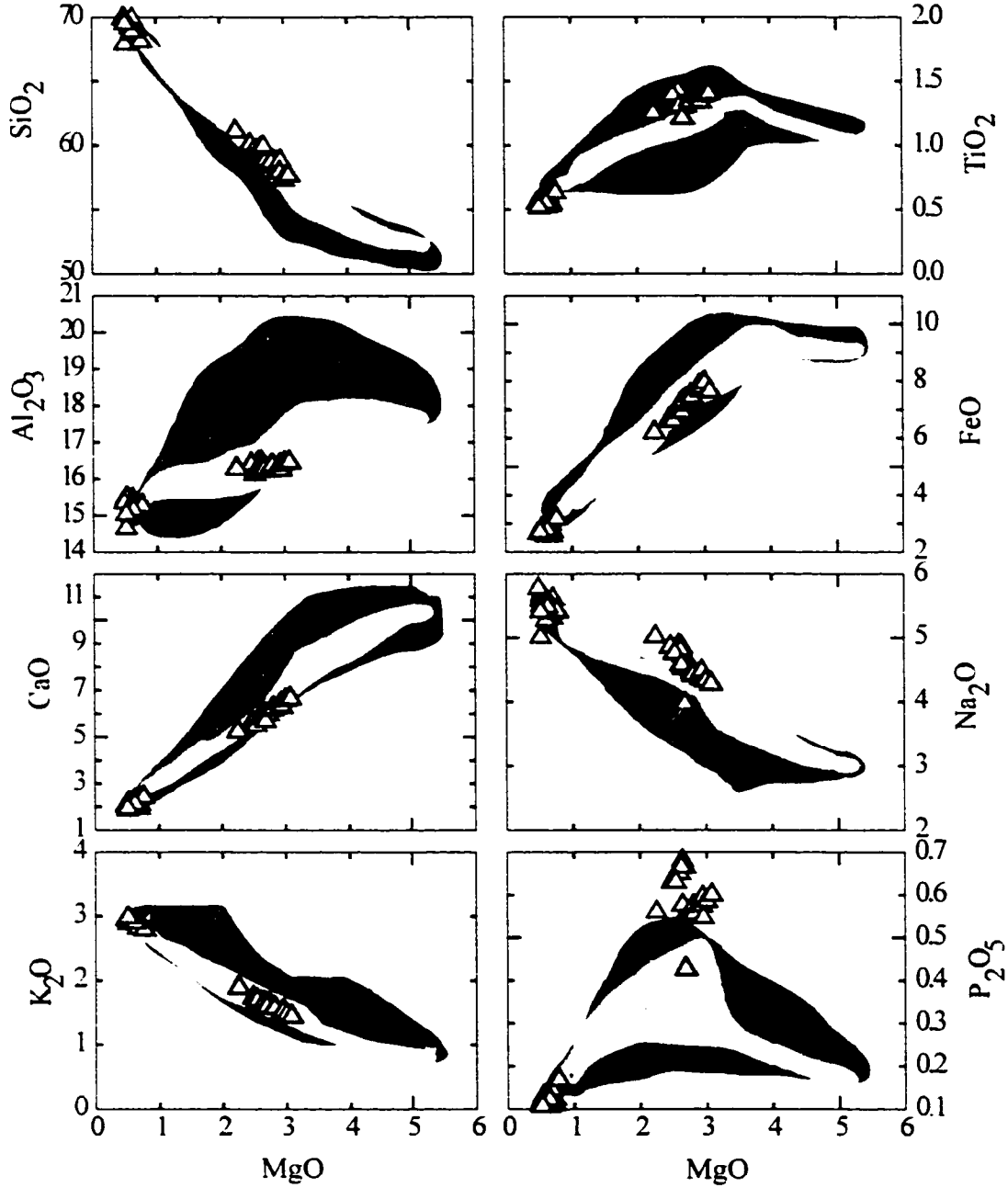

Figure 11: Major elements in CFE tephras. Precaldera (dark grey) and postcaldera (light grey) data are shown for comparison. All oxides are in weight percent.

concentrations of about 3.5 wt. %, being steeper at lower MgO values. Al_2O_3 and CaO both decrease with decreasing MgO, both at relatively constant slopes. FeO concentrations remain nearly constant at MgO concentrations >3.5 wt. %, then decreases at lower MgO concentrations. TiO_2 and P_2O_5 both increase with decreasing MgO in the high-MgO end of the array. TiO_2 begins to decrease at around 3.5wt. % MgO. A change to a decreasing trend occurs in P_2O_5 at around 3 wt. % MgO. Both increasing and decreasing trends in both oxides occur at roughly constant slopes. The pre-caldera and post-caldera data both span a range of 5.5 down to 0.5 wt. % MgO. The CFE andesite ranges from 3.1 to 2.5 wt. % MgO. While most CFE andesite major element data coincide with the trends defined by pre- and post-caldera data, there are significant exceptions. Most notably, P_2O_5 in the CFE andesite is higher than in any other sample from Aniakchak. The CFE andesites also show enrichments in TiO_2 and Na_2O relative to other andesites from Aniakchak.

Similar plots of trace elements versus MgO show a similarly consistent composition of CFE andesites with pre- and post-caldera data (figure 12). The majority of analyzed elements are incompatible, and thus increase with decreasing MgO. For example, Rb, Ba, Zr, and Eu all increase at a relatively constant rate with decreasing MgO. Vanadium increases over the high-MgO portion of the data set, but the trend contains a deflection at around 4 wt. % MgO, and vanadium then falls at a decreasing rate. Strontium remains relatively constant between 5.5 and 3 wt. % MgO, but falls at a constant rate as MgO decreases below 3 wt. %. Like in the major element oxides, the CFE andesite trace element data are within the linear fields defined by pre- and post-caldera data. Again, there are notable exceptions to this general correspondence. Vanadium in the CFE andesites is lower than in post-

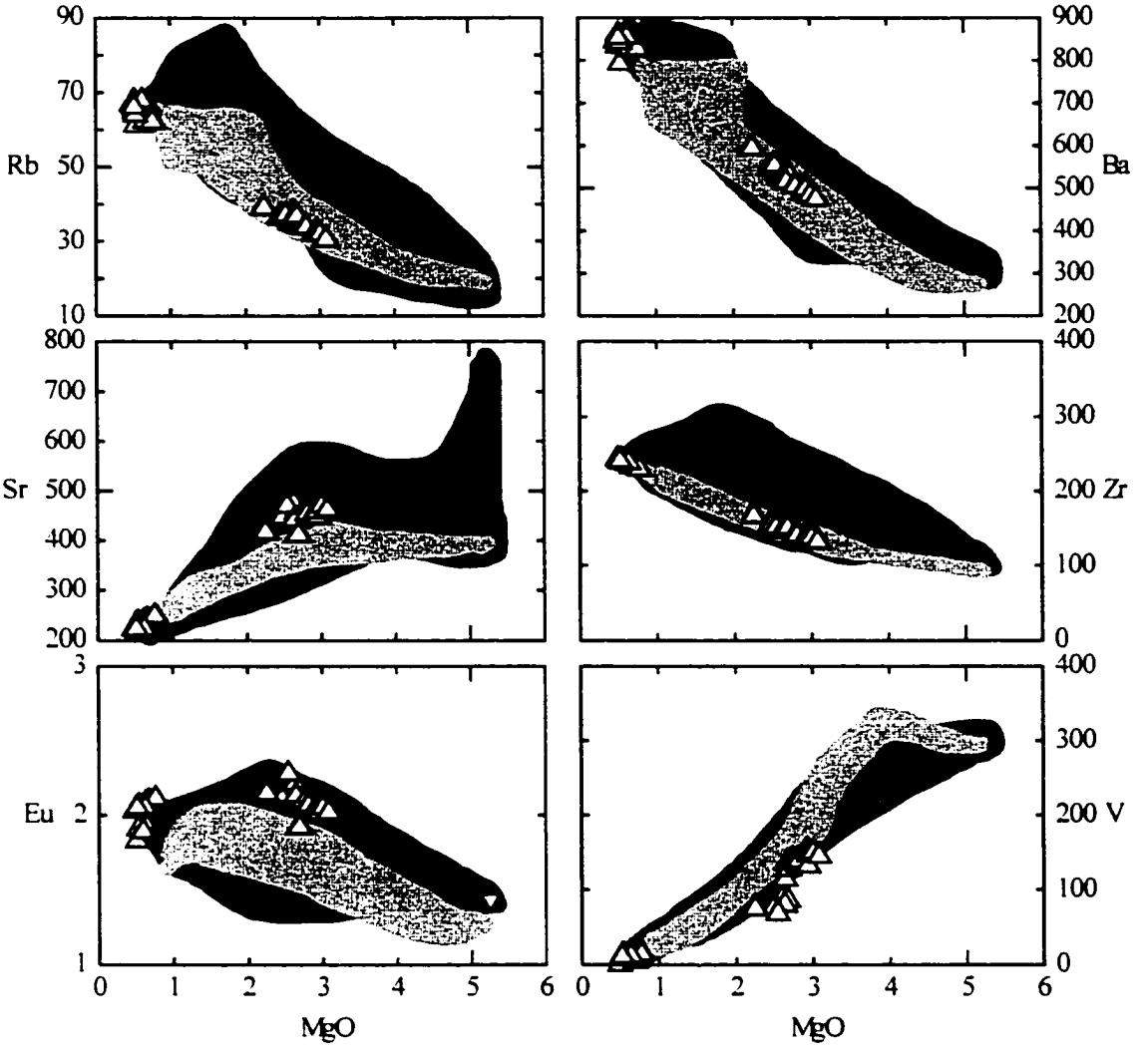

Figure12: Selected trace element concentrations (ppm) in CFE tephras versus MgO (weight percent). Precaldera data (dark grey) and postcaldera (light grey) data are shown for comparison.

caldera andesites. Sr is elevated in the CFE andesites relative to post-caldera andesites. The light and middle rare earth elements are enriched in the CFE andesites, relative to post-caldera andesites of similar MgO content.

Using the MELTS algorithm developed by Ghiorso and Sack (1995), liquid lines of descent were calculated using a high-alumina basalt as a starting point. Initial water content in the model was taken to be 1 wt.%, and the pressure was held constant at 7 kb, corresponding to lower crustal depths. In one model run, the system was constrained to undergo equilibrium crystallization. A second run was performed, in which phases were fractionated as they crystallized. The results are compared to the suite of data in figure 13. Under these conditions, MELTS calculated a liquidus temperature of 1227 °C. According to this equilibrium crystallization model, augite of composition $En_{44}Fs_{11}Wo_{44}$ is the liquidus phase, followed by plagioclase with a composition of An72 at a temperature of 1182°C. At 1117° C pigeonite with a composition of $En_{51}Fs_{34}Wo_{15}$ begins to crystallize. Magnetite is stabilized at a temperature of 1082° C, followed by apatite at 1032° C. Orthopyroxene ($En_{50}Fs_{48}Wo_2$) stabilized at a temperature of 972° C, and garnet ($Alm_{63}Gr_{13}Py_{23}$) at 932° C. The algorithm failed to converge at temperatures below 887° C. At this point, only about 19 wt. % liquid remains in the system, and the SiO_2 concentration has increased from 52 wt. % to 63 wt. %.

Under a fractional crystallization model, initial augite and plagioclase compositions are similar; plagioclase again is stabilized at 1182° C. Pigeonite follows at a higher temperature of 1137° C. The appearance of pigeonite marks the end of augite crystallization. Magnetite becomes stable at 1102° C. At 1027° C apatite begins to crystallize. Garnet with composition $Alm_{71}Gr_{15}Py_{14}$ begins to crystallize

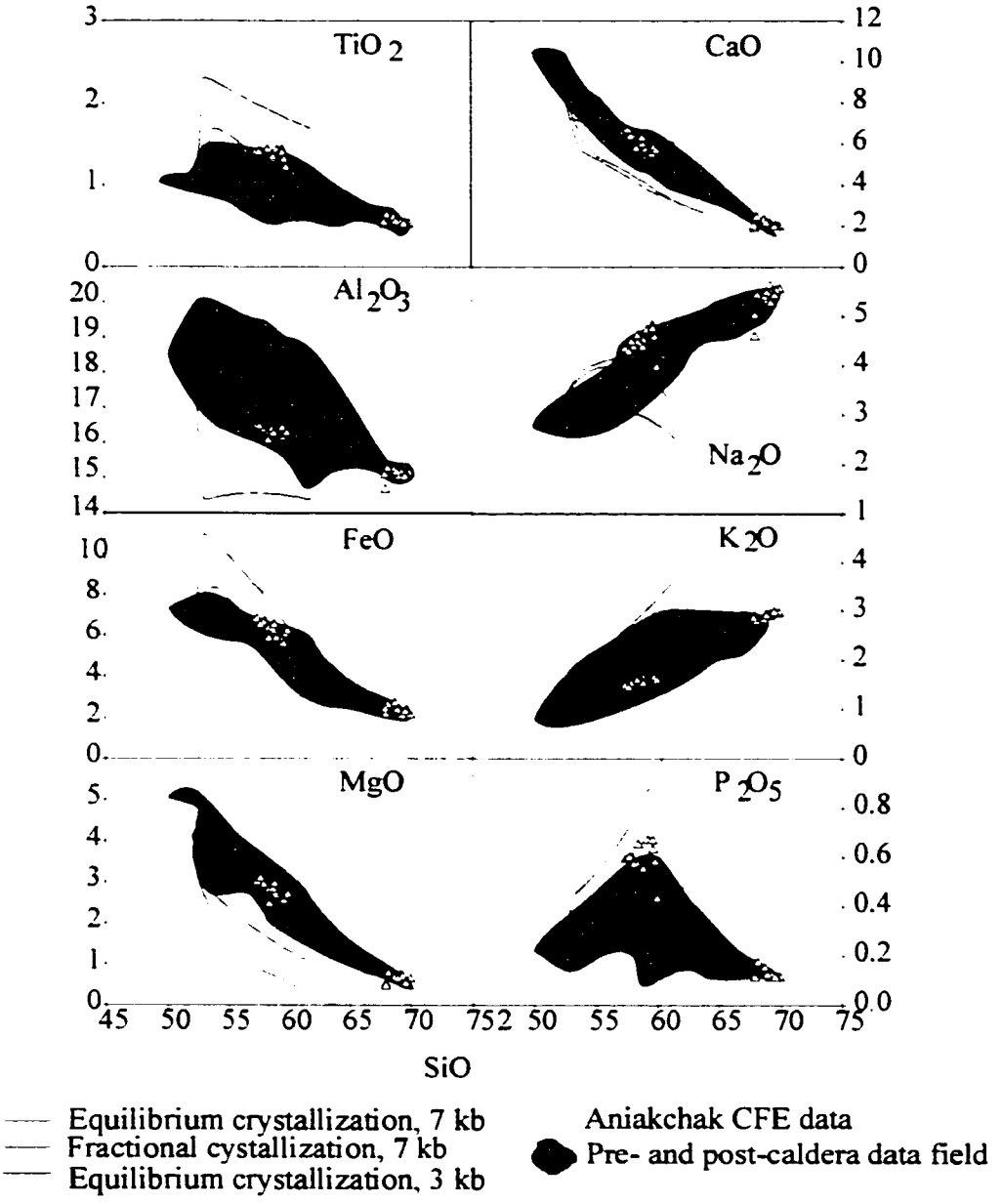

Figure 13: Comparison of Aniakchak data with MELTS calculations of crystallization differentiation. Two equilibrium crystallization runs were performed at 3 and 7 kb pressure, respectively. A fractional crystallization model was also run at 7 kb pressure.

and pigeonite vanishes at 992° C. Ilmenite appears at 982° C while magnetite ceases to crystallize. This assemblage of garnet, plagioclase, ilmenite, and apatite continues to crystallize until the algorithm fails at a temperature of 862° C. At this temperature, about 20 wt. % of the original liquid remains, and has evolved to around 66 wt. % SiO_2. A final simulation, in which the basalt crystallizes under equilibrium conditions at 3 kb pressure and 0.2 wt. % H_2O, to simulate shallow depth, was run. In this model, plagioclase (An_{74}) is the liquidus phase. The liquidus temperature is 1228° C. Augite ($En_{48}Fs_{13}Wo_{40}$) begins to crystallize at 1188° C, followed by pigeonite ($En_{61}Fs_{23}Wo_{16}$) at 1173° C. Magnetite and apatite begin to crystallize at 1123°C and 1033° C, respectively. The model fails at a temperature of 968°C, when 12 wt. % liquid remains. At this point, the SiO_2 concentration is 66 wt. %.

Even with only an 11 to 14 wt. % SiO_2 span produced in the calculations, it is clear that the suite of rocks at Aniakchak did not evolve from a single basalt parent under closed-system conditions. The two high pressure models produce similar liquid compositional paths. Fractional crystallization leads to greater initial enrichments in FeO and TiO_2. Na_2O increases throughout the fractional crystallization model, while equilibrium crystallization eventually leads to Na_2O reduction. The suppression of plagioclase crystallization in the early stages causes the Al_2O_3 concentration to increase from about 18 wt. % to 19.6 wt. % in both models. MgO decreases from around 4.3 wt. % to nearly 1 wt. %, with only a 3 wt. % increase in SiO_2. The low pressure model shows an initial depletion of Al_2O_3 due to early plagioclase crystallization. Much higher FeO and TiO_2 concentrations are reached as a result. Low pressure crystallization could reproduce the P_2O_5 concentrations found in the CFE andesite; however, such a mechanism would produce only a single population of

plagioclase with compositions around An_{55} – a composition intermediate to those of the two plagioclase populations observed in the pumice samples. Furthermore, low pressure crystallization fails to reproduce the observed concentrations of TiO_2, Al_2O_3, MgO, Na_2O, and K_2O. Some portion of the rhyodacite magma represented by the high silica end of the data set could have been produced by crystallization of basaltic magma at relatively high pressure, and perhaps variably mixed with partial melts of basaltic plutons. Much of the remaining compositional variation in the data suite can be explained by mixing between basalt and rhyodacite. Although much of the compositional and mineralogical data for the CFE andesite can be satisfied by such hybridization, the enrichments of P_2O_5 and REE are not explained.

In order to assess the nature of the various elemental enrichments in the CFE andesites, it is useful to determine whether these elements are being added back into the magma, or if they were simply less efficiently depleted in the CFE andesite by fractionation processes than in other andesites of similar major element composition. To do this, it is noted that incompatible element data sets will define trends with slopes of 1 on log-log plots if the elements have identical bulk distribution coefficients. Slopes less than one indicate that the element on the y-axis is more compatible than that on the x-axis; the opposite is true for slopes greater than 1. If one chooses an element for the x-axis that is very incompatible (i.e., one which has a bulk distribution coefficient, D~0), then any element chosen for the y-axis cannot have a bulk distribution coefficient less than this. In other words, trends controlled by fractional crystallization should all have slopes of one or less when the x-axis element has D~0.

Figure 14a shows a log-log plot of Th vs. P_2O_5. In the CFE andesites, thorium

has a bulk distribution coefficient of around 0.06 (Bacon and Druitt, 1988. It is reasonable to expect phosphorus to have a bulk distribution coefficient at least this high. Accordingly, at Th concentrations less than about 4, pre-caldera and post-caldera data define a trend of slope ~1. At higher Th concentrations, the slope becomes strongly negative. The P_2O_5 concentration in the CFE andesite, however, is higher than the trend. These andesites are clearly not related to the more mafic rocks in the suite by closed-system crystal fractionation, or simple binary mixing, but have had phosphorus added. A similar plot of Th versus Ti (figure 14b) also shows enrichments above the trend. In this case the trend defined by pre- and post-caldera data has a slope less than one, so the CFE andesite data may represent a decrease in the rate of depletion rather than an absolute enrichment. Europium in CFE andesites is above the trend defined by the less evolved (Th < 4 ppm) rocks in the pre- and post-caldera data (figure 14c). The slope of this portion of the data is near unity. Finally, rubidium and thorium are equally incompatible in the Aniakchak suite, as evidenced by the near unity slope throughout the data set (figure 14d). Data from the CFE andesite have a similarly sloping trend, but they lie slightly below the trend defined by the rest of the data from Aniakchak. Some trace elements seem to have been added to the CFE andesites, while other trace elements have been unaffected.

3.6 Discussion

3.6.1 Possible Sources of Elemental Enrichment

The observed elemental enrichments in the CFE andesite could be explained by one of several hypotheses: 1) derivation from an unusual parental magma with differences inherited from inhomogeneities in the mantle source, 2) derivation from a

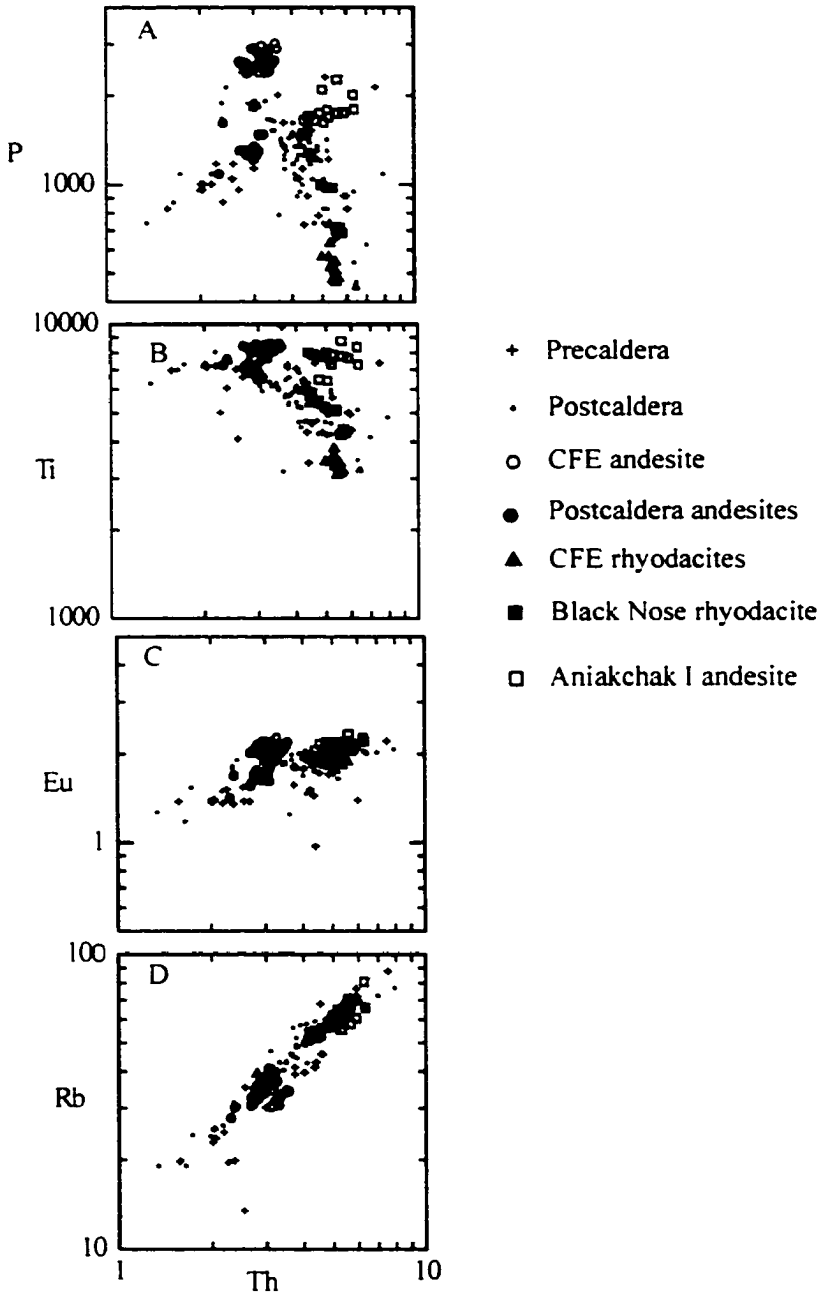

Figure 14: Comparison of selected trace elements with thorium. Phosphorus shows a pattern indicative of absolute enrichment in the CFE andesites. Other plots are inconclusive regarding the nature of the elemental enrichments. See text for details.

parental magma with differences derived from greater than normal fluid flux from the subducted slab, 3) hydrothermal fluid addition in the crustal andesite chamber, 4) assimilation of crustal material, or 5) processes within the crustal magma chamber.

Wide variations in primitive magma compositions have been reported in the Cascade Range of northern California, Oregon, and Washington (Bacon et al., 1997a). Although there is a range in basalt compositions in the pre-caldera suite at Aniakchak, no sample has been found that can account for all of the chemical deviations found in the CFE andesites. In particular, to explain the CFE andesites as simple binary mixtures, a mafic endmember with 5 wt. % MgO would need around 1.5 wt. % P_2O_5. This is around 10 times the P_2O_5 concentrations observed in other basalts at Aniakchak. This is unlikely.

An enrichment in light and middle REE in the CFE andesites relative to post-caldera andesites, shown in figure 15, is similar to a slab fluid signature recognized in primitive mantle melts due to greater fluid-mobility of LREE relative to HREE (e.g., Class et al., 2000). Conceivably, then, the parent to the CFE andesite could be derived from partial melting of subarc mantle that contains a greater proportion of slab-derived fluid. Comparison of ratios between large ion lithophile elements (LILE) and high field strength elements (HFSE) in CFE and post-caldera andesites provides a test for this hypothesis. Because LILE are more mobile in metasomatic fluids liberated from the subducted slab than HFSE (McCulloch and Gamble, 1991; Tatsumi et al., 1986), the CFE andesites should show a positive correlation with P and REE if their enrichments are due to increased fluid flux in the mantle. Figure 16 shows that among andesites with 2.5 to 3 wt. % MgO, Rb/Nb ratios are constant or very slightly decreasing with increasing P concentrations. Furthermore, a log-log plot of the Rb vs.

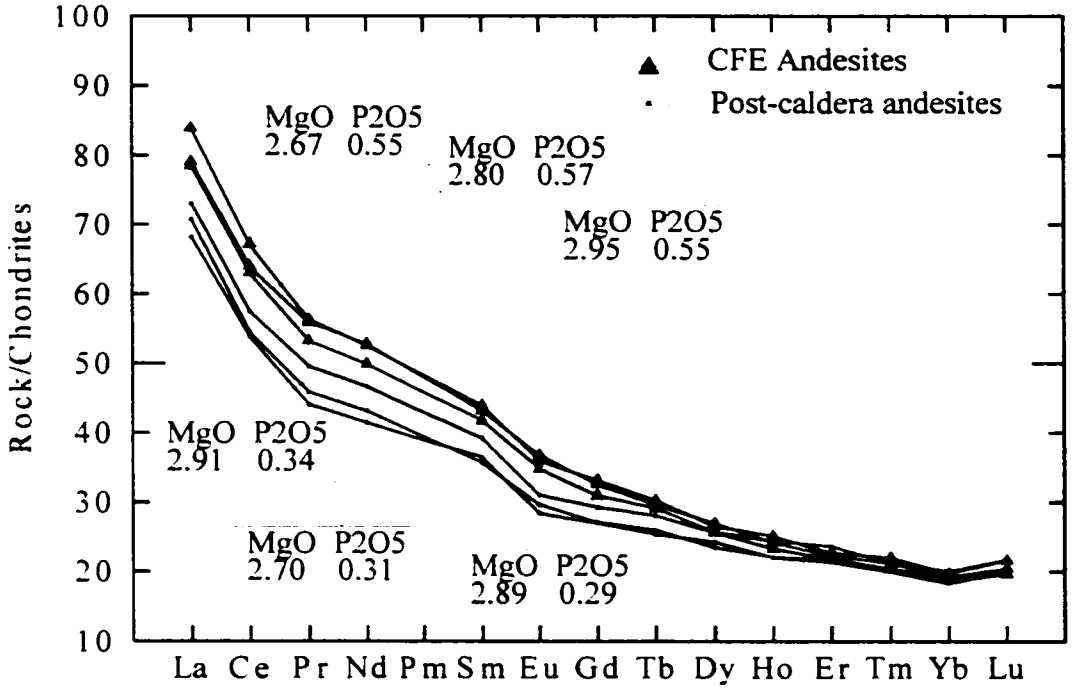

Figure 15: Comparison of rare earth element patterns in CFE andesites and postcaldera andesites with similar major element compositions.

Nb (figure 16 inset) from the entire data set produces a linear array with a slope of unity. Fractionation processes have not fractionated Rb and Nb from each other. Likewise the process responsible for the P and REE enrichments also left the Rb/Nb ratios undisturbed.

While REE and P deviations can not be explained by crystallization differentiation processes, or deep subduction metasomatization variations, the mobilities of REE are less easily defined in the shallow crustal environment. Granite weathering and ore formation studies find large variations in REE mobilities. For example, Lentz and Gregoire (1995) found both P and LREE to be fluid-mobile in the alteration of granite. Poitrasson et al. (1995), however, found that MREE and HREE were more efficiently leached from granite than LREE, while the opposite was true in a hydrothermally altered rhyolite. Van der Weijden and van der Weijden (1995) found a wide range of mobilities of REE among four different granitic bodies. This wide variation results from differences in the compositions of the fluids themselves. As a result, without some knowledge of the composition of the hydrothermal fluid, fractionation patterns in REE cannot be relied upon to determine contributions from such hydrothermal fluids to crustal magmas. On the other hand, LILE are consistently more mobile in hydrothermal fluids than HFSE. As discussed above, this relationship has been found in high-pressure subduction zone environments (McCulloch and Gamble, 1991; Tatsumi et al., 1986). Low-pressure experiments by You et al. (1996) on subduction-zone sediments gave similar results. Finally, Lentz and Gregoire (1995) found HFSE to be less mobile than LILE during the alteration of granites.

Based on these studies, trace element ratios such as Rb/Nb can be used to test

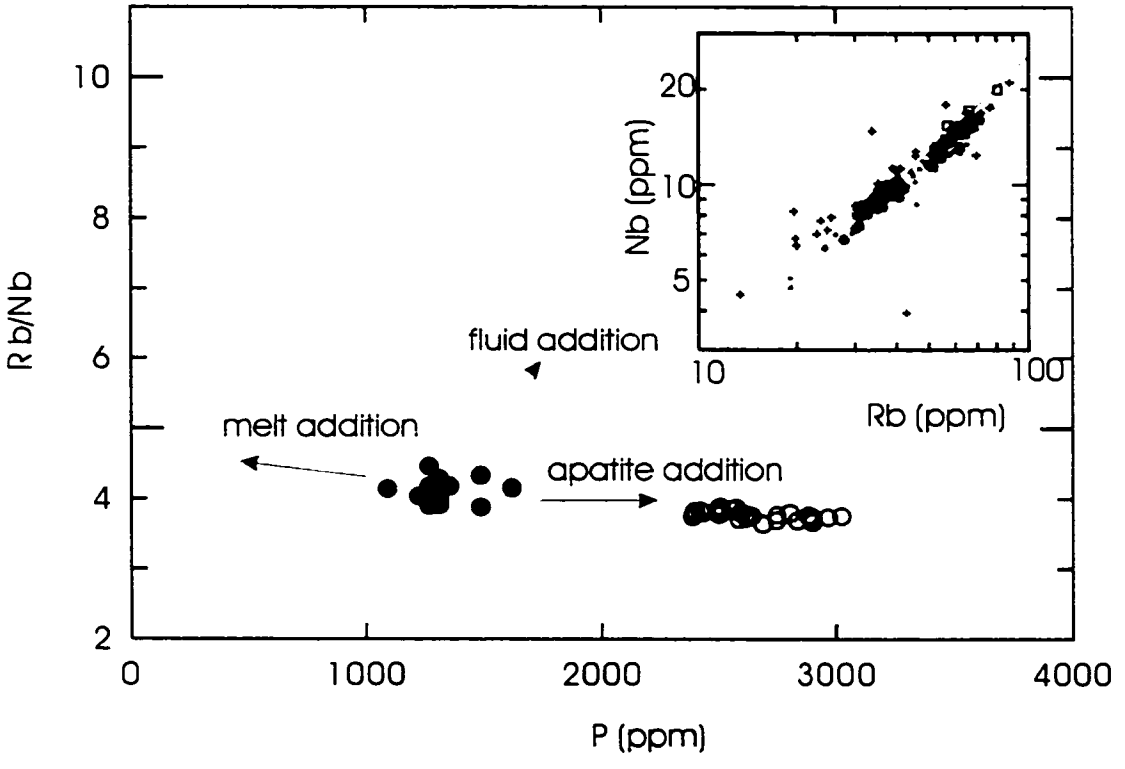

Figure 16: Rb/Nb ratio versus P in CFE andesite and similar postcaldera andesites. Arrows indicate trends expected from various processes potentially responsible for the P enrichments in the CFE apatite. Open circles represent CFE andesite samples; closed circles represent post-caldera andesites. Inset shows the similar behavior of Rb and Nb in Aniakchak rocks.

for hydrothermal influence in both low- and high-pressure environments. Using a similar argument to that used above, then, the constant Rb/Nb ratios with increasing P rules out hydrothermal fluid contamination as the source of P and REE enrichment.

Bulk assimilation of wall rock seems unlikely as well, given the similarity in major elements between CFE andesites and other andesites from Aniakchak. One sample of granodiorite collected from the CFE lithic breccia, and thought to originate from the Jurassic Naknek conglomerate, and ultimately from the Alaska-Aleutian Batholith described by Reed and Lanphere (1973), contains 0.18 wt. % P_2O_5 - similar to the P_2O_5 concentrations in both high-alumina basalt (HAB) and rhyodacite from Aniakchak. Assimilation of Alaska-Aleutian Batholith granodiorite could not increase the P_2O_5 levels above that produced by binary mixing. Assimilation-fractional crystallization (AFC) of a basalt parent would reduce the P_2O_5 levels resulting from crystallization alone.

Selective dissolution of ~1 wt. % of apatite, however, would achieve the observed enrichments in phosphorus without modifying the other major elements. Very little apatite has actually been observed in the CFE andesites, even as microlites. The apatite that is present is in the form of inclusions in other minerals, usually clinopyroxene or magnetite. Based on observed magnetite compositions, mass balance calculations indicate that adding 2 to 3 wt. % magnetite would achieve the slight enrichments in Ti and Mn observed in the CFE andesite. However, given the observed proportions of apatite to magnetite in the coexisting pairs (figure 17), adding the 1% apatite along with its magnetite host would far exceed the observed enrichments in Ti, Mn, and Fe. Analyses of the CFE andesite matrix are similar to whole rock analyses, confirming that the phosphorus is indeed dissolved in the melt

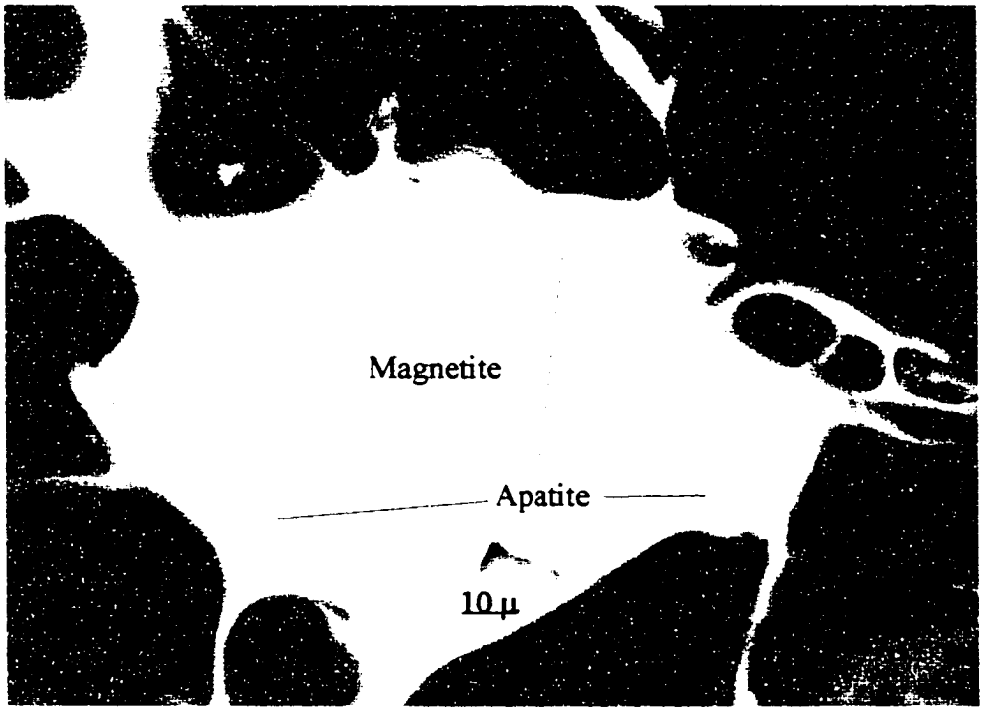

Figure 17: Backscatter electron image of magnetite with apatite inclusions in CFE rhyodacite pumice.

phase. Given the failures of crystallization differentiation, source inhomogeneities, and crustal contamination in explaining the phosphorus enrichments, self-contamination of the hybrid andesite must be considered.

3.6.2 A Model for Mixing-Induced Self-Contamination

Snyder and Tait (1996) and Wiebe (1996) described basalt flows across the base of more silicic magma chambers in layered mafic and silicic intrusions. Snyder and Tait (1998) have recently proposed a novel mechanism for the selective contamination of silicic magmas by influxes of basalt. In their experiments, Snyder and Tait (1998) show that basalt flows separate into parallel fingers perpendicular to the flow front. At the same time, a layer of the host magma becomes trapped beneath the advancing basalt flow. Due to gravitational instability, the trapped silicic layer percolates upward between the fingers, exchanging mass through diffusion along the way. In addition to initiating diffusive contamination of the host magma, heat from the incoming basalt drives thermal convection in the overlying silicic magma, leading to rapid dispersion of the contaminated silicic magma into the host (Snyder and Tait, 1998). In this way, elements with high diffusivities are more efficiently enriched in the host magma. While any single basalt influx may not drastically alter the composition of the host magma by this mechanism, a series of basalt influxes can have significant cumulative effects. Examples given by Snyder and Tait (1998) using geologically reasonable parameters show that after ten to twenty basalt injections, concentrations of some elements can be increased by an order of magnitude or more.

Marsh (1996) outlined a model of magma chamber crystallization in which a solidification front forms in response to inwardly advancing isotherms. The

temperature gradient along the margins results in a range of crystallinities, and thus of liquid compositions. Near the outer margins of the chamber, a crystal-rich region with highly evolved (high SiO_2) liquid forms. Further from the margin, the solid fraction decreases, and the melt composition approaches that of the bulk melt in the interior of the chamber (figure 18). At some intermediate distance, a point of critical crystallinity is reached; between the chamber wall and the point of critical crystallinity, the magma has the rheology of a porous solid, but remains more fluid on the interior side of the critical crystallinity point. In an andesitic chamber, melt compositions within the solidification front may vary considerably both in major and trace elements. The interior of the chamber remains unchanged as long as the thermal gradient advances inward enough to initiate chemical disequilibrium. Thus a hybrid magma may retain relict crystals from the mixing endmembers in the eruptable portion of the chamber interior, while phases crystallizing in equilibrium with the hybrid magma would be confined to the chamber margins. For example, in the CFE andesites, two populations of plagioclase evidently derived from basalt and rhyodacite are present, while crystals preciptated in equilibrium with the andesite are scarce.

Observations of Snyder and Tait (1998) show that the trapped layer of host melt is thin, i.e., the distance between the bottom of the basalt flow and the solid floor of the chamber is small. This means that, in the case of basalt intruding an andesitic chamber, the basalt likely flows across a horizon near the critical crystallinity. In this case, the basalt would trap not only a thin layer immediately beneath the flow, but any interstitial melts present in the supercritically crystalline zone beneath as well. Being of higher density the basalt serves to increase the pore pressure of the fluid in the "mush zone" by an amount

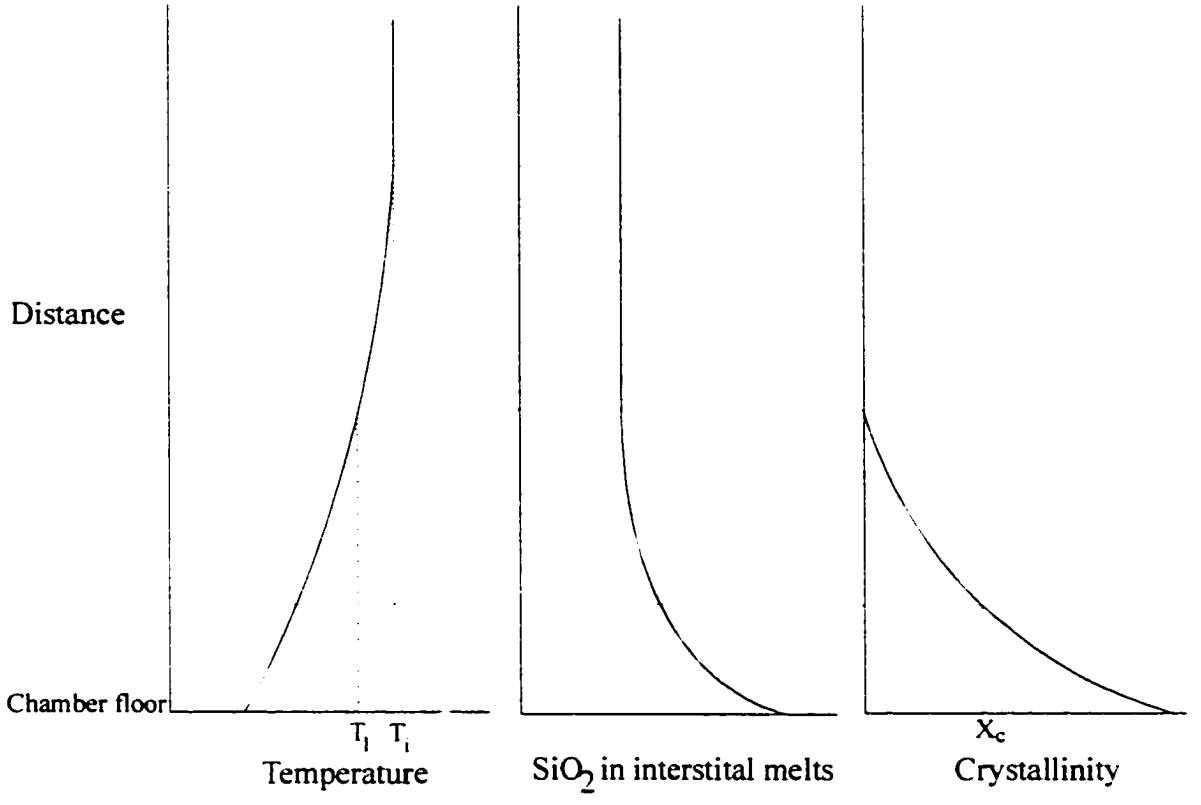

Figure 18: Schematic diagram of the relationship between temperature, silica content in the melt, and crystallinity versus distance from the chamber margin. Melt composition and crystal mass fraction only begin to change when the temperature falls below the liquidus. T_l and T_i represent liquidus and initial temperatures, respectively. X_c represents the level of critical crystallinity.

$$\delta u = g(\rho_b - \rho_a)d \qquad (1)$$

where δu is the increase in pore pressure, g is the acceleration due to gravity (9.8 m s^{-2}) . ρ_b is the density of the basalt, ρ_a is the density of the andesite, and d is the thickness of the basalt flow (Middleton and Wilcock, 1994). Aniakchak basalt 92CNA22 with 0.2 wt% H_2O and CFE andesite with 2 wt.% H_2O have a density contrast on the order of 200 kg m^{-3}. Snyder and Tait (1996, 1998) report field observations of basalt flows in granitic chambers from 1 to 10 meters thick. Pore pressure increases would be on the order of 2 x 10^3 to 2 x 10^4 Pa.

The discharge per unit area from the pressurized mush zone is given by Darcy's law,

$$q = -\left(\frac{k}{\eta}\right)\frac{dp}{dy} \qquad (2)$$

where q is the discharge per unit area, k is the coefficient of permeability, η is the fluid viscosity, and dp/dy is the pressure gradient. The coefficient of permeability is an experimentally determined parameter. For aquifers, the permeability is typically less than 1, although some may reach several darcies; good petroleum reservoirs have permeabilities of a few tens of millidarcies (Middleton and Wilcock, 1994). Permeability of a crystal mush zone increases with distance from the chamber margin. In the following calculation, a value of 0.05 darcy (~5 x 10^{-14} m^2) was used, but this should be considered an upper limit. For a viscosity of 5 x 10^3 Pa s, and a mush zone of 1 m thickness, the resulting discharge is ~1.7 x 10^{-9} m/day, or about 1.7 x 10^{-3} cm^3/day per m^2 of mush zone surface.

The melt expelled from the mush zone has a composite composition consisting of all the compositions present in the supercritically crystalline layer over which the basalt flows. In order to assess the composition of the expelled melt, the compositional gradient, as well as the gradient in melt fraction over the thickness of the mush zone must be known. Towards this goal, the MELTS program of Ghiorso and Sack (1995) was again employed. This time, however, instead of representing the change of an entire magma body with cooling over time, the results were taken to define the changing melt compositions and melt fractions over the distance in which temperature falls from the liquidus to the wall rock interface temperature. The temperature gradient is then used to map compositional changes to distance from the margin.

In the case of a magma chamber in contact with cooler country rocks, heat flows from the magma body into the country rock. As the magma cools from the boundary inward, the wall rock heats from the boundary outward. The result is that the temperature at the boundary is held constant as long as the initial temperature of the magma is maintained in the interior of the magma (Turcotte and Schubert, 1982). The solution to the heat conduction equation for this situation is (Turcotte and Schubert, 1982)

$$\theta = \frac{erfc(\eta)}{1 + erf(\lambda)} \qquad (3)$$

where

$$\theta = \frac{T - T_0}{T_m - T_0} \qquad (4)$$

$$\eta = \frac{y}{2\sqrt{\kappa t}} \qquad (5)$$

$$\frac{L\sqrt{\pi}}{C_p(T_m - T_0)} = \frac{e^{-\lambda^2}}{\lambda(1 + erf(\lambda))} \qquad (6)$$

A list of symbol definitions and appropriate values used is given in table 5. Heat capacity across the mush zone is highly variable due to the changing proportions of liquid and solid. To account for this, the liquid and solid heat capacities for each temperature interval as given by the MELTS output were multiplied by their respective mass fractions and summed to give a bulk heat capacity. A fourth order polynomial function was fitted to the temperature – bulk C_p data. Figure 19 shows a comparison of the data with the function. Using this function along with magma and wall rock temperatures of 1100 and 100° C, respectively, and a latent heat of 210 kJ kg^{-1} (Marsh, 1988), the value of λ was determined by iterative numerical calculations.

Table 5: Symbols and definitions used in numerical analysis of mush zone self-contaminating melt.

Symbol	Definition	Value
θ	Dimentionless temperature	
η	Dimentionless distance	
λ	Dimentionless distance to liquidus	
T	Temperature, C	
To	Wall rock temperature, C	1100
Tm	Magma temperature, C	100
y	Distance, m	
κ	Thermal diffusivity, = k/(Cp p)	
k	Thermal conductivity	5
ρ	Density, kg/m^3	2600
t	Time, s	
L	Latent heat of crystallization, kJ/kg	210
Cp	Heat capacity, kJ/kg K	

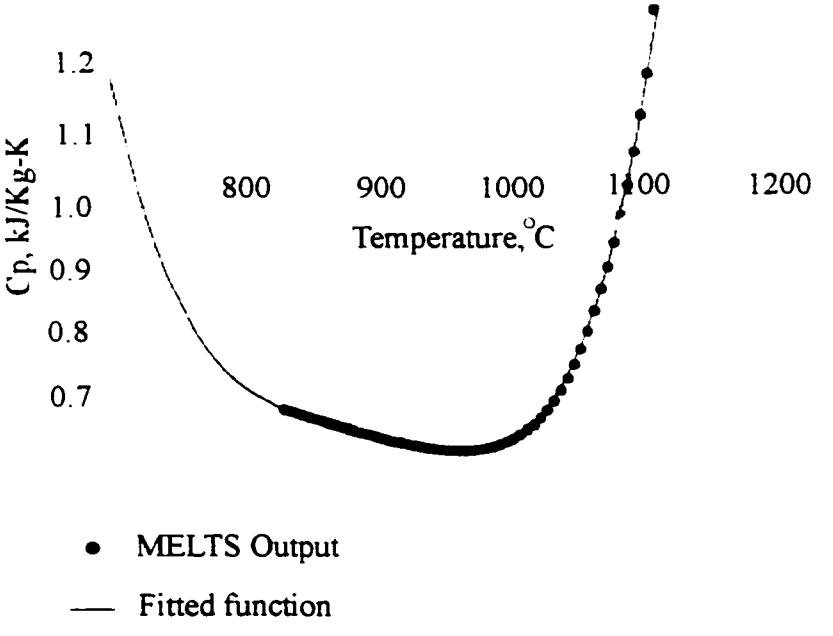

Figure 19: Comparison of bulk Cp data obtained from MELTS and a fourth order polynomial function fitted to the data. The function is used in modeling the temperature profile from chamber margin to chamber interior.

After also solving the thermal diffusivity, $\kappa = k/\rho C_p$, using k = 5 and density values from the MELTS output, equations 4 and 5 can be substituted into equation 3 to obtain a function of T which depends on y and t. A plot of the temperature profiles using different values of latent heat of crystallization (L) is given in figure 20. The main difference caused by increasing the value of L is to shift the interface temperature to higher values. This function was then rearranged to get a function y(T, t). The time variable affects the total distance from wall to liquidus isotherm, but does not affect the shape of the tmperature gradient. This means that while the total mass of melt available for expulsion increases, the mass of melt within any particular temperature increment increases proportionally, so the composition of the composite melt is constant. Using the temperature values from the MELTS output as arguments to this function, each compositional step in the MELTS results was assigned a distance from the chamber margin. The calculated interface temperature in this temperature gradient was always similar to the lowest temperature at which MELTS was able to find a solution, while the starting temperature of the MELTS run was the liquidus temperature. Thus, the MELTS output sufficiently spans the spatial range predicted by the temperature gradient calculations. The new distance vs. composition data set was filtered to include only that portion that is supercritically crystalline. Marsh (1981) suggests values between 0.25 to 0.5 are appropriate for silicate melts. All data points with solid mass fractions less than 0.5 were removed from the data set.

With the filtered data set, the composite composition of the interstitial liquid can then be calculated. Each oxide weight fraction in the MELTS output was multiplied by the liquid mass in each step, giving the total mass of each oxide in the liquid in each increment of distance. After numerically fitting interpolating functions

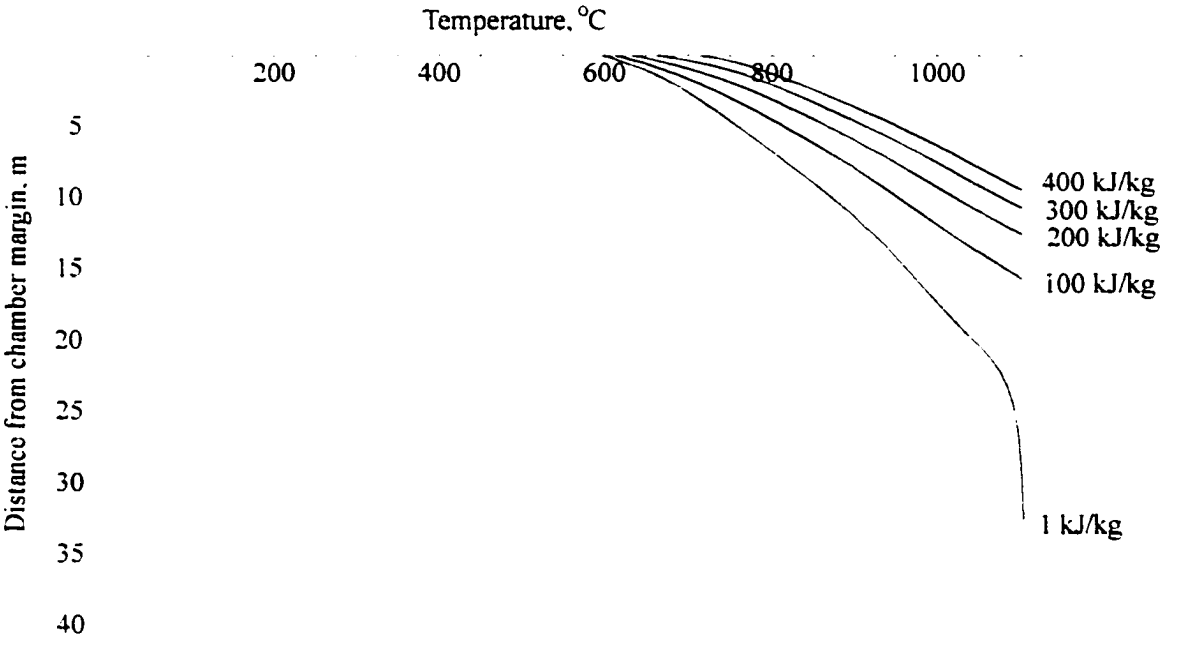

Figure 20: Temperature profiles of magma with initial temperature of 1100 °C and a wall rock temperature of 100 °C. The different curves represent profiles calculated with various values for latent heat of crystallization (L), given by the numbers at the right of each curve.

to each oxide mass vs. distance, the functions were numerically integrated over the distance between the wall and the point of critical crystallinity. A similar integration was performed for the total liquid mass. The result of each oxide mass integration was divided by the total mass integration to obtain a weight fraction oxide of the composite liquid. Using an initial composition determined by taking equal masses of HAB and rhyodacite, the predicted composition of the melt expelled from the mush zone is given in table 6. Note that it is similar in many respects to that of the CFE rhyodacite. Of particular interest, however, is the elevation of P_2O_5 to levels 3 to 4 times that in the CFE rhyodacite. Given the starting composition of the hypothetical hybrid, MELTS did not predict apatite crystallization. As interstitial melts are expelled in small increments back into the main chamber, the starting P_2O_5

Table 6: Calculated composition of mush zone melt expelled into main chamber after basalt intrusion.

Oxide	Wt. %
SiO2	70.34
TiO2	0.79
Al2O3	12.33
Fe2O3	0.38
FeO	2.07
MnO	0.41
MgO	0.47
CaO	3.28
Na2O	3.06
K2O	3.87
P2O5	0.42

concentration rises, albeit slowly. Using the phosphorus-enriched CFE andesites as a starting composition, MELTS does predict apatite saturation. The point at which P_2O_5 concentrations in the starting melt lead to apatite saturation in the mush zone is intermediate between 0.18 and about 0.6 wt. %. Once the mush zone begins to crystallize apatite, the residual melt will contain less P_2O_5. However, if the basalt flows can heat the mush layer faster than melts are expelled, crystallized apatite can be resorbed into the melt.

Considering compositional evolution of a magma body to occur in cycles of replenishment, self-contamination, and eruption (e.g. O'Hara, 1977; O'Hara and Matthews, 1981), the concentration of component i in the main part of the chamber is given by

$$C_n^i = C_{n-1}^i M_{n-1} + C_b^i M_b + C_s^i M_s + C_c^i M_c - C_e^i M_e \qquad (7)$$

where C^i and M are concentration of component i and mass of a particular contribution to the system. Subcript n refers to the cycle number, b and s refer to basaltic and silicic inputs, respectively. Subscript c refers to the self contaminating fluid expelled from the mush zone, and e refers to the erupted magma.

The time interval between replenishment events plays a critical role in determining the compositional evolution of the hybrid magma. Longer repose periods between injections allows a greater mass of interstitial liquid to be generated in the growing solidification front at the chamber margins. As discussed in chapter 3, if the mass eruption rate is less than the total mass injection rate, the total mass of the system increases. This has the effect of slowing the eruption rate even further, as larger host volumes require larger input volumes to overstress the chamber walls to

the point of eruption. If the mass influx rate continues at a constant rate, while the eruption rate slows, this allows the effects of the self-contaminating melt to build up in the main chamber.

Because the rates of magma injection and eruption at Aniakchak are not known, it is difficult to make a meaningful quantitative estimate of the compositional evolution of the system. However, it is not difficult to see in qualitative terms that most major elements in the contaminating melt are not very different from that in the rhyodacites. Thus the effect of the contaminant on the hybrid is not much different than that of the silicic replenishment alone. P_2O_5 and MnO are significantly elevated in the contaminant relative to the rhyodacites. Given sufficient time these components can accumulate in the host hybrid melt.

One further speculation is that rhyodacite as well as basalt influxes could lead to the expulsion of mush zone melts from chamber margins. Buoyant pressure of silicic intrusions against the roof of the chamber may produce similar melt expulsions downwards into the host chamber.

3.7 Conclusion

The complex, and in the case of plagioclase, bimodal mineralogy of the CFE andesites suggests a mixing origin for the CFE andesite. Periodic inputs of both high-alumina basalt and rhyodacite can account for much of the compositional variation between these two endmembers in the Aniakchak data suite. Models of crystallization differentiation alone fail to reproduce the compositional trends of the suite in general, and of the CFE andesite in particular. Mixing, on the other hand, could generate much of the observed composition and mineralogy of the andesites. Some chemical

components (e.g., P_2O_5, REE) are elevated above the concentrations expected from binary mixing alone. Comparison of these concentrations with highly incompatible elements in the CFE andesite indicate that they have been added into the magma rather than just being less efficiently depleted by fractionation processes than in other andesites. The lack of basalts with suitable compositions at Aniakchak casts doubt on the possibility of an "odd" mafic endmember to mixing. The elemental enrichments in the CFE andesites increase in spite of constant LILE/HFSE ratios, so it is unlikely that an excess hydrous fluid component, either in the mantle source of the mafic endmember or from a crustal hydrothermal system, is responsible for the increased concentrations of certain elements. An appealing alternative is the addition of an "apatite component" from the crystallizing margins of the magma chamber. Modeled interstitial melts in the crystal mush zone have compositions similar to the rhyodacitic mixing endmember, but are enriched in phosphorus by up to 300 %. As these melts are expelled from the mush zone during replenishment events, the compositional effects are small, but these enrichments accumulate in the host melt as long as the eruption rate is smaller than the total influx rate. The composition of the CFE andesite is well explained, then, by the periodic additions of mafic and silicic magmas, which over time led to the enrichment of an apatite component.

Chapter 4: Petrology of the Aniakchak CFE Rhyodacite

4.1 Introduction

The origin of silicic magmas is an intriguing problem in igneous petrology. Highly evolved melts could potentially be produced by a number of mechanisms at various places in the crust. Crystallization differentiation of a basaltic to andesitic parent could produce rhyolite (Brophy and Dreher, 2000). Partial melting of a mafic pluton at deeper crustal levels could also generate silicic melts (Borg and Clynne, 1998; Tepper et al., 1993). Partial melting of granitic country rocks at shallow depths might also produce high-SiO_2 magmas. Each of these processes has petrological implications for crustal evolution. Crystallization of mafic parents leads to addition of mantle-derived materials to the crust, while partial melting of deep plutonic bodies and segregation of resulting melts redistributes mass into shallower crustal levels. In either case, production of highly evolved melts implies that melt fraction is low, often on the order of 10 wt. % or less of the parent magma or melting pluton. Thus, an initial mass of parent magma or pluton at least ten times the mass of erupted silicic magmas is required (Knesel and Davidson, 1997).

In addition to the petrological implications of silicic magma genesis, volcanologists are interested in the typically explosive nature of silicic magma eruptions. As erupting magmas become more viscous and more volatile-rich – both of which correlate with increasing SiO_2 concentrations – the eruptions become more violent. Aniakchak has demonstrated its proclivity for explosive eruptions in its most recent eruption in 1931 (Hubbard, 1931). Such events can have great impacts on air traffic as well as on surrounding communities such as Meshik, Alaska. It is important

to identify the nature of silicic magmatism at Aniakchak: a volcano that has both a history of explosive activity, and which has generated a rather large volume of evolved magma in the Holocene epoch.

The caldera-forming eruption of Aniakchak released a volume of at least 34 km^3 of rhyodacitic tephra, approximately 12 km^3 DRE, along with a similar volume of hybrid andesite (this study, chapter 1). While banded pumices are fairly common in the CFE ignimbrite, no homogenous pumice with composition intermediate to the andesite and rhyodacite has been found. Several rhyodacite lavas and the Black Nose pumice were erupted during the late precaldera period. All of these lavas and tephras are geochemically and mineralogically similar. The lavas contain a greater proportion of crystals, but all appear to have experienced a simple history between separation from their source and eruption. This chapter will describe the mineralogy and geochemistry of the CFE rhyodacite as well as estimates of its liquidus and eruptive temperatures. A similar assessment of the late precaldera rhyodacites is also presented for comparison with the CFE rhyodacite. Various mechanisms for rhyodacite production are then discussed in light of the petrological data. Models of crystallization of basalt and partial melting of gabbroic plutons are compared. A model is developed in which rhyodacite magmas from deeper crustal levels periodically replenish the shallow chamber beneath the volcano, buffering the host andesite composition against basaltic injections. During the caldera forming event an atypically large volume of silicic magma intruded the andesite chamber and erupted, destabilizing the roof, and leading to the evacuation of most or all of the chamber. This happened rapidly enough that the two magmas only had time to mingle, not mix.

4.2 Mineralogy of the CFE Rhyodacite

The phenocryst assemblage in the CFE rhyodacite comprises plagioclase, orthopyroxene, magnetite, and minor amounts of ilmenite and hornblende. Mass balance calculations based on whole rock, glass, and mineral compositions suggest the rhyodacites contain around 2% crystals, predominantly plagioclase. The groundmass is glassy and nearly microlite-free (figure 21).

The anorthite content in the rhyodacite plagioclase cores define a single population, ranging from An_{15} to An_{55}, with most (46 out of 74 analyzed) between An_{35} and An_{45} (figure 8). The mode of this population is between An40 and An45. Composition profiles (figure 22) from plagioclase cores to rims show slight reverse zonation with oscillatory zonation superimposed over the trend of increasing calcium. As figure 22 shows, the difference in the anorthite component between the rim and core is less than a few mole %. Although criteria for plagioclase equilibrium are poorly constrained (Housh and Luhr, 1991), single narrow compositional populations are interpreted to reflect equilibrium between plagioclase and melt (Brophy, 1987; 1990; Sakuyama, 1981). Melt inclusions in plagioclase have major element compositions very close to the whole rock and glass compositions (Dreher et al., 1997), indicating that very little chemical change has occurred in the melt phase since crystallization began. Crystals in the rhyodacite are often broken, but rarely show disequilibrium textures.

Strontium, barium, and europium concentrations in plagioclase were measured using a Micromass laser ablation inductively-coupled plasma hexapole mass spectrometer at Michigan State University. A 100-micrometer laser spot was used, and five spots were analyzed in each plagioclase crystal. Spots were chosen such that

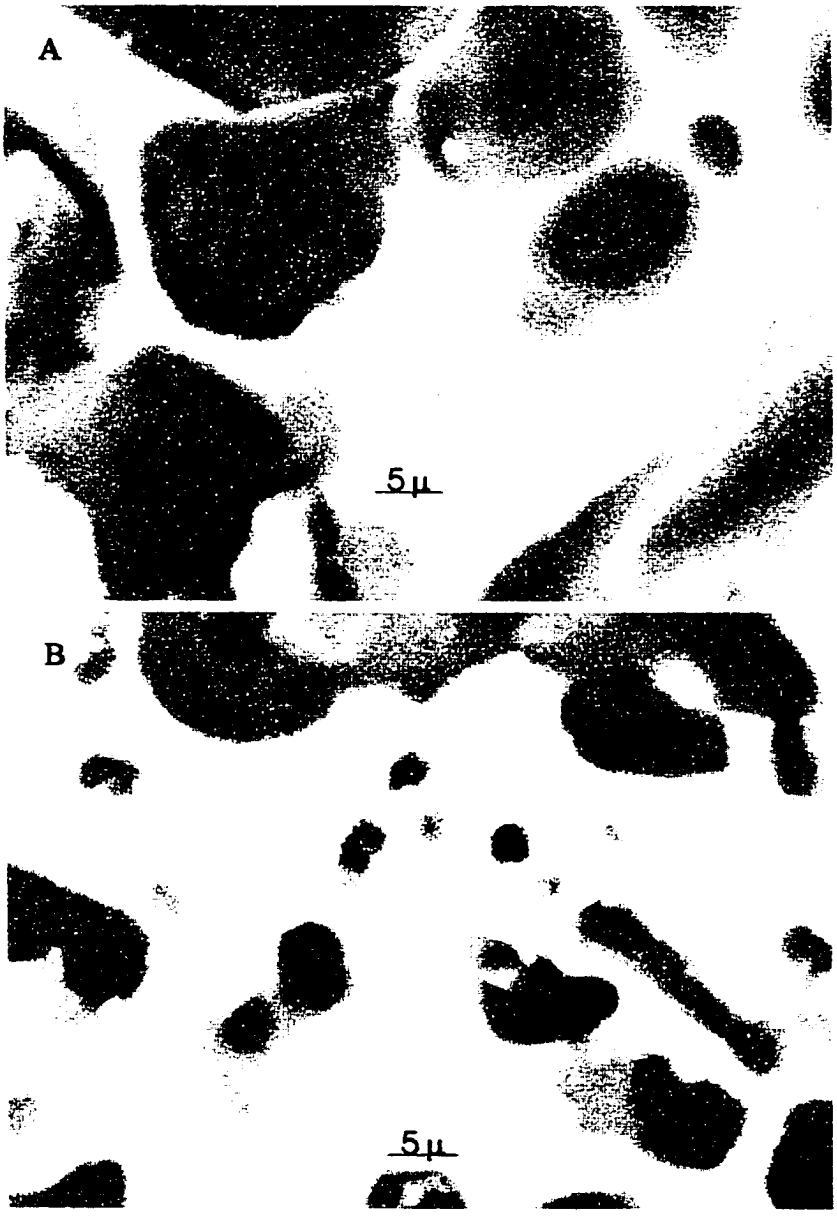

Figure 21: Backscatter electron images of CFE rhyodacite groundmass (panel A). Panel B shows the groundmass of CFE andesite for comparison.

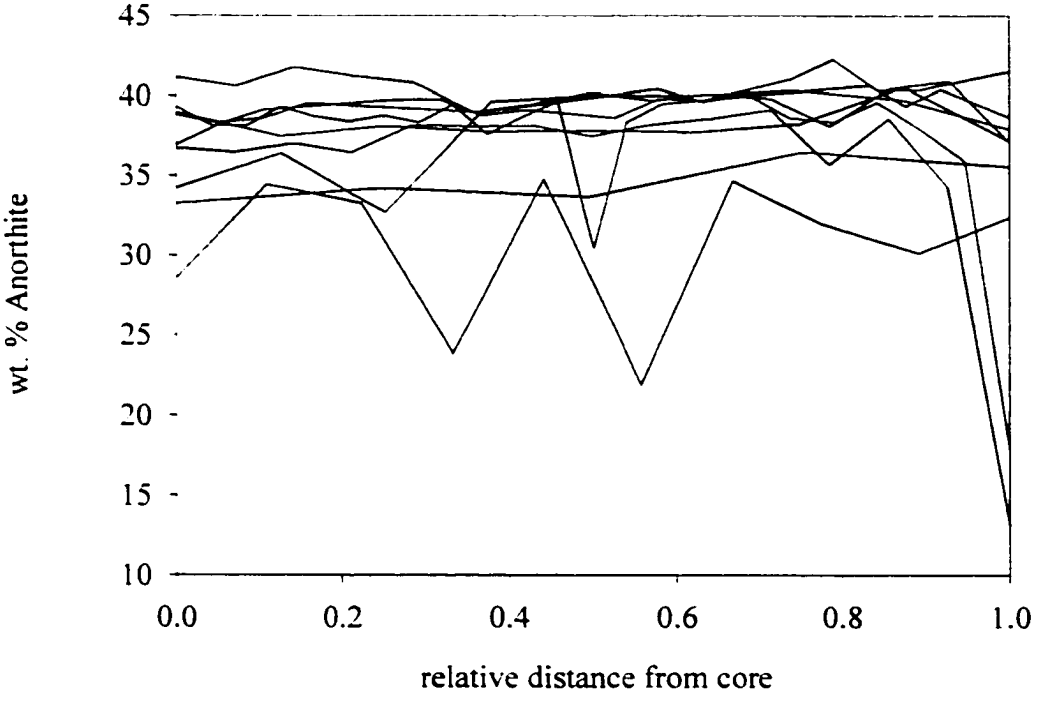

Figure 22: Plagioclase profiles from CFE rhyodacite.

they spanned the width of the crystal from one rim to the other, following the same path used to collect electron microprobe data for major elements. Eu concentrations range from 2.7 to 4.1 ppm, with a mean concentration of 3.4 ppm. Ba levels are between 363 and 595 ppm, with a mean value of 515 ppm. Finally the range of Sr concentrations is 900 to 1322 ppm, and a mean concentration of 1140 ppm. These concentrations are plotted against wt. % CaO in figure 23. Similar data from a late precaldera rhyodacite lava are shown as well for comparison.

Orthopyroxene is the only major ferromagnesian phase present, although traces of hornblende have been noted. Orthopyroxene compositions are typically in the range $En_{63-65}Fs_{32-35}Wo_{3-4}$. Molar Mg numbers $\left(100 \times \frac{MgO}{MgO + FeO}\right)$ are between 64 and 68. Fe/Mg $Kd^{opx\text{-}melt}$ values in CFE rhyodacite are between 0.20 and 0.24, with most between 0.21 and 0.23. FeO in the orthopyroxene was calculated from total FeO based on stoichiometry (e.g., Droop, 1987). Whole rock FeO and Fe_2O_3 concentrations were determined using the method of Sack et al. (1980) using temperatures and oxygen fugacities determined by coexisting iron-titanium oxides (Stormer, 1983; Andersen and Lindsley, 1988). Comparing these results to the range of equilibrium values reported by Grove et al. (1982) of 0.27 to 0.30, suggests that the orthopyroxene did not crystallize from this magma. On the other hand, Beard and Lofgren (1991) found Fe/Mg $Kd^{opx\text{-}melt}$ values between 0.19 and 0.20 for orthopyroxene and melt derived from water-undersaturated partial melting of amphibolite. As discussed below, crustal melting provides an attractive mechanism for generating at least part of the mass of rhyodacite erupted at Aniakchak.

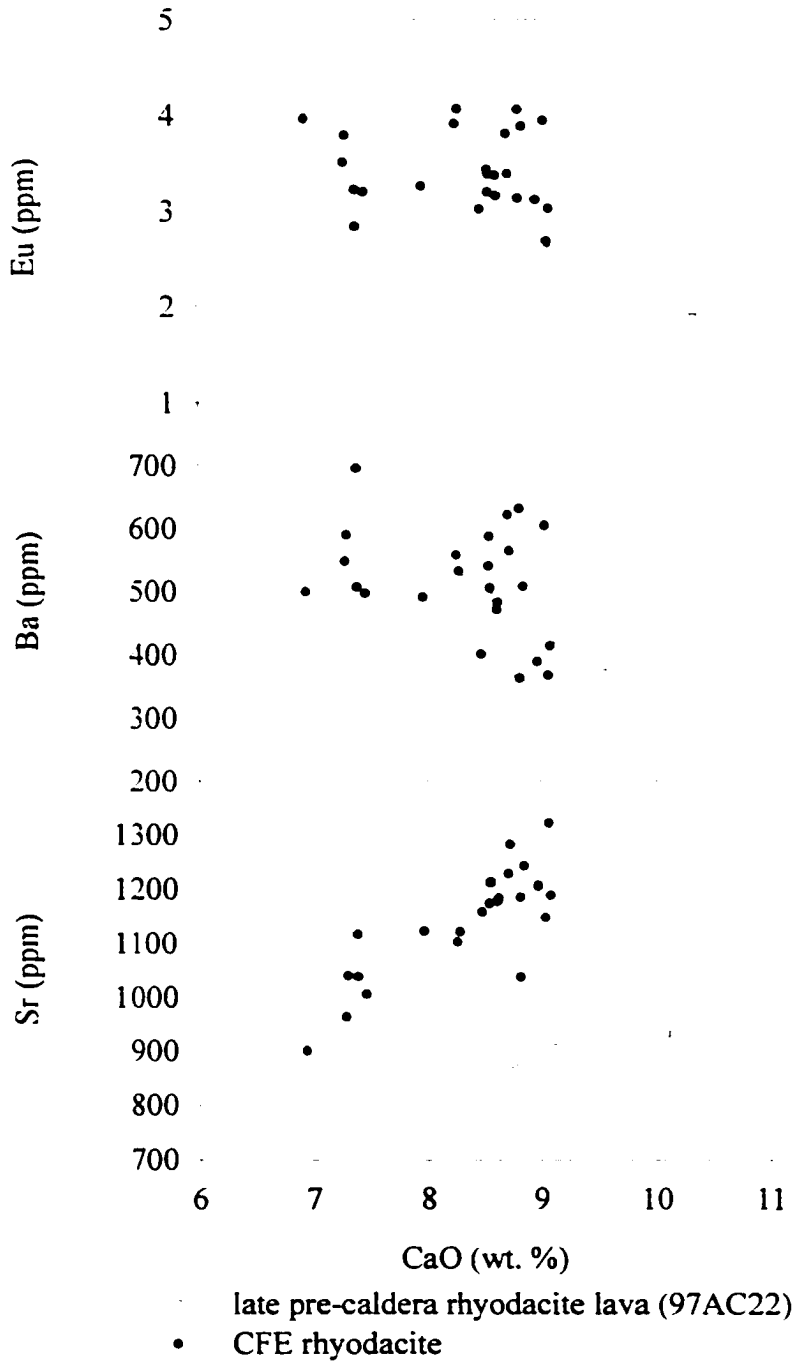

Figure 23: Selected trace elements in plagioclase in CFE and late pre-caldera rhyodacite. Concentrations determined by laser ablation ICP-MS at Michigan State University.

4.3 Whole Rock Geochemistry

Silica content of analyzed CFE rhyodacite pumice samples ranges from 67 up to 70 wt. % (figure 11, and appendix 1). This is the highest SiO_2 concentration of all analyzed samples from Aniakchak. CFE rhyodacite contains 0.5 to 1.0 wt. % MgO. The rhyodacite is quite homogeneous: for Al_2O_3, FeO, CaO, and Na_2O, the scatter in concentrations is within 1 wt. %. TiO_2, K_2O, and P_2O_5 concentrations differ by no more than a few tenths of a wt. %. On MgO variation diagrams, the CFE rhyodacite represents the most evolved end of the data array. For all major elements, both pre- and post-caldera data sets extend to and are continuous with the low-SiO_2 portion of the CFE rhyodacite data.

Figure 12 shows a similar homogeneity in trace element data to that in the major elements from CFE rhyodacite samples. As in the major elements, the CFE rhyodacite samples extend the trends in trace elements from the pre- and post-caldera data from Aniakchak. CFE rhyodacites contain 60 to 70 ppm Rb, between 800 and 900 ppm Ba, 200 to 260 ppm Sr, around 240 ppm Zr, 1.8 to 2.2 ppm Eu, and a few tens of ppm V.

Using temperatures estimated from Fe-Ti oxide compositions, and plagioclase and whole rock compositions, the equations of Housh and Luhr (1991) were used to estimate water contents in CFE rhyodacites. Results from the equations were identical at 3 and 7 kb pressures. From the anorthite component in plagioclase, an H_2O concentration of 4.13 wt. % is predicted. A concentration of 3.75 wt. % H_2O is predicted from the albite component in plagioclase.

The continuity of the CFE rhyodacite data with that of the rest of the Aniakchak data set bespeaks some genetic relationship with the rest of the sample

suite. Although plagioclase and whole rock compositions suggest that the CFE andesites are hybrids between nearly equal portions of rhyodacitc and basaltic magmas. CFE rhyodacite and andesite have nearly identical strontium and neodymium isotope ratios.

The $^{87}Sr/^{86}Sr$ ratio in CFE rhyodacite is 0.70340; in the CFE andesite $^{87}Sr/^{86}Sr$ is 0.70333. $^{143}Nd/^{144}Nd$ is 0.51308 in the CFE rhyodacite, and 0.51313 in the CFE andesite (George et al., 2001). For the hybrid to have the same isotopic signature as the silicic endmember, the basaltic endmember must also share this signature. In order for both mixing endmembers to have the same isotope signatures, the rhyodacite must be derived from the basalt by fractional crystallization, or from partial melting of a pluton young enough to still have the same isotopic ratios as the basaltic magma. Both processes produce melts approaching the eutectic composition, and it is thus difficult to distinguish between them on the basis of major element compositions. For example, although major element mass balance calculations allow the production of CFE rhyodacite by fractional crystallization of a basaltic magma (see below), Beard and Lofgren (1991) have experimentally reproduced low-K dacitic melts that are quite similar to typical arc dacites by dehydration melting of amphibolite at pressures up to 7 kb. Trace elements are more sensitive than major elements to the solid assemblage in equilibrium with the melt, however, and are useful in differentiating between crystallization and partial melting as petrogenetic mechanisms in rhyodacite formation. In addition, several late pre-caldera rhyodacitic lavas and tephras have been sampled which have similar compositions and mineralogies to that of the CFE rhyodacites. Assuming these silicic magmas all were formed by similar processes, they can be compared to the CFE rhyodacites to elucidate the origins of Aniakchak

silicic magmas.

4.4 Temperature Estimates for the CFE Rhyodacite

Magnetite is common in the CFE rhyodacite, but ilmenite is rare. Using coexisting magnetite-ilmenite pairs, temperatures have been estimated using the equations of Stormer (1983) and Andersen and Lindsley (1988). Results from three pairs indicate temperatures of 888, 895, and 898 °C. Compositional data for the magnetite and ilmenite grains are given in appendix 4. Corresponding calculated log (fO_2) values are −11.8, -11.8, and −11.7, near the NNO + 1 buffer curve. Using the MELTS program (Ghiorso and Sack, 1995), liquidus temperatures are estimated to be 929 °C at 3 kb pressure, and 953 °C at 7 kb pressure. That the eruptive temperature of the rhyodacite is close to its calculated liquidus is in good agreement with petrographic observations and melt inclusion data, which also suggest that the rhyodacitic magma has been little modified by crystallization since its segregation from its source. Temperature data are summarized in table 4.

4.5 Late Precaldera Lavas and Tephras

Several late precaldera dacitic to rhyodacitic lavas and pumice deposits in the caldera walls and on the upper flanks have been examined for comparison to the CFE rhyodacite. The group of lavas comprises three separate lava flows. The collapse of the caldera dissected one lava dome (99AC26), now exposed high in the eastern caldera wall. The age of this sample is constrained by the underlying Aniakchak I ignimbrite to be younger than ~8000 years (Miller and Smith, 1987) and older than

the 3500 year old CFE. Two lava flows are exposed in stream valleys on the northeast (97AC22) and northwest (97ANB45) flanks, respectively. The lava on the northeast flank is also overlain directly by lag breccia produced by the caldera formation. The Black Nose Pumice, exposed on the eastern caldera rim on the north side of the Gates immediately beneath lag breccia produced by the caldera formation, consists of upper and lower units. The upper pumice fall unit (97AC19) is dark brown, less silicic and more crystal rich than both the lower unit and the CFE rhyodacite. The lower unit (97AC14) is a buff- and pink-colored pumice fall containing less than 10 wt. % crystals. These rocks range in composition from 67.2 wt. % SiO_2 in the upper unit of the Black Nose Pumice to 69.2 wt. % SiO_2 in lava dome sample 99AC26. For comparison, the CFE rhyodacite contains between 68.9 and 70.4 wt. % SiO_2. All three lavas contain plagioclase, orthopyroxene, clinopyroxene, magnetite, and ilmenite, with microphenocrysts of apatite. Rare crystals of quartz in the lavas have rounded corners and resorbed edges, and commonly are surrounded by reaction halos. The two pumices contain plagioclase, orthopyroxene, magnetite, and ilmenite, with minor amounts of clinopyroxene. Limited observations of microlite populations in the lavas suggest that clinopyroxene is absent in the groundmass. The pumice samples are virtually microlite free.

Plagioclase compositions in the lavas are all similar, ranging continuously from approximately An30 to An64. Similarly, precaldera pumice plagioclase compositions range continuously from An32 to An55. The plagioclase analyzed in the CFE rhyodacite span the entire range of precaldera pumice plagioclase compositions (figure 24), and all but the most calcic plagioclase in the lavas. Plagioclase phenocrysts comprise single compositional populations in all samples considered

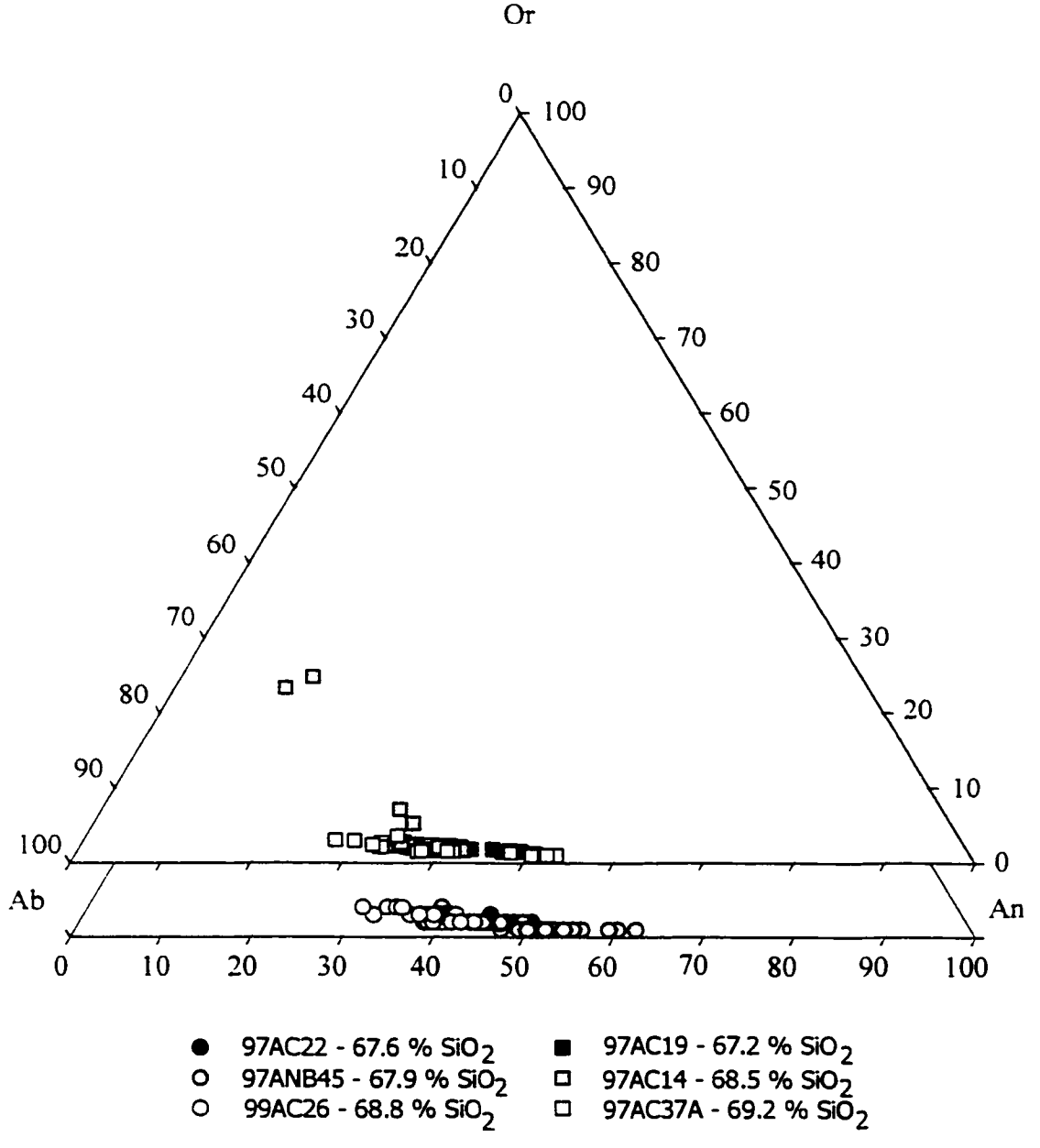

Figure 24: Ternary diagram showing plagioclase compositions in precaldera lavas (bottom) and pumice (top). Sample 97AC37A is a CFE rhyodacite for comparison to the precaldera samples. The silica concentrations in the legend refer to the corresponding whole rock composition.

here. Crystals do not commonly show textural signs of disequilibrium such as sieve textures. Although the phenocrysts are often broken, especially in the pumices, they rarely have embayed or resorbed edges.

Trace elements in five plagioclase crystals from one precaldera lava were determined. The concentrations of Eu, Ba, and Sr, in this sample are generally lower than in the CFE rhyodacite. Eu ranges from 1.6 to 3.1 ppm, and has an average concentration of 2.3 ppm. Ba ranges from 280 to 521 ppm, with an average concentration of 399 ppm. Sr levels are between 781 and 991 ppm, with an average of 903 ppm. Figure 23 shows a fairly consistent separation of the late precaldera rhyodacite flow data from that of the CFE rhyodacite. Although there is minor overlap in the Eu and Ba data, the precaldera and CFE Sr data are very cleanly separated from each other. The slopes of the trends in Sr vs. CaO are also different between the two sets of data.

Figure 25 shows pyroxene compositions for the same group of rocks. Like the plagioclase compositions, each of the three lavas contains a single population of both clinopyroxene and orthopyroxene. Sample 97ANB45, the northwest flank lava flow and intermediate of the three lavas in whole rock composition, contains more magnesian orthopyroxene than the other two. Pyroxene compositions in the pumices and lavas are broadly similar.

Published equilibrium Kd values of 0.27 to 0.30 for orthopyroxene (Grove et al., 1982) and 0.23 to 0.26 for clinopyroxene (Grove and Bryan, 1983) are used as the criteria for testing equilibrium between pyroxene phenocrysts and host lavas and tephras. Average $Kd^{opx\text{-}melt}$ in the samples considered range from 0.19 to 0.26. The range of average $Kd^{cpx\text{-}melt}$ is 0.15 to 0.20. Whole rock compositions were used as a

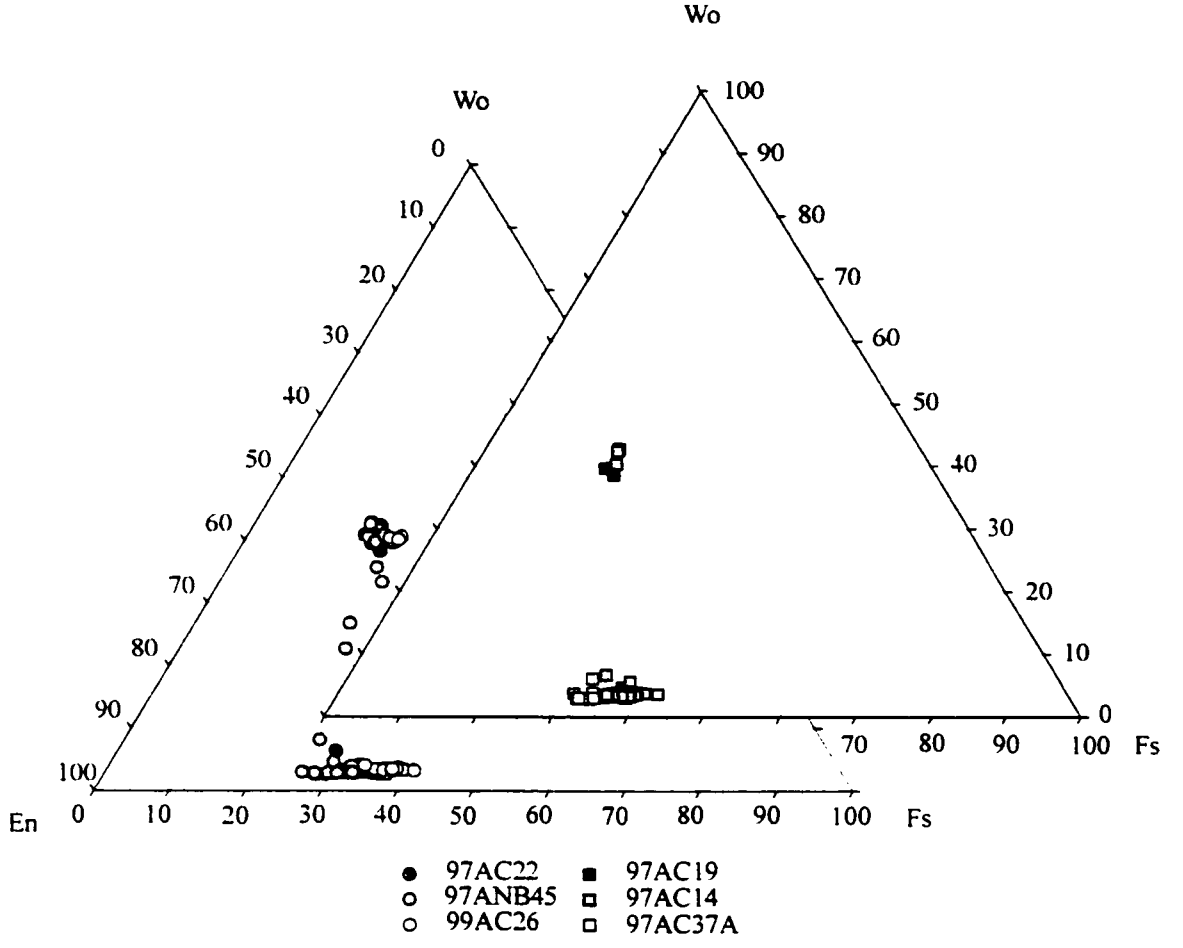

Figure 25: Ternary diagram showing pyroxene compositions in precaldera rhyodacitic lavas (left) and pumice (right). Sample 97AC37A is a CFE rhyodacite sample for comparison.

proxy for liquid compositions. Since FeO/MgO ratios are expected to be slightly higher in the matrix glass than in the whole rock, these values represent an upper limit. FeO abundances in the minerals were calculated from stoichiometry (Droop, 1987); those in the whole rocks were determined by the method of Sack et al. (1980) assuming temperatures and oxygen fugacities determined from coexisting Fe-Ti oxides. In the lavas, clinopyroxene crystals are commonly rimmed by orthopyroxene. The thicknesses of the orthopyroxene rims is on the same scale as the length of orthopyroxene microlites in the lava groundmasses; the rims likely formed during ascent and cooling of the lava.

Pre-eruptive water contents calculated from the plagioclase-melt equilibrium equations of Housh and Luhr (1991) range from 3.8 to 4.5 wt. % based on the Ab component in the lavas, and 4.4 to 4.7 wt. % based on the An component, assuming a temperature of 900°C. These values are similar to those estimated for the CFE rhyodacites, as discussed above as well as measured water content measured in melt inclusions from rhyodacites erupted in 1931 of 4.1 wt.% (Bacon, 2000).

The whole rock chemical compositions of precaldera samples overlap the compositional range shown by the CFE rhyodacite sample collection. Compositional data for these rocks are given in table 7. Although major elements in the pre-caldera rhyodacites are continuous with the compositional field of the CFE rhyodacite, there is much more variation in trace elements. Each of the five pre-caldera rhyodacites is distinct from the others; the compositions of the five rhyodacites do not vary in any systematic way. The lava dome in the caldera wall (99AC26) and the lower Black Nose Pumice (97AC14) contain similar SiO_2 concentrations to the CFE rhyodacite, but contain greater abundances of incompatible trace elements, as shown in figure 26.

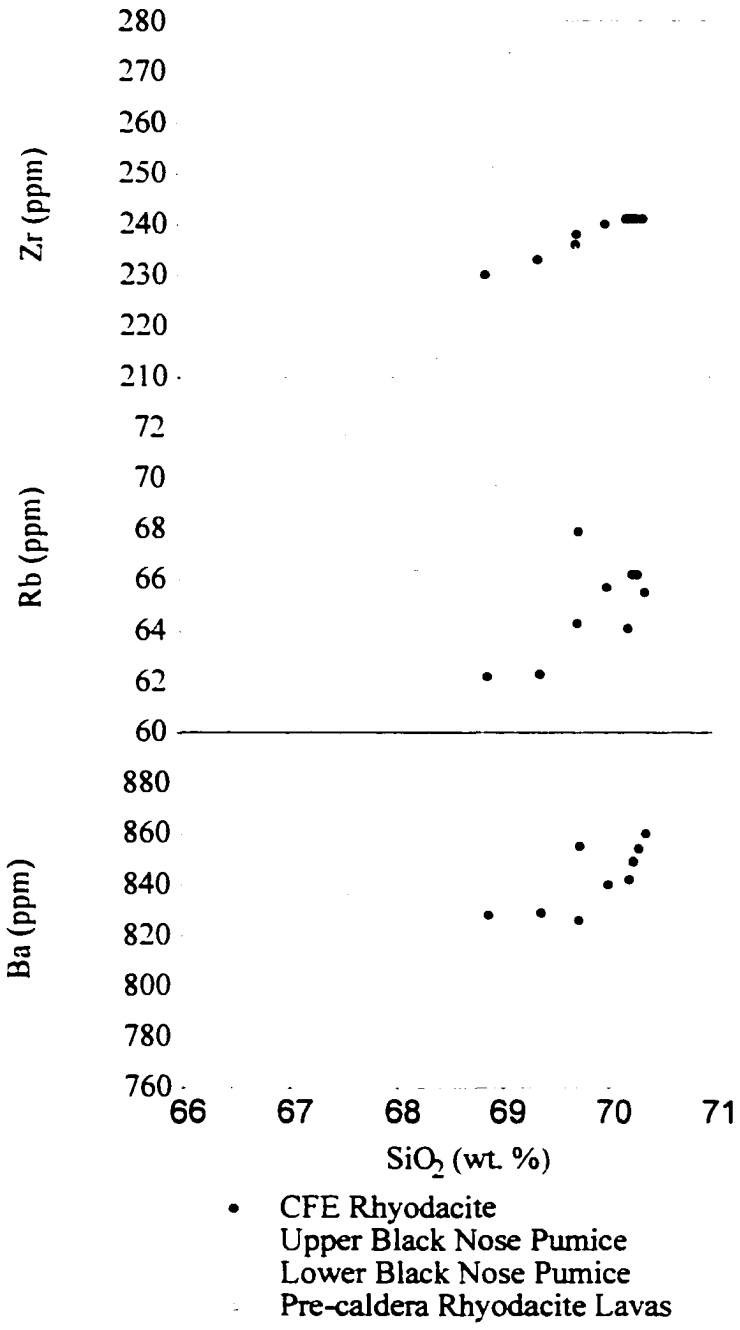

Figure 26: Selected trace element concentrations in CFE and late pre-caldera rhyodacite samples.

In those samples with lower SiO_2 than the CFE rhyodacite, Rb is higher than in the CFE rhyodacite despite being a very incompatible element. With the exception of the northwest flank lava (97ANB45), Zr is also higher in pre-caldera rhyodacites. In contrast, for both elements, the CFE rhyodacite sample suite shows a positive correlation between SiO_2 and these incompatible elements, probably a result of variations in the crystal content of individual pumice fragments.

Table 7: Major element compositions of late precaldera rhyodacite lavas and pumice.

SAMPLEID	97AC-22	97ANB45	99AC26	97AC-14	97AC-19
SiO2	67.55	67.88	68.76	68.48	67.21
TiO2	0.827	0.711	0.694	0.733	0.850
Al2O3	15.53	15.35	14.81	14.87	15.37
FeO	2.85	2.72	2.73	2.79	3.10
Fe2O3	0.995	0.946	0.996	1.008	1.082
MnO	0.151	0.148	0.158	0.159	0.172
MgO	1.10	0.85	0.69	0.74	1.01
CaO	2.85	3.01	2.25	2.30	2.87
Na2O	5.10	4.92	5.21	5.20	5.24
K2O	2.98	2.63	3.09	2.98	2.73
P2O5	0.210	0.182	0.144	0.164	0.224
Total	100.05	99.25	99.43	99.33	99.75

Temperatures estimated from Fe-Ti oxide compositions (Andersen and Lindsley, 1988; Stormer, 1983) range from 980 to 1073 °C in 99AC26. In 97ANB45 the range is 971 to 1073 °C. Sample 97AC22 gives estimates between 900 and 1182 °C. The lower Black Nose pumice gives a temperature range of 933 to 948 °C; one oxide pair in the upper Black Nose pumice predicts a temperature of 935 °C. All pairs

used in these ranges passed the Bacon-Hirschmann test (Bacon and Hirschmann, 1988). The two-pyroxene geothermometer of Wood and Banno (1973) was also used for each of the lavas and the upper Black Nose Pumice. These calculations predict temperatures of 1082 °C for 99AC26, 1018 °C for 97ANB45, and 1040 °C for 97AC22. Pumice sample 97AC19 is estimated to have crystallized pyroxenes at a temperature of 1059 °C. Temperature data are summarized in Table 2. FeO and Fe_2O_3 in the pyroxenes were determined by stoichiometry (Droop, 1987). Average orthopyroxene and clinopyroxene compositions from each sample were used in the calculations.

Liquidus temperatures calculated using the MELTS program (Ghiroso and Sack, 1995) are within the ranges estimated from oxide compositions in the lavas, but are higher than the temperatures obtained from the pumice samples. In lava sample 99AC26, the liquidus temperature at 3 kb was estimated at 979 °C and 987 °C at 7 kb. Sample 97ANB45, another lava, is estimated to have a liquidus temperature of 970 °C at 3 kb pressure and 977 °C at 7 kb. The third lava, 97AC22, returned estimates between 982 and 1031 °C, at 3 and 7 kb pressure, respectively. The upper Black Nose pumice is estimated to have a liquidus temperature from 995 to 1023 °C at 3 and 7 kb, respectively, at least 60 °C higher than the temperature estimated from Fe-Ti oxide compositions. The lower Black Nose pumice has a liquidus temperature of 982 °C at 3 kb and 994 °C at 7 kb, between 34 and 61 °C higher than temperatures obtained from magnetite-ilmenite geothermometry. Temperature data are summarized in table 4. Both calculated liquidus temperatures and eruptive temperatures estimated from phase compositions are higher in the precaldera samples than in the CFE rhyodacite.

4.6 Discussion

4.6.1 The Origin of the CFE Rhyodacite

If rhyodacitic magma is a mixing end member in the production of CFE andesite, it is unlikely that it is also derived from the CFE andesite through crystallization differentiation. In addition, the crystal poor nature of both CFE andesite and rhyodacite and the presence of a 10 wt. % SiO_2 composition gap imply that the two magmas encountered each other just prior to the eruption. This still leaves the question of the origin of the rhyodacitic end member. The possibilities include crystallization differentiation of a more mafic parent, partial crustal melting, or some combination involving mixing of distillates and partial melts.

The precaldera rhyodacites are clearly not part of the same batch of magma that produced the CFE rhyodacite. Neither do they represent steps in crystallization differentiation of a single mafic parent. Evolution to higher SiO_2 concentrations by crystallization would lead to a systematic increase in incompatible elements Rb and Zr. The differences between CFE and precaldera rhyodacites in trace element abundances in plagioclase is further support for the hypothesis that the CFE rhyodacite represents a distinct batch of silicic magma.

Although the ages of the individual rhyodacites are poorly constrained, they are all younger than the Aniakchak I ignimbrite, and thus younger than about 8000 years (Miller and Smith, 1987). This leaves a maximum of 4500 years to form all of the precaldera rhyodacites and the CFE rhyodacite, which erupted ~3500 years ago (Miller and Smith, 1987). Turner et al. (2001) have suggested that closed-system crystallization differentiation of basalt to produce rhyolite takes less than a few

thousand years. Even with such short differentiation times, the eruption of at least five different rhyodacitic magmas in less than 5000 years requires multiple simultaneously evolving rhyodacitic bodies. Silicic magma is not necessarily produced in a single, shallow crustal chamber.

These several rhyodacitic magma batches may be produced either by fractional crystallization of distinct basaltic parents or by partial melting of various lithologies in the mid to lower crust. Basaltic underplating has been recognized as an important aspect of crust formation in arc environments (Bergantz, 1989; Zhou and Li, 2000). The Talkeetna Formation in southern Alaska, a Late Triassic – Early Jurassic batholith that represents a cross section through a segment of volcanic arc crust, is composed of mafic and ultramafic plutonic bodies in the stratigraphically lower portions (DeBari, 1997; Nokleberg et al., 1994). There is likely to be abundant source material for silicic melt production in the deeper portions of the present Aleutian arc as well.

In order to test the ability of fractional crystallization to derive Aniakchak rhyodacite from Aniakchak high-alumina basalt (HAB), a detailed model was constructed, following the approach taken by Devine (1995), using the entire data set from Aniakchak, including pre-caldera and post-caldera samples (C Nye, C Neal, C Bacon, unpublished data). First, all major elements were plotted against MgO. Curves were then fitted to the data in each plot to approximate a liquid line of descent (figure 27). The equations of the best-fit curves were then used to calculate the major element composition of the hypothetical liquid at increments of 0.5 wt. % MgO. For each of the resulting 10 compositions, equilibrium phase compositions were calculated for olivine, clinopyroxene, orthopyroxene, and plagioclase. Ferromagnesian phase

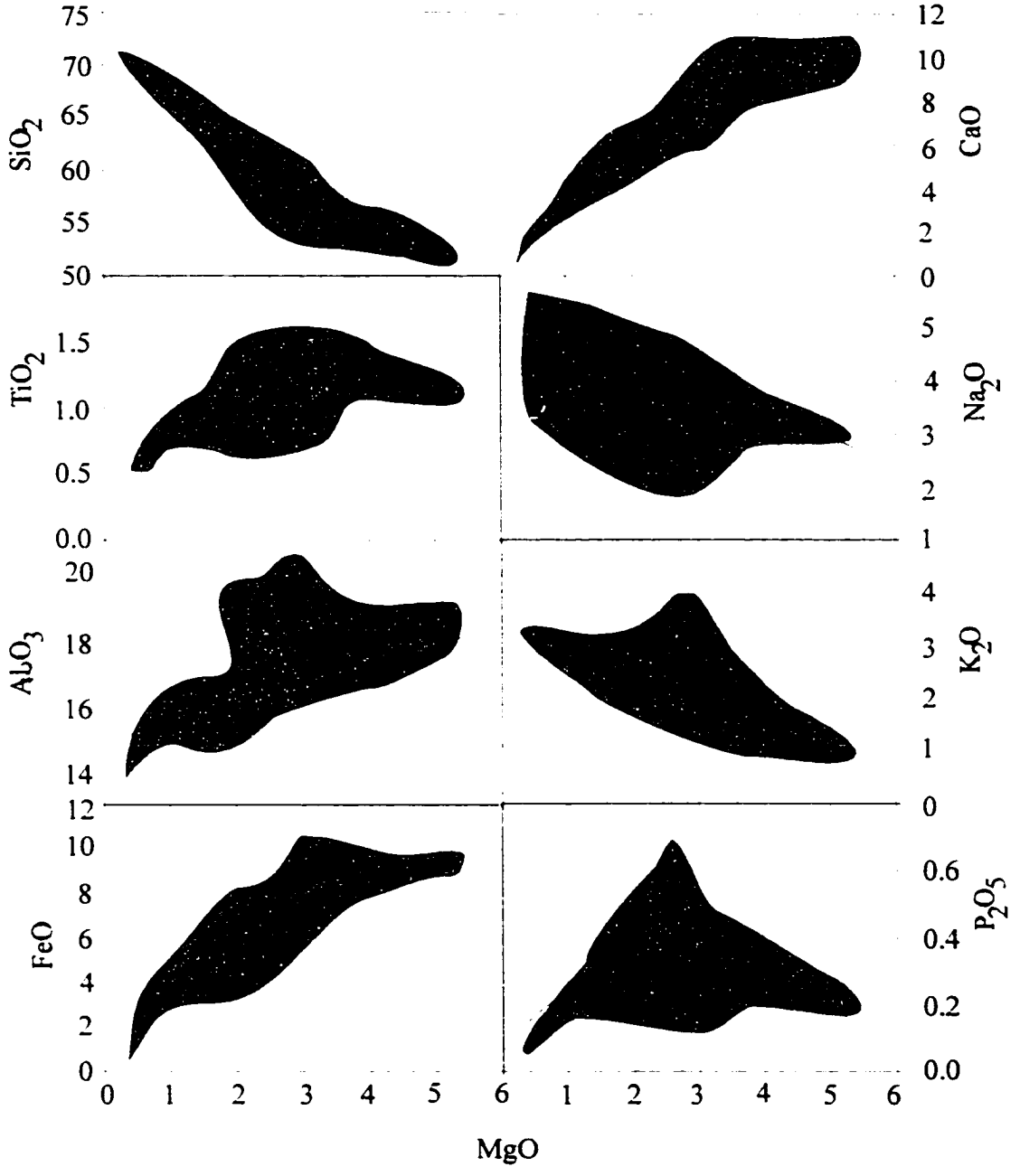

Figure 27: Regression curves through Aniakchak data set. The curves were used as model liquid compositions in assessing the ability of crystallization differentiation to produce the suite of samples from a common parent. All oxides are in weight percent. Grey fields represent unpublished data of C. R. Bacon, C. A. Neal, and C. J. Nye, and this study.

compositions were based on experimentally-determined equilibrium Kd values. For olivine, a value of 0.3 was used (Roeder and Emslie, 1970). Clinopyroxene composition was determined using a Kd value of 0.25 (Grove and Bryan, 1983) and othopyroxene with a value 0.29 (Grove et al., 1982). Equilibrium plagioclase compositions are less well constrained. Following the calculations of Nye (1987) plagioclase compositions were calculated by taking constant values for $(CaO/Na_2O)_{liq}/(CaO/Na_2O)_{plag}$ and finding the value that most closely replicated Ca, Al, and Na trends in the sample suite. Nye (1987) used values of 1, 2 and 3 to model the development of the Mt. Spurr magma system. For the case of Aniakchak, a value of 3 gave the best correspondence to plagioclase compositions observed in the HAB and rhyodacite end members. Compositions of each step in the liquid line of descent, and the equilibrium phenocryst compositions are given in table 8.

Based on an extensive data set for Mt. Spurr phenocrysts, Nye (1987) developed relationships between major element compositions and Mg numbers (molar $MgO/(MgO+FeO_t)$) for ferromagnesian phases and anorthite content for plagioclase. These phase compositions were then used in mass balance calculations (model 1: using plagioclase Kd of 3) for each of the ten steps in the hypothetical liquid line of descent. Results for each calculation were quite good, giving r^2 values of 0.1 or less in each case. The first step is achieved by removal of olivine, clinopyroxene, orthopyroxene, plagioclase, and magnetite. Including olivine in subsequent steps produced poor results, and was removed from the fractionating assemblage for the remainder of the model. All other phases remained. The proportions of the minerals change systematically throughout the model. Clinopyroxene decreases slightly from a solid weight fraction of 0.19 to 0.18. Orthopyroxene increases in the second step,

from 0.03 to 0.16, reflecting the discontinuance of olivine crystallization. Orthopyroxene then decreases in remaining steps by a factor of two, accounting for a solid weight fraction of 0.07 in the final step. Plagioclase increases over the entire course of the model, from a weight fraction of 0.56 to 0.64 in the final step. Finally, magnetite increases from a solid weight fraction of 0.07 in the first step to 0.11 in step 6, and then falls slightly to 0.10 in the final step. The liquid fraction declines from the initial value of 1 at the beginning, to 0.28 after the final step.

Table 8: Compositions of melts in fractional crystallization model. Compositions are derived from regression curves fitted to Aniakchak data set. See figure 27.

Step number	1	2	3	4	5	6	7	8	9	10
SiO2	52.09	53.13	54.41	55.95	57.73	59.76	61.99	64.44	67.19	70.18
TiO2	1.15	1.21	1.24	1.24	1.21	1.15	1.06	0.95	0.80	0.62
Al2O3	17.95	17.70	17.44	17.17	16.89	16.60	16.31	16.01	15.69	15.37
FeO	7.92	7.71	7.39	6.93	6.35	5.65	4.86	3.97	2.96	1.87
Fe2O3	1.78	1.81	1.82	1.79	1.73	1.63	1.49	1.29	1.03	0.70
MnO	0.18	0.19	0.19	0.19	0.19	0.19	0.18	0.17	0.16	0.14
MgO	5.00	4.50	4.01	3.51	3.00	2.50	2.00	1.51	1.00	0.50
CaO	9.83	9.21	8.53	7.78	6.96	6.08	5.15	4.16	3.09	1.96
Na2O	2.99	3.27	3.56	3.85	4.14	4.43	4.71	5.00	5.28	5.57
K2O	1.09	1.17	1.27	1.42	1.60	1.81	2.05	2.33	2.64	2.99
P2O5	0.20	0.27	0.32	0.36	0.37	0.37	0.34	0.30	0.24	0.17
Total	100.18	100.17	100.17	100.19	100.17	100.17	100.14	100.13	100.08	100.07
Olivine Mg #	77.31	75.83	74.39	72.95	71.43	69.94	68.25	66.36	63.43	57.61
Cpx Mg#	80.35	79.01	77.71	76.40	75.00	73.63	72.06	70.31	67.55	61.99
Opx Mg#	78.50	77.07	75.68	74.29	72.82	71.37	69.72	67.89	65.02	59.29
Plag An (Kd=3)	84.50	82.36	79.89	77.01	73.59	69.47	64.45	57.97	49.24	36.84
Plag An (Kd=1)	64.50	60.88	56.97	52.76	48.16	43.13	37.66	31.50	24.44	16.28

Two additional models, both with $(CaO/Na_2O)_{liq}/(CaO/Na_2O)_{plag}$ equal to 1, were also calculated. Results are given in table 9. The first of these (model 2) included olivine in the fractionating assemblage until the sixth step. After the sixth step, including olivine no longer produced successful results. From the beginning until the sixth step,

the olivine fraction decreased from 0.05 to 0.02. The solid fraction of plagioclase increases slightly over the course of the model from 0.60 to 0.66.

Table 9: Results of major element mass balance calculations. Liquid mass fraction refers to the entire system. Solid phase mass fractions refer to proportions of total solids.

Model 1

Step number	1	2	3	4	5	6	7	8	9	10
F	1.00	0.88	0.76	0.66	0.57	0.49	0.43	0.37	0.32	0.28
Mass Fraction										
Liquid	1.00	0.88	0.87	0.86	0.86	0.87	0.87	0.87	0.87	0.86
Ol	0.00	0.10	0.00	0.00	0.00	0.00	0.00	0.00	0.00	0.00
Cpx	0.00	0.23	0.19	0.19	0.19	0.19	0.18	0.18	0.18	0.18
Opx	0.00	0.03	0.16	0.15	0.14	0.14	0.12	0.11	0.10	0.07
Plag	0.00	0.56	0.56	0.56	0.56	0.59	0.58	0.60	0.63	0.64
Mt	0.00	0.07	0.08	0.09	0.09	0.10	0.11	0.11	0.10	0.10

Model 2

Step number	1	2	3	4	5	6	7	8	9	10
F	1.00	0.81	0.65	0.52	0.42	0.34	0.28	0.23	0.19	0.16
R^2		0.03	0.03	0.03	0.03	0.03	0.03	0.05	0.07	0.07
Mass Fraction										
Liquid	1.00	0.81	0.81	0.80	0.80	0.81	0.82	0.82	0.82	0.83
Ol	0.00	0.05	0.05	0.03	0.05	0.05	0.03	0.02	0.00	0.00
Cpx	0.00	0.22	0.22	0.22	0.22	0.22	0.23	0.23	0.23	0.23
Opx	0.00	0.06	0.05	0.05	0.03	0.01	0.01	0.01	0.02	0.01
Plag	0.00	0.60	0.61	0.62	0.62	0.63	0.64	0.65	0.65	0.66
Mt	0.00	0.07	0.08	0.08	0.08	0.08	0.09	0.09	0.09	0.09

Model 3

Step number	1	2	3	4	5	6	7	8	9	10
F	1.00	0.81	0.64	0.50	0.39	0.32	0.26	0.21	0.17	0.14
R^2		0.03	0.03	0.03	0.03	0.03	0.03	0.05	0.07	0.07
Mass Fraction										
Liquid	1.00	0.81	0.79	0.79	0.79	0.80	0.81	0.82	0.82	0.83
Ol	0.00	0.05	0.00	0.00	0.00	0.00	0.00	0.00	0.00	0.00
Cpx	0.00	0.22	0.20	0.20	0.20	0.21	0.21	0.22	0.23	0.23
Opx	0.00	0.06	0.11	0.10	0.09	0.08	0.06	0.04	0.02	0.01
Plag	0.00	0.60	0.60	0.61	0.62	0.63	0.64	0.65	0.65	0.66
Mt	0.00	0.07	0.08	0.08	0.09	0.09	0.09	0.09	0.09	0.09

Magnetite also increased slightly from 0.07 to 0.09. Clinopyroxene was roughly constant at 0.23. The orthopyroxene solid fraction decreased from 0.06 to 0.01. The other version of the model (model 3) included olivine, accounting for 5% of the

solids, only in the first step. Plagioclase increased from 0.60 to 0.66 from beginning to end. Clinopyroxene decreased from 0.22 to 0.20 after the exclusion of olivine, but then grew to 0.23 by the end. Orthopyroxene increased from 0.06 to 0.11 in the second step, then declined steadily to 0.01 by the last step. Both models produced good results, with r^2 values of 0.1 or less in all steps. Predicted phase assemblages for all three versions of the model are shown in table 9.

The phase assemblages produced by these models were used to predict changes in trace element concentrations. Partition coefficients used are shown in table 10. Figure 28 shows results of all three trace element models compared with Aniakchak data. Model 1 matches the data the best, but significantly underestimates LILE, and slightly overestimates REE and HFSE. In figure 29a, Rb vs. SiO2 data are well constrained between the model 1 and model 2. The trend defined by the Zr vs. SiO2 data, in figure 29b, however, lies at lower Zr concentration than all three models at any given SiO_2 concentration. Furthermore, figure 30 shows that the Aniakchak rocks all have smaller negative Eu anomalies and higher Sr concentrations than predicted by the crystal fractionation models. The model indicates a greater amount of plagioclase removal than the data allow.

Calculations of liquid lines of descent using the MELTS algorithm of Ghiorso and Sack (1995) also demonstrate the inconsistency of the Aniakchak data set with crystallization differentiation. These calculations are discussed in detail in chapter 2, and illustrated in figure 13. The possibility that the rhyodacite magmas were generated by some combination of crystallization and mixing with crustal melts is still tenable, however. Extrapolation of the model trends to higher silica values for several of the oxides considered suggests the plausibility of rhyodacite production by high

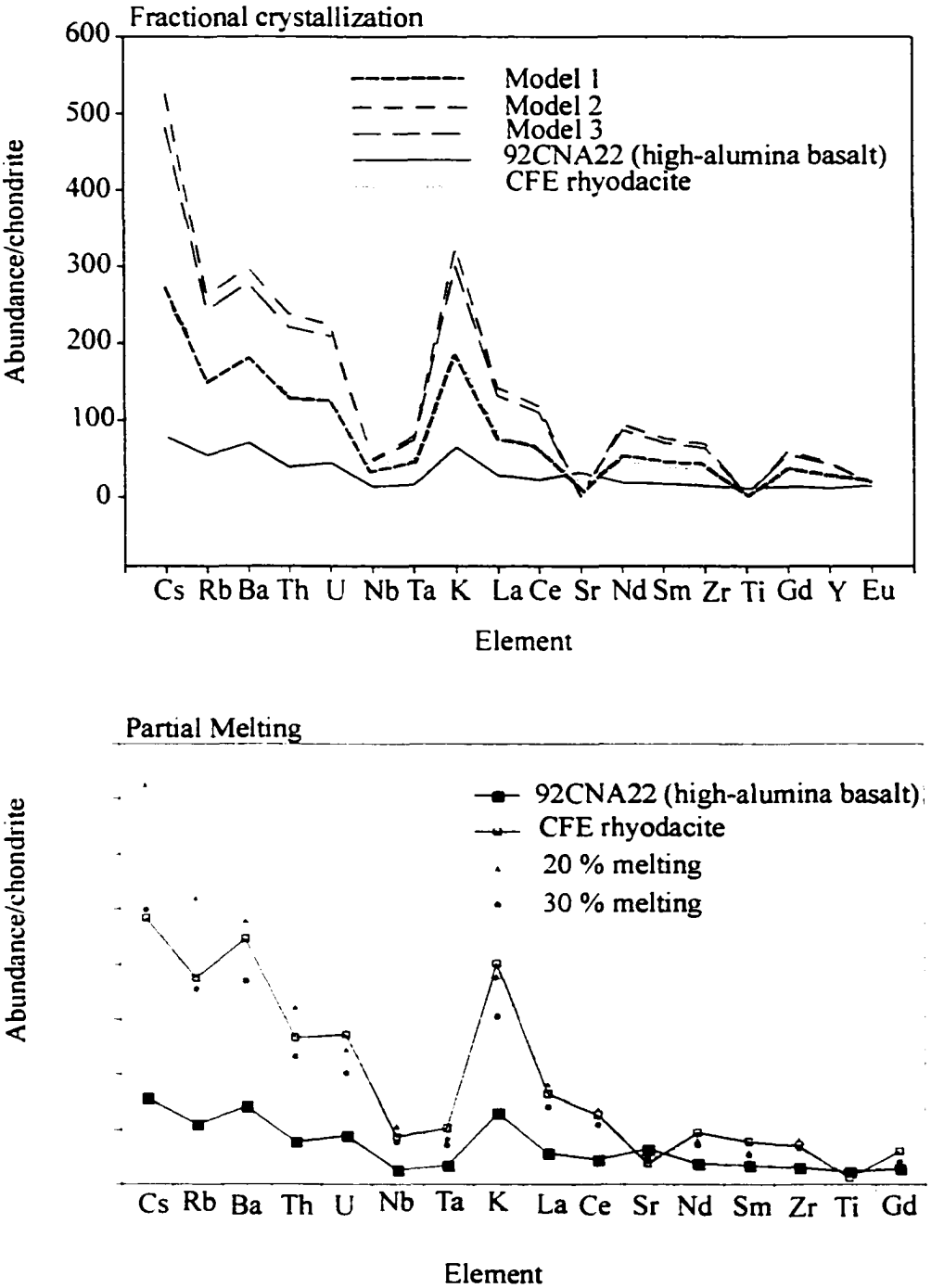

Figure 28: Trace element spider diagrams comparing CFE rhyodacite data with results from fractional crystallization (top) and partial melting (bottom).

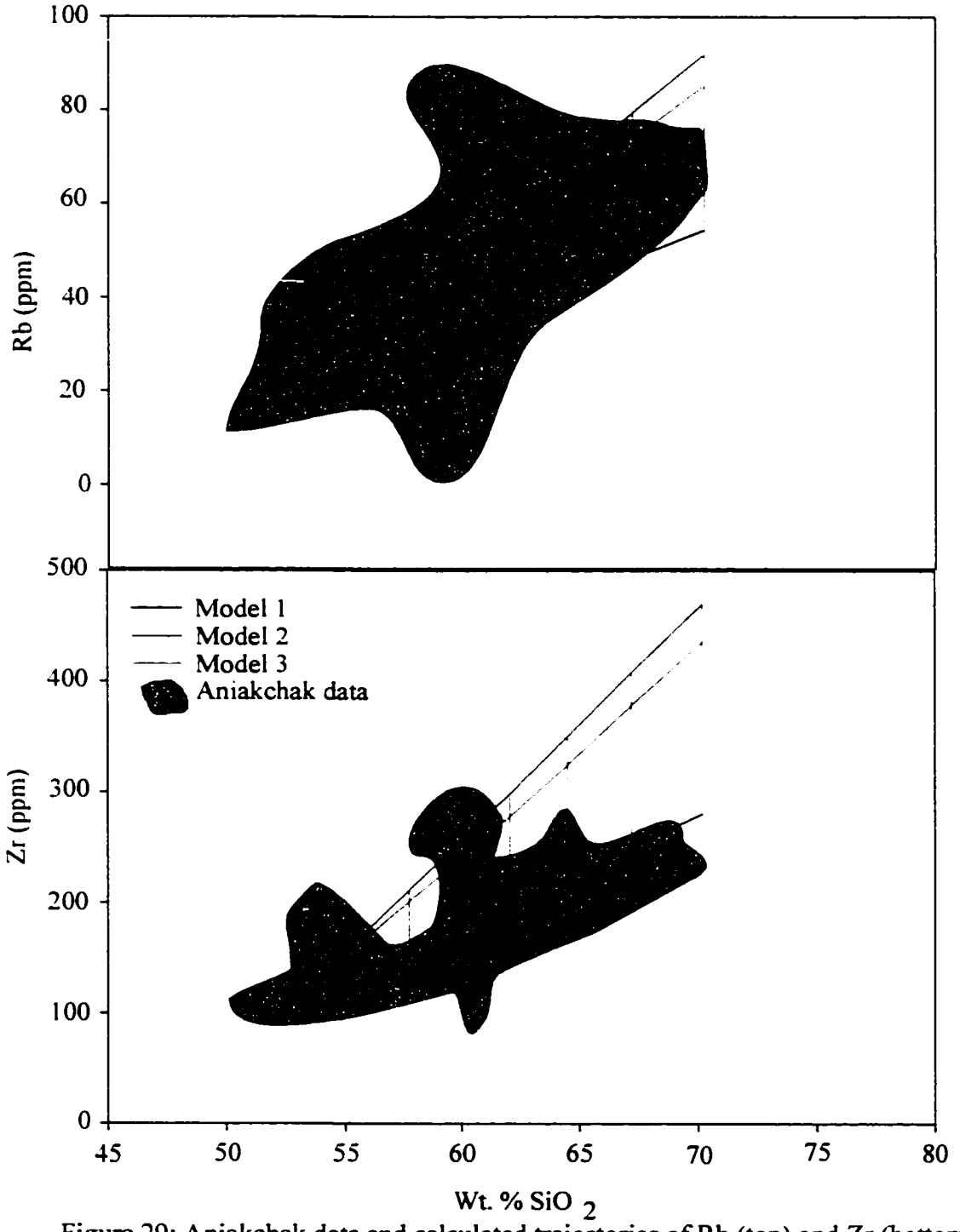

Figure 29: Aniakchak data and calculated trajectories of Rb (top) and Zr (bottom) versus silica for three fractional crystallization models. Vertical lines mark model step compositions.

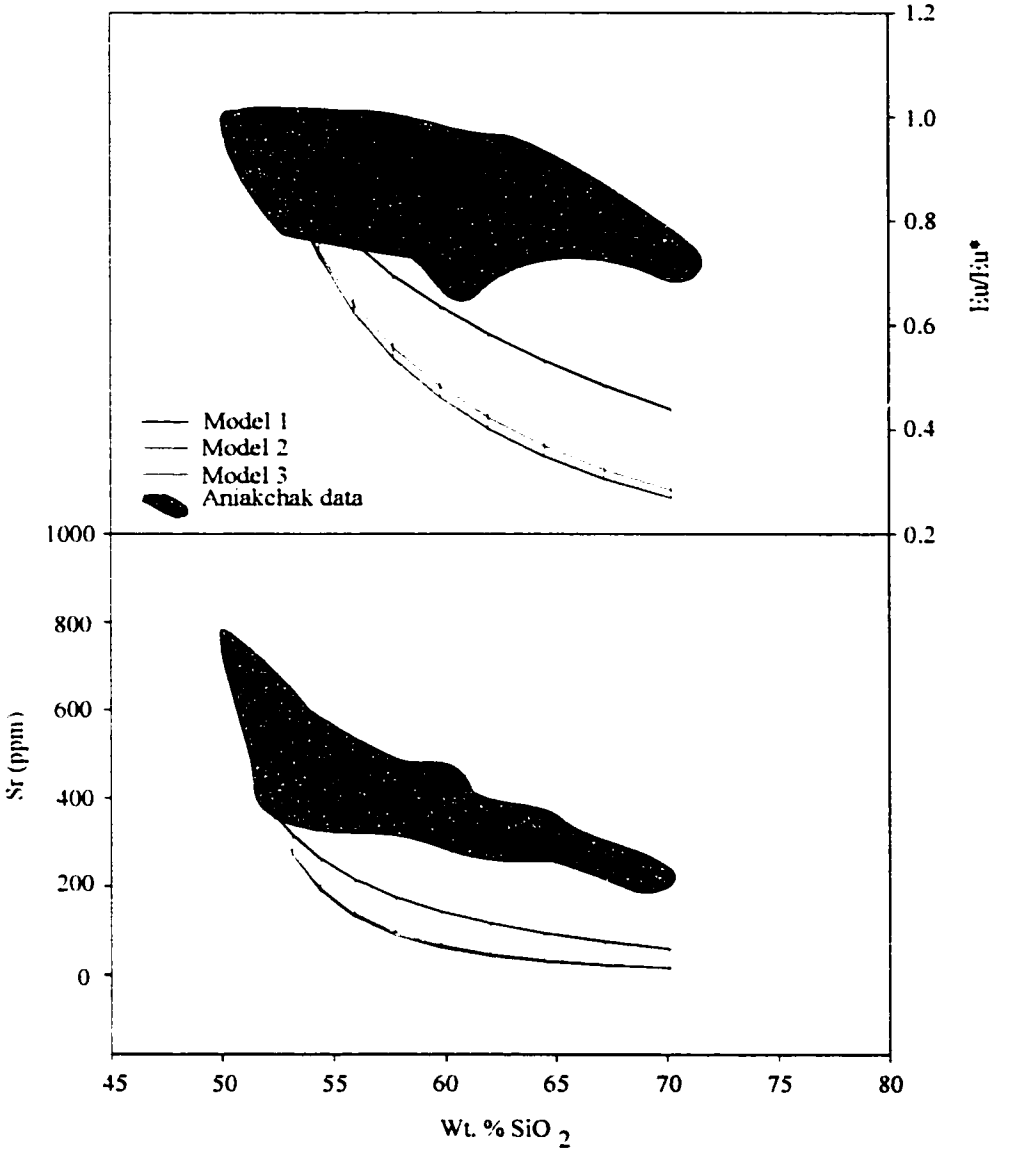

Figure 30: Comparison of europium anomalies (top) and strontium concentrations (bottom) versus silica predicted by fractional crystallization models (see text for details) and observed data. Both diagrams show that the models require a greater mass of plagioclase removal than the trace element data allow. Vertical lines mark model step compositions.

pressure crystallization (figure 13). In particular, the FeO, MgO, and CaO trends all point to the rhyodacite data. Al_2O_3 concentrations are between the extrapolated trends for high pressure equilibrium and fractional crystallization, while TiO_2 levels in the rhyodacites are higher than the predicted concentrations. Concentrations of Na_2O are higher than predicted by the models, and K_2O is significantly lower. It is possible that

Table 10: Partition coefficients used in fractionation and melting models. Sources of data: Arth (1976); Nash and Crecraft (1985); Pearce and Norry (1979); Bacon and Druitt (1988); Dostal et al. (1983); Sisson (1994); Mahood and Hildreth (1983); Ewart and Griffin (1994); Fujimaki et al. (1984); Green and Pearson (1987); Okamoto (1979); Nagasawa and Schnetzler (1971); Reid (1983); Philpotts and Schnetzler (1970); Kennedy et al. (1993); Villemant (1988).

Element	olivine	cpx	opx	plag	magnetite
Cs	0.01	0.01	0.01	0.03	0.01
Rb	0.0098	0.032	0.003	0.3	0.01
Ba	0.008	0.131	0.003	0.36	0.1
Th	0.006	0.15	0.13	0.048	0.01
U	0.007	0.21	0.145	0.093	0.7
Nb	0.01	0.3	0.35	0.3	0.7
Ta	0.098	0.263	0.165	0.035	1.2
K	0.0068	0.037	0.002	0.263	0.045
La	0.006	0.015	0.015	0.18	0.66
Ce	0.006	0.044	0.016	0.12	0.71
Sr	0.015	0.516	0.009	4	0.01
Nd	0.006	0.166	0.016	0.09	0.93
Sm	0.007	0.457	0.017	0.06	1.2
Zr	0.012	0.29	0.033	0.2	0.24
Ti	0.01	0.7	0.4	0.083	16.5
Gd	0.009	0.703	0.027	0.13	0.3
Y	0.013	0.84	0.44	0.13	0.12
Eu	0.007	0.5	0.05	1.13	1

appearance of potassium feldspar, occurring in later stages beyond the ability of MELTS to calculate, could change the slope of the SiO_2 – K_2O trend. This does nothing, however, to account for the Na_2O data, and is pure speculation.

The crystal-poor nature the rhyodacites and apparent equilibrium of crystals that are present indicate a relatively uncomplicated history for this magma since its separation from its source. Rhyodacitic melt inclusions in plagioclase and the lack of more mafic melt inclusions suggest that the plagioclase phenocrysts are not the product of protracted *in situ* equilibrium crystallization of a basaltic parent, although fractional crystallization is still a viable means of at least some silicic melt production. For example, Brophy and Dreher (2000) described a mechanism by which evolved but crystal poor magmas can be produced by extraction of interstitial melt from a crystallizing margin of a more mafic magma body.

In addition, melting of mafic plutons is also a reasonable means of CFE rhyodacite production. Although the pyroxenes in the rhyodacites have lower Kd values than expected for equilibrium, it should be noted that Beard and Lofgren (1991) observed similarly low Kd values in pyroxenes in equilibrium with melts produced in 7-kilobar amphibolite dehydration melting experiments. The low Kd values for orthopyroxene in CFE rhyodacite, does not necessarily preclude equilibrium between orthopyroxene and melt.

Further supporting the partial melting hypothesis are the trace element compositions of the pre-caldera lavas and tephras (figure 26). These rocks have generally lower SiO_2 contents, but comparable or higher incompatible element abundances. This is inconsistent with progressive crystallization differentiation, which

predicts higher incompatible elements with increasing differentiation. Successive melting of the same source would deplete the source in incompatible elements in early events, causing lower abundances of these elements in later events, regardless of the overall degree of melting.

Experimental studies have shown that partial melting of basaltic rocks is capable of producing typical arc rhyodacitic melts at mid- to lower-crustal pressures (Beard and Lofgren, 1989; 1991; Holloway and Burnham, 1972; Rushmer, 1991). Borg and Clynne (1998) and Tepper et al. (1993) point out that $P_{(H2O)}$ in the melting source region exerts an important control on the composition of resulting melts, because it is this parameter that determines whether a hydrous or anhydrous restite phase assemblage is stable in the presence of melt. These authors also contend that the amount of water present in the source region is largely controlled by the water contents of crystallizing basalts in the lower crust (Borg and Clynne, 1998; Tepper et al., 1993). Basalts from Shishaldin volcano on Unimak Island in the Aleutians have pre-eruptive water contents of less than 1.5 wt % (Stelling et al., in press). Brophy et al. (1999) have calculated water contents of 0.7 to 1.8 wt% for Kanaga high-alumina basalts and 2.0 to 3.2 wt. % for basalts from the Cold Bay volcanic complex. Baker and Eggler (1987) estimated water contents in Atka basalts to be around 2 wt. %. Although water content of Aleutian basalts can vary significantly, the predominantly anhydrous mineral assemblage present in all Aniakchak rhyodacites suggests a consistently water-undersaturated source region over the last few thousand years. In all water-undersaturated experiments performed by Beard and Lofgren (1991), amphibole had completely decomposed at 900 °C, a similar temperature to those determined from Fe-Ti oxide compositions in CFE rhyodacite.

Models of partial melting of mafic plutons reproduce the trace element composition of CFE rhyodacite fairly well, especially for the REE and HFSE. Around 20 % partial melting of a pluton with trace element compositions like that in basalt sample 92CNA22 produces trace element concentrations that are broadly similar to those observed in the CFE rhyodacites, especially in the REE and HFSE. The mineral assemblage used in the model is 51 % plagioclase, 39 % clinopyroxene, and 5 % each of magnetite and amphibole. This assemblage is broadly similar to that used in the melting experiments of Beard and Lofgren (1991), and to the predicted solid assemblage at the limit of the MELTS calculation for HAB. The MELTS results indicate the presence of up to 10% garnet, however, which will have a significant impact on the heavy REE and Y concentrations of the partial melts. Note that LILE abundances are below the 20% partial melting model values, but the crystallization calculations described earlier overestimate the LILE abundances in the CFE rhyodacites (figure 28). Both models match the REE and HFSE in the rhyodacite remarkably well.

Because the heat necessary for partial melting is supplied by release of latent heat during basalt crystallization (DePaolo, 1981; Spera and Bohrson, 2001), silicic melts derived from basalt crystallization may be in close proximity to those derived from partial melting. Mixing of the two silicic melts may explain the observed LILE concentrations in the CFE rhyodacites. Since both processes are predicted to generate similar REE and HFSE concentrations, mixing the two would have little effect on their respective abundances.

The similarities in whole rock and mineral compositions indicate that the late precaldera rhyodacites were formed by similar processes of combined crystallization

differentiation and partial melting at depths greater than that of the site of andesite hybridization. Any of the precaldera rhyodacitic magmas are plausible candidates for the silicic endmember for andesite formation. In all likelihood, several, or even all of them, contributed to the mass of CFE andesite. This process of silicic replenishment, along with basaltic inputs served to maintain the composition of the andesite.

4.6.2 Silicic Replenishment as a Triggering Mechanism

As discussed in chapter 2, the CFE andesite is thought to represent a cumulative mixture of successive inputs of basalt and rhyodacite into a shallow level magma chamber. The relatively simple, equilibrium mineral assemblage of the CFE rhyodacites, on the other hand, indicates an uncomplicated history between separation of the melt from the source and eruption. The caldera-forming eruption represents a replenishment event in which rhyodacitic magma intruded into the andesitic chamber. Alternatively, injection of basalt into a more silicic magma body could result in the production of a hybrid magma like the CFE andesite. The composition gap of 10 wt. % SiO_2 is left unexplained, however, by a mafic replenishment model. In any case, if the mixing event that produced the CFE andesite occurred nearly syneruptively, a gradational compositional zonation spanning some part of the compositional range between the resident and intruding magmas is expected. The hybrid nature of the CFE andesite and its compositional separation from the CFE rhyodacite indicates that the andesite had been formed prior to the introduction of the CFE rhyodacite. An independently mixed magma could have intruded a shallowly stored rhyodacite; however, the crystal poor nature and near liquidus temperatures of the CFE rhyodacite makes such a scenario unlikely. More probably, a batch of rhyodacite generated by

crystallazation of basalt and partial melting of gabbroic plutons ascended from depth greater than level of the andesite storage chamber and intruded into the andesite immediately prior to the eruption. This eruption then triggered the eruption.

The idea of silicic replenishment as an eruption triggering mechanism was put forth by Eichelberger et al. (2000). Eichelberger and Izbekov (2000) expounded on the differences between eruptions motivated by mafic intrusions and those provoked by silicic magma influxes. These authors argue that the lower density of the silicic magma causes the roof of the chamber to become unstable. The hybrid nature of the Aniakchak CFE andesite suggests that not all silicic replenishment events lead to eruption. Some silicic injections must be allowed to mix with the host magma in order to maintain the andesitic composition against basaltic influxes.

Seismicity preceding an eruption is often taken to reflect the fracturing of surrounding rocks to accommodate an increase in magma chamber pressure. Pressure increase in a chamber can be achieved through exsolution of a gas phase through second boiling (Tait et al., 1996), or through the addition of mass in a magmatic replenishment (e.g., Nakada et al., 1999). In either case, the pressure increase must be large enough and rapid enough to propagate a fracture to the surface. Crystallization of a magma body, and the resulting second boiling may be considered to occur on a timescale much longer than that of a single eruption. However, fracturing of surrounding rocks and viscoelastic relaxation of the chamber walls (Dragoni and Magnanensi, 1988) serve to increase the volume of the chamber, and thus alleviate at least some of the pressure increase derived from the exsolution of volatiles. Furthermore, not all magmatic replenishment events lead to eruption. Small-volume intrusions could be completely accomadated by fracturing of surrounding rocks. For

example, the 1996 seismic crisis at Akutan volcano in the Aleutian Islands is thought to be an example of a noneruptive intrusion (Keith et al., 1996). If the long-term rate of magmatic influx is greater than the rate of eruption, the result is a growing magma chamber. Pressure in the chamber is governed by the relationship (Druitt and Sparks, 1984):

$$\frac{\Delta V}{V} = \frac{\Delta P}{\beta}$$

where V is the initial volume, ΔV is the volume change, ΔP is the pressure change, and β is the bulk modulus of the melt. Assuming that the rate of magma production in the mantle or lower crust is independent of the volume of the shallow chamber, as the chamber grows, the pressure increase resulting from an influx of a given volume become less. To cause an eruption, an intrusion must elevate the pressure sufficiently to propagate a fracture to the surface. All else being equal, then, a larger chamber requires a larger influx of new magma to produce an eruption. Otherwise, the intruding magma pressurizes the chamber and expands the volume until the pressure is relieved. The host and injected magmas then have an opportunity to mix with one another.

The late precaldera rhyodacite lavas and the Black Nose pumice may represent "leaks" from the chamber following silicic inputs that were not quite large enough to erupt catastrophically. At least part of these magmas may have mixed with the host magma, leaving low-calcium plagioclase in the hybrid andesite as evidence. By this hypothesis, the CFE rhyodacite was sufficiently voluminous to initiate an immediate eruption, leaving little time to mix with the host.

4.7 Conclusion

While silicic magma genesis is an important issue from both a petrological and a volcanic hazards perspective, it is also one that is difficult to unravel. Crystallization of mafic magmas and anatexis of gabbroic plutons are expected to generate near eutectic melts. Major element compositions resulting from these two processes therefore converge to similar values, making process identification a complicated matter.

The simple mineralogy of the CFE and precaldera rhyodacites suggest an uncomplicated history between separation from the source and eruption, while variations in trace element abundances preclude progressive evolution of a single magma batch. The short time span over which these five silicic magmas erupted, less than 4500 years, indicates that they formed at least partially simultaneously from spatially separated sources. Chemical models of high-alumina basalt crystallization and mafic pluton partial melting are consistent with mixing of the two resulting magmas to produce the CFE rhyodacites. Because the compositions and mineralogies of the precaldera rhyodacites are similar to those of the CFE rhyodacite, it is reasonable that they too formed by some process of mixing between basalt distillates and gabbro partial melts. These evolved melts fit the expected composition of the silicic endmember involved in generating the CFE andesite. According to the hypothesis illustrated in figure 31, the CFE rhyodacite represents an unusually large pulse of silicic magma which rose to the top of the chamber, overstressed and destabilized the roof, leading to immediate eruption of both the rhyodacite and the resident andesite. Following the caldera-forming eruption, the magma chamber is reduced to a small system once again, where eruptions are more frequent, and hybrid magma compositions are closer to those expected from binary mixing.

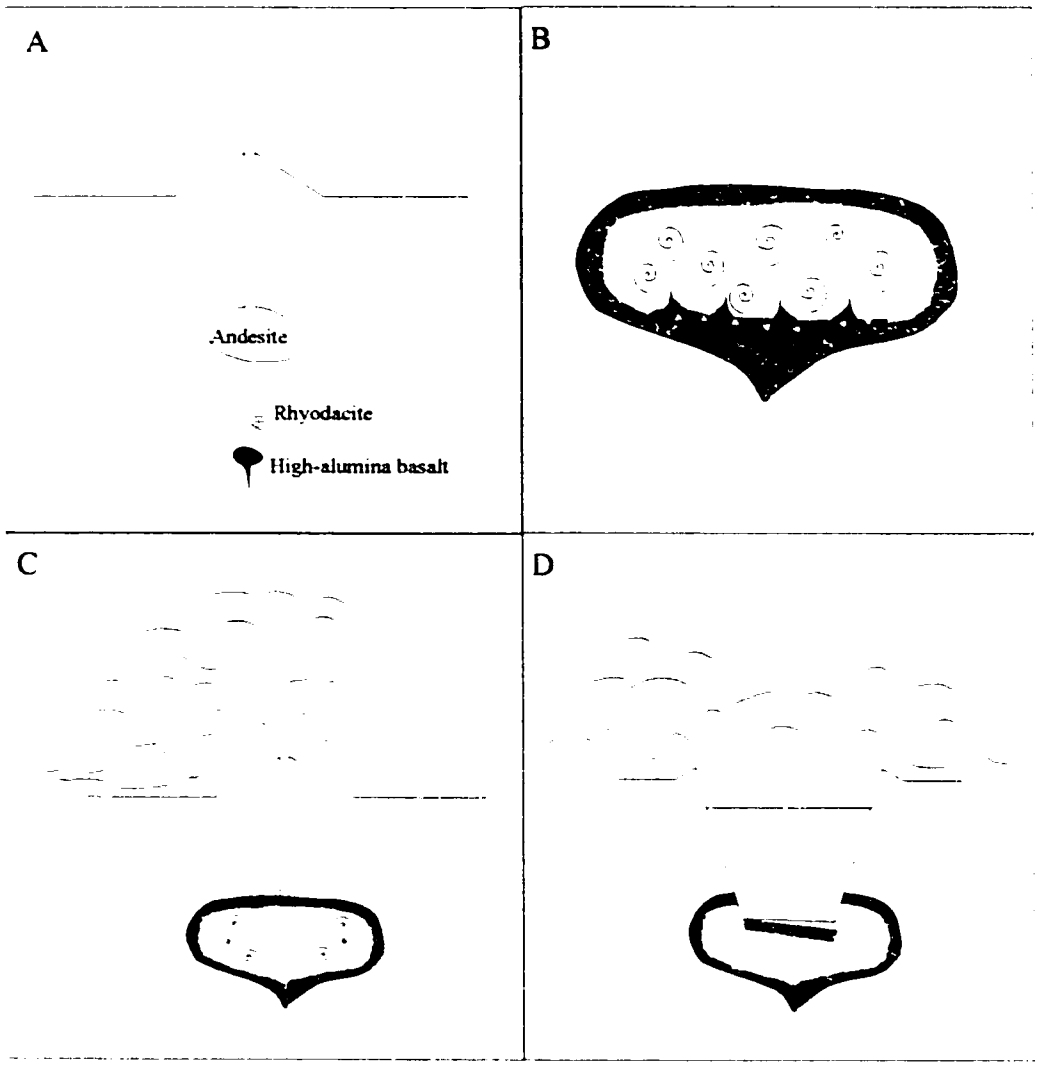

Figure 31: Summary of proposed chamber evolution and zoned ignimbrite formation. A) The andesitic chamber grows from successive inputs of basalt and rhyodacite. B) Volume of andesite grows over time, and crystallizes around the margins. Basalt intrusions cause expulsion of interstitial melt from the cumulates along the floor of the chamber. C) An unusually large batch of rhyodacite greatly overpressurizes the chamber and precipitates an eruption. D) After evacuation of most of the rhyodacite, the roof collapses into the chamber.

References Cited

Andersen, D.J. and Lindsley, D.H., 1988. Internally consistent solution models for Fe-Mg-Mn-Ti oxides; Fe-Ti oxides. American Mineralogist, August, 73(7-8): 714-726.

Arth, J.G., 1976. Behavior of trace elements during magmatic processes - A summary of theoretical models and their applications. Journal of Research, US Geological Survey 4: 41-47.

Aubin, W.L, Wolfe, J.A. and Conrey, R.M., 2000. Crustal melting beneath the Oregon Cascade range: the ignimbrite record. Eos, Transaction of the American Geophysical Union 81(48): 1381.

Bacon, C.R., 1983. Eruptive history of Mount Mazama and Crater Lake Caldera, Cascade Range, U.S.A. Journal of Volcanology and Geothermal Research, 18: 57-115.

Bacon, C.R., 2000. Preeruptive volatiles in the most recent eruptions of Aniakchak Volcano, Alaska. Eos, Transaction of the American Geophysical Union, 81(48): F1376-F1377.

Bacon, C.R., Bruggman, P.E., Christiansen, R.L., Clynne, M.A., Donelly-Nolan, J.M. and Hildreth, W., 1997a. Primitive magmas at five Cascade volcanic fields; melts from hot, heterogeneous sub-arc mantle. Canadian Mineralogist, April, 35(2): 397-423.

Bacon, C.R. and Druitt, T.H., 1988. Compositional evolution of the zoned calcalkaline magma chamber of Mount Mazama, Crater Lake, Oregon. Contributions to Mineralogy and Petrology, 98: 224-256.

Bacon, C.R. and Hirschmann, M.M., 1988. Mg/Mn partitioning as a test for

equilibrium between coexisting Fe-Ti oxides. American Mineralogist, 73: 57-61.

Bacon, C.R., Neal, C.A., Nye, C.J. and McGimsey, R.G., 1997b. Pre-eruptive temperatures for post-caldera magmas of Aniakchak Volcano, Alaska. Eos, Transaction of the American Geophysical Union, 78(46): F792-F793.

Baker, D.R. and Eggler, D.H., 1987. Compositions of anhydrous and hydrous melts coexisting with plagioclase, augite, and olivine or low-Ca pyroxene from 1 atm to 8 kbar; application to the Aleutian volcanic center of Atka. American Mineralogist, 72(1-2): 12-28.

Beard, J.S. and Lofgren, G.E., 1989. Effect of water on the composition of partial melts of greenstone and amphibolite. Science, 244(4901): 195-197.

Beard, J.S. and Lofgren, G.E., 1991. Dehydration melting and water-saturated melting of basaltic and andesitic greenstones and amphibolites at 1, 3 and 6.9 kb. Journal of Petrology, 32(2): 365-401.

Beget, J.E., Mason, O.K. and Anderson, P.M., 1992. Age, extent and climatic significance of the c. 3400 BP Aniakchak tephra, western Alaska, USA. The Holocene, 2(1): 51-56.

Bergantz, G.W., 1989. Underplating and partial melting: Implications for melt generation and extraction. Science, 245: 244-246.

Blake, S. and Ivey, G.N., 1986. Density and viscosity gradients in zoned magma chambers, and their influence on withdrawal dynamics. Journal of Volcanology and Geothermal Research, 30(3-4): 201-230.

Borg, L.E. and Clynne, M.A., 1998. The petrogenesis of felsic calc-alkaline magmas from the southernmost Cascades, California; origin by partial melting of

basaltic lower crust. Journal of Petrology, 39(6): 1197-1222.

Bottinga, Y., Weill, D. and Richet, P., 1982. Density calculations for silicate liquids; I, Revised method for aluminosilicate compositions. Geochimica et Cosmochimica Acta, 46(6): 909-919.

Brophy, J.G., 1987. The Cold Bay Volcanic Center, Aleutian Volcanic Arc; 2, Implications for fractionation and mixing mechanism in calc-alkaline andesite genesis. Contributions to Mineralogy and Petrology, 97(3): 378-388.

Brophy, J.G., 1990. Andesites from northeastern Kanaga Island, Aleutians; implications for calc-alkaline fractionation mechanisms and magma chamber development. Contributions to Mineralogy and Petrology, 104(5): 568-581.

Brophy, J.G. and Dreher, S.T., 2000. The origin of composition gaps at South Sister Volcano, central Oregon: implications for fractional crystallization processes beneath active calc-alkaline volcanoes. Journal of Volcanology and Geothermal Research, 102: 287-307.

Brophy, J.G., Whittington, C.S. and Park, Y.R., 1999. Sector-zoned augite megacrysts in Aleutian high alumina basalts; implications for the conditions of basalt crystallization and the generation of calc-alkaline series magmas. Contributions to Mineralogy and Petrology, 135(2-3): 277-290.

Class, C., Miller, D.M., Goldstein, S.L. and Langmuir, C.H., 2000. Distinguishing melt and fluid subduction components in Umnak Volcanics, Aleutian Arc. Geochemistry Geophysics Geosystems, 1.

Conrey, R.M., Donelly-Nolan, J.M., Taylor, E.M., Champion, D. and Bullen, T., 2001. The Shevlin Park Tuff, Central Oregon Cascade Range: Magmatic Processes Recorded in an Arc-Related Ash-Flow Tuff. Eos, Transaction of the

American Geophysical Union 82(47): Fall Meeting Supplement, Abstract V32D-0994.

DeBari, S.M., 1997. Evolution of magmas in continental and oceanic arcs: the role of the lower crust. The Canadian Mineralogist, 35(Part 2): 501-519.

DePaolo, D.J., 1981. Trace element and isotopic effects of combined wallrock assimilation and fractional crystallization. Earth and Planetary Science Letters, 53(2): 189-202.

Detterman, R.L., Miller, T.P., Yount, M.E. and Wilson, F.H., 1981. Geologic map of the Chignik and Sutwik Island quadrangles, Alaska, map I-1229. U.S. Geological Survey.

Devine, J.D., 1995. Petrogenesis of the basalt-andesite-dacite association of Grenada, Lesser Antilles island arc, revisited. Journal of Volcanology and Geothermal Research, 69(1-2): 1-33.

Dostal, J., Dupuy, C., Carron, J.P., le Guen de Kerneizan, M. and Maury, R.C., 1983. Partition coefficients of trace elements: application to volcanic rocks of St. Vincent, West Indies. Geochimica et Cosmochimica Acta 37: 525-533.

Dragoni, M. and Magnanensi, C., 1989. Displacement and stress produced by a pressurized, spherical magma chamber, surrounded by a viscoelastic shell. Physics of the Earth and Planetary Interiors, 56: 316-328.

Dreher, S.T., Faust, J.L., Miller, T.P. and Bacon, C.R., 1997. Chemical characteristics of the Aniakchak ash-flow sheet. Eos, Transaction of the American Geophysical Union, 78: F180.

Droop, G.T.R., 1987. A general equation for estimating Fe^{3-} concentrations in ferromagnesian silicates and oxides from microprobe analyses, using

stoichiometric criteria. Mineralogical Magazine, 51(361): 431-435.

Druitt, T.H., 1985. Vent evolution and lag breccia formation during the Cape Riva eruption of Santorini, Greece. Journal of Geology, 93(4): 439-454.

Druitt, T.H. and Bacon, C.R., 1986. Lithic breccia and ignimbrite erupted during the collapse of Crater Lake Caldera, Oregon. Journal of Volcanology and Geothermal Research, 29(1-4): 1-32.

Druitt, T.H. and Sparks, R.S.J., 1984. On the formation of calderas during ignimbrite eruptions. Nature, 310(5979): 679-681.

Eichelberger, J.C., Chertkoff, D.G., Dreher, S.T. and Nye, C.J., 2000. Magmas in collision: rethinking chemical zonation in silicic magmas. Geology, 28(7): 603-606.

Eichelberger, J.C. and Izbekov, P.E., 2000. Eruption of andesite triggered by dyke injection: contrasting cases at Karymsky Volcano, Kamchatka and Mt Katmai, Alaska. Philosophical Transactions of the Royal Society of London, 358(1770): 1465-1485.

Ewart, A. and Griffin, W.L., 1994. Application of proton-microprobe data to trace-element partitioning in volcanic rocks. Chemical Geology 117: 251-284.

Fierstein, J.E., Houghton, B.F., Wilson, C.J.N. and Hildreth, W.H., 1997. Complexities of plinian fall deposition at vent: an example from the 1912 Novarupta eruption (Alaska). Journal of Volcanology and Geothermal Research, 76(3-4): 215-227.

Fujimaki, H., Tatsumoto, M. and Aoki, K., 1984. Partition coefficients of Hf, Zr, and REE between phenocrysts and groundmasses. Journal of Geophysical Research, 89: 662-672.

George, R., Turner, S., Haweksworth, C., Nye, C.J., Bacon, C.R., Stelling, P.L. and Dreher, S.T., 2001. Chemical versus temporal controls on evolution of tholeiitic and calc-alkaline volcanoes in the Aleutian arc. Eos, Transaction of the American Geophysical Union, 82(47): Abstract No. T41C-0886.

Ghiroso, M.S. and Sack, R.O., 1995. Chemical and mass transfer in magmatic processes. IV. A revised and internally consistent thermodynamic model for the interpolation and extrapolation of liquid solid equilibria in magmatic systems at elevated temperatures and pressures. Contributions to Mineralogy and Petrology, 119: 197-212.

Green, T.H. and Pearson, N.J., 1987. An experimental study of Nb and Ta partitioning between Ti-rich minerals and silicate liquids at high pressure and temperature. Geochimica and Cosmochimica Acta 51: 55-62.

Green, T.H. and Watson, E.B., 1982. Crystallization of apatite in natural magmas under high pressure hydrous conditions, with particular reference to orogenic rock series. Contributions to Mineralogy and Petrology, 79(1): 96-105.

Grove, T.L. and Bryan, W.B., 1983. Fractionation of pyroxene-phyric MORB at low pressure: and experimental study. Contributions to Mineralogy and Petrology, 84: 293-309.

Grove, T.L., Gerlach, D. and Sando, T., 1982. Origin of calc-alkaline series lavas at Medicine Lake volcano by fractionation, assimilation, and mixing. Contributions to Mineralogy and Petrology, 80: 160-182.

Heiken, G. and Eichelberger, J.C., 1980. Eruptions at Chaos Crags, Lassen Volcanic National Park, California. Journal of Volcanology and Geothermal Research, 7: 443-481.

Hildreth, W., 1979. The Bishop Tuff; evidence for the origin of compositional zonation in silicic magma chambers. In: Chapin and E ; Elston (Editors), Ash-flow tuffs. Special Paper - Geological Society of America. Geological Society of America (GSA), Boulder, CO, United States, pp. 43-75.

Holloway, J.R. and Burnham, C.W., 1972. Melting Relations of Basalt with Equilibrium Water Pressure Less Than Total Pressure. Journal of Petrology, 13(1): 1-29.

Housh, T.B. and Luhr, J.F., 1991. Plagioclase-melt equilibria in hydrous systems. American Mineralogist, April, 76(3-4): 477-492.

Hubbard, B.R., 1931. A world inside a mountain: Aniakchak, the new volcanic wonderland of the Alaska Peninsula, is explored, National Geographic Magazine, pp. 319-345.

Huppert, H.E. and Turner, J.S., 1981. A laboratory model of a replenished magma chamber. Earth and Planetary Science Letters, 54(1): 144-152.

Keith, T.E.C., Nye, C.J., Eichelberger, J.C., Miller, T.P. and Power, J.A., 1996. March 1996 seismic crisis at Akutan Volcano, Central Aleutian Arc, Alaska. Eos, Transaction of the American Geophysical Union, 77(46): F815.

Kennedy, A.K., Lofgren, G.E. and Wasserburg, G.J., 1993. An experimental study of trace element partitioning between olivine, orthopyroxene and melt in chondrules: equilibrium balues and kinetic effects. Earth and Planetary Science Letters 115: 177-195.

Knesel, K.M. and Davidson, J.P., 1997. The origin and evolution of large-volume silicic magma systems: Long Valley Caldera. Geology International, 39(11): 1033-1052.

Lentz, D.R. and Gregoire, C., 1995. Petrology and mass-balance constraints on major-, trace-, and rare-earth-element mobility in porphyry-greisen alteration associated with the epizonal True Hill Granite, southwestern New Brunswick, Canada. Journal of Geochemical Exploration, 52(3): 303-331.

Mahood, G. and Hildreth, W., 1983. Large partition coefficients for trace elements in high-silica rhyolites. Geochemica et Cosmochimica Acta, 47(1):11-30.

Marsh, B.D., 1981. On the crystallinity, probability of occurrence, and rheology of lava and magma. Contributions to Mineralogy and Petrology, 78(1): 85-98.

Marsh, B.D., 1988. Crystal capture, sorting, and retention in convecting magma. Geological Society of America Bulletin, November, 100(11): 1720-1737.

Marsh, B.D., 1996. Solidification fronts and magmatic evolution. Mineralogical Magazine, 60(1(398)): 5-40.

McCulloch, M.T. and Gamble, A.J., 1991. Geochemical and geodynamical constraints on subduction zone magmatism. Earth and Planetary Science Letters, 102(3-4): 358-374.

McLean, H., 1979. Sandstone petrology: Upper Jurassic Naknek Formation on the Alaska Peninsula and coeval rocks on the Bering Shelf. Journal of Sedimentary Petrology, 49(4): 1263-1268.

Middleton, G.V. and Wilcock, P.R., 1994. Mechanics in the Earth and Environmental Sciences. Cambridge University Press, Cambridge, 459 pp.

Miller, T.P. and Smith, R.L., 1977. Spectacular mobility of ash flows around Aniakchak and Fisher calderas, Alaska. Geology, 5(3): 173-176.

Miller, T.P. and Smith, R.L., 1987. Late Quaternary caldera-forming eruptions in the eastern Aleutian Arc, Alaska. Geology, 15(5): 434-438.

Nagasawa, H. and Schnetzler, C.C., 1971. Partitioning of rare earth, alkali, and alkaline earth elements between phenocrysts and acidic igneous magmas. Geochimica et Cosmochimica Acta 35: 953-967.

Nakada, S., Shimizu, H. and Ohta, K., 1999. Overview of the 1990-1995 eruption at Unzen Volcano. Journal of Volcanology and Geothermal Research, 89(1-4): 1-22.

Nash, W.P. and Crecraft, H.R., 1985. Partition coefficients for trace elements in silicic magmas. Geochimica et Cosmochimica Acta 49: 2309-2322.

Nokleberg, W.J., Plafker, G. and Wilson, F.H., 1994. Geology of south-central Alaska. In: G. Plafker and H.C. Berg (Editors), The Geology of Alaska. The Geology of North America, pp. 311-366.

Nye, C.J., 1987. Stratigraphy, petrology, and geochemistry of the Spurr volcanic complex, eastern Aleutian Arc, Alaska, University of Alaska Fairbanks Geophysical Institute.

Nye, C.J., Neal, C.A. and McGimsey, R.G., 1993. Extreme and abrupt transition from tholeiitic to calcalkaline volcanism at Aniakchak Volcano, eastern Aleutian Arc. In: Anonymous (Editor), AGU 1993 fall meeting. Eos, Transactions, American Geophysical Union. American Geophysical Union, Washington, DC, United States, pp. 674.

O'Hara, M.J., 1977. Geochemical evolution during fractional crystallisation of a periodically refilled magma chamber. Nature, 266(5602): 503-507.

O'Hara, M.J. and Matthews, R.E., 1981. Geochemical evolution in an advancing, periodically replenished, periodically tapped, continuously fractionated magma chamber. Journal of the Geological Society of London, 138(2): 237-

277.

Okamoto, K., 1979. Geochemical study on magmatic differentiation of Asama volcano, Central Japan. Journal of the Geological Society Japan 85: 525-535.

Pearce, J.A. and Norry, M.J., 1979. Petrogenetic implications of Ti, Zr, Y, and Nb variations in volcanic rocks. Contributions to Mineralogy and Petrology, 69(1):33-47.

Philpotts, J.A. and Schnetzler, C.C., 1970. Phenocryst-marix partition coefficients for K, Rb, Sr, and Ba, with applications to anorthosite and basalt genesis. Geochimica et Cosmochimica Acta 34: 307-322.

Poitrasson, F., Pin, C. and Duthou, J.-L., 1995. Hydrothermal remobilization of rare earth elements and its effect on Nd isotopes in rhyolite and granite. Earth and Planetary Science Letters, 130: 1-11.

Reed, B.L. and Lanphere, M.A., 1970. Plutonic belts of central and southern Alaska range and Alaska peninsula. The American Association of Petroleum Geologists Bulletin, 54(12): 2502.

Reed, B.L. and Lanphere, M.A., 1973. Alaska-Aleutian Range Batholith; Geochronology, Chemistry, and Relation to Circum-Pacific Plutonism. Geological Society of America Bulletin, 84(8): 2583-2609.

Reid, F., 1983. Origin of the rhyolitic rocks of the Taupo Volcanic Zone, New Zealand. Geothermal Research 15: 315-333.

Roeder, P.L. and Emslie, R.F., 1970. Olivine-liquid equilibrium. Contributions to Mineralogy and Petrology, 29(4): 275-289.

Rose, W.I. and Chesner, C.A., 1987. Dispersal of ash in the great Toba eruption, 75 ka. Geology, 15(10): 913-917.

Rushmer, T., 1991. Partial melting of two amphibolites; contrasting experimental results under fluid-absent conditions. Contributions to Mineralogy and Petrology, 107(1): 41-59.

Ryan, M.P., 1993. Neutral buoyancy and the structure of mid-ocean ridge magma reservoirs. Journal of Geophysical Research, 98(12): 22,321-22,338.

Sack, R.O., Carmichael, I.S.E., Rivers, M. and Ghiroso, M.S., 1980. Ferric-ferrous equilibria in natural silicate liquids at 1 bar. Contributions to Mineralogy and Petrology, 79: 169-186.

Sakuyama, M., 1981. Petrological study of the Myoko and Kurohime volcanoes, Japan; crystallization sequence and evidence for magma mixing. Journal of Petrology, 22(4): 553-583.

Schmitt, A.K., de Silva, S.L., Trumbull, R.B. and Emmermann, R., 2001. Magma evolution in the Purico ignimbrite complex, northern Chile: evidence for zoning of a dacitic magma by injection of rhyolitic melts following mafic recharge. Contributions to Mineralogy and Petrology, 140: 680-700.

Sigurdsson, H. and Carey, S., 1989. Plinian and co-ignimbrite tephra fall from the 1815 eruption of Tambora Volcano. Bulletin of Volcanology, 51(4): 243-270.

Sisson, T.W., 1994. Hornblende-melt trace-element partitioning measured by ion microprobe. Chemical Geology 117: 331-344.

Smith, W., 1925. Aniakchak Crater, Alaska Peninsula. United States Geological Survey Professional Paper, 132-J: 139-145.

Snyder, D. and Tait, S., 1996. Magma mixing by convective entrainment. Nature, 379(6565): 529-531.

Snyder, D. and Tait, S., 1998. The imprint of basalt on the geochemistry of silicic

magmas. Earth and Planetary Science Letters, 160(3-4): 433-445.

Sparks, R.S.J., Huppert, H.E. and Turner, J.S., 1984. The fluid dynamics of evolving magma chambers. Philosophical Transactions of the Royal Society of London, Series A, 310(1514): 511-534.

Sparks, R.S.J. and Walker, G.P.L., 1977. The significance of vitric-enriched air-fall ashes associated with crystal-enriched ignimbrites. Journal of Volcanology and Geothermal Research, 2(4): 329-341.

Spera, F.J., 1984. Some numerical experiments on the withdrawal of magma from crustal reservoirs. Journal of Geophysical Research, 89(10): 8222-8236.

Spera, F.J. and Bohrson, W.A., 2001. Energy-constrained open-system magmatic processes: I. General model and energy-constrained assimilation and fractional crystallization (EC-AFC) formulation. Journal of Petrology, 42(5): 999-1018.

Stelling, P. et al., submitted. Geology and petrology of ejecta from the 1999 eruption of Shishaldin Volcano, Alaska. Bulletin of Volcanology.

Stormer, J.C., Jr., 1983. The effects of recalculation on estimates of temperature and oxygen fugacity from analyses of multicomponent iron-titanium oxides. American Mineralogist, 68(5-6): 586-594.

Tait, S., Jaupart, C. and Vergniolle, S., 1989. Pressure, gas content and eruption periodicity of a shallow, crystallizing magma chamber. Earth and Planetary Science Letters, 92: 107-123.

Tatsumi, Y., Hamilton, D.L. and Nesbitt, R.W., 1986. Chemical characteristics of fluid phase released from a subducted lithosphere and origin of arc magmas; evidence from high-pressure experiments and natural rocks. Journal of Volcanology and Geothermal Research, 29(1-4): 293-309.

Tepper, J.H., Nelson, B.K., Bergantz, G.W. and Irving, A.J., 1993. Petrology of the Chilliwack Batholith, North Cascades, Washington; generation of calc-alkaline granitoids by melting mafic lower crust with variable water fugacity. Contributions to Mineralogy and Petrology, 113(3): 333-351.

Turcotte, D.L. and Schubert, G., 1982. Geodynamics: Applications of Continuum Physics to Geological Problems. John Wiley and Sons, Inc., New York, 450 pp.

Turner, S., Evans, P. and Hawkesworth, C., 2001. Ultrafast source-to-surface movement of melt at island arcs from (super 226) Ra- (super 230) Th systematics. Science, 292(5520): 1363-1366.

van der Weijden, C.H. and van der Weijden, R.D., 1995. Mobility of major, minor and some redox-sensitive trace elements and rare-earth elements during weathering of four granitoids in central Portugal. Chemical Geology, 125(3-4): 149-167.

Villemant, B., 1988. Trace element evolution in the Plegrean Fields, Central Italy.: fractional crystallization and selective enrichment. Contributions to Mineralogical Petrology 98: 169-183.

Walker, D., Shibata, T. and DeLong, S.E., 1979. Abyssal tholeiites from the Oceanographer fracture zone; II. Phase equilibria and mixing. Contributions to Mineralogy and Petrology, September, 70(2): 111-125.

Wiebe, R.A., 1996. Mafic-silicic layered intrusions; the role of basaltic injections on magmatic processes and the evolution of silicic magma chambers, Special Paper Geological Society of America, pp. 233-242.

Wilson, F.H., 1985. Meshik and Aleutian arcs; Tertiary volcanism on Alaska

Peninsula, Alaska. American Association of Petroleum Geologists Bulletin, 69(4): 683.

Wood, B.J. and Banno, S., 1973. Garnet-Orthopyroxene and Orthopyroxene-Clinopyroxene Relationships in Simple and Complex Systems. Contributions to Mineralogy and Petrology, 42(2): 109-124.

Woods, A.W. and Wohletz, K.H., 1991. Dimensions and dynamics of co-ignimbrite eruption columns. Nature, 350(6315): 225-227.

You, C.-F., Castillo, PR, Gieskes, JM, Chan, LH, Spivack, AJ, 1996. Trace element behavior in hydrothermal experiments: Implications for fluid processes at shallow depths in subduction zones. Earth and Planetary Science Letters, 140: 41-52.

Zhou, X.M. and Li, W.X., 2000. Origin of late Mesozoic igneous rocks in southeastern China: implications for lithosphere subduction and underplating of mafic magmas. Tectonophysics, 326(3-4): 269-287.

Appendix A: Whole rock Compositions

Major elements were determined by X-Ray fluorescence (XRF) and trace elements by inductively couple plasma – mass spectrometry (ICP-MS) at Washington State University. Section designations correspond to mapped locations in figure 2. Latitude and longitude for each section can be found in table 2 and appendix E.

Section	AC-5AD	AC-5BD	AC-5CD	AC-5DD	AC-91	AC-101	AC11a1
SiO2	67.92	68.88	59.13	59.56	69.15	60.17	60.83
TiO2	0.51	0.56	1.42	1.43	0.71	1.31	1.24
Al2O3	14.66	15.12	16.31	16.41	14.86	15.86	15.64
FeO	2.15	2.42	5.85	5.81	2.87	6.29	6.00
Fe2O3	0.55	0.62	1.20	1.20	0.74	1.30	1.28
MnO	0.15	0.15	0.21	0.21	0.16	0.19	0.19
MgO	0.52	0.68	2.67	2.63	0.67	2.42	1.78
CaO	1.87	2.14	5.70	5.72	2.22	5.36	4.73
Na2O	5.01	5.32	4.72	4.81	5.32	4.18	4.18
K2O	2.89	2.93	1.64	1.62	3.03	2.26	2.48
P2O5	0.11	0.13	0.67	0.67	0.16	0.39	0.40
Total	96.34	98.95	99.51	100.06	99.89	99.73	98.75
FeO/MgO	2.59	2.23	1.34	1.35	2.68	1.59	2.07
Mg#	0.30	0.33	0.45	0.45	0.29	0.41	0.35
La ppm	27.62	27.00	19.88	20.25	27.08	23.75	27.43
Ce ppm	55.13	54.62	41.43	42.01	55.48	49.54	56.56
Pr ppm	6.88	6.90	5.49	5.59	7.01	6.47	7.34
Nd ppm	29.90	29.84	25.41	25.86	30.96	29.40	32.15
Sm ppm	7.88	7.75	6.97	7.05	8.15	8.03	8.81
Eu ppm	2.03	2.09	2.19	2.21	2.09	2.16	2.22
Gd ppm	7.68	7.82	7.08	7.11	8.24	8.31	9.10
Tb ppm	1.34	1.34	1.14	1.16	1.41	1.36	1.53
Dy ppm	8.43	8.40	6.90	7.11	8.87	8.31	9.22
Ho ppm	1.81	1.75	1.42	1.43	1.84	1.70	1.90
Er ppm	5.01	4.97	3.81	3.83	5.16	4.72	5.28
Tm ppm	0.74	0.75	0.55	0.54	0.79	0.68	0.76
Yb ppm	4.79	4.79	3.29	3.35	4.97	4.23	4.83
Lu ppm	0.76	0.78	0.54	0.53	0.80	0.68	0.74
Ba ppm	861	843	533	545	863	659	778
Th ppm	5.42	5.52	3.00	2.95	5.58	4.54	6.26
Nb ppm	15.59	15.29	9.50	9.61	16.04	13.18	15.89
Y ppm	48.96	49.38	38.41	38.27	51.48	45.53	52.87
Hf ppm	6.89	7.10	3.94	3.87	7.31	5.73	6.58
Ta ppm	1.00	1.04	0.66	0.66	1.12	0.94	1.04
Zr ppm	241	240	148	147	255	206	230
U ppm	2.63	2.68	1.48	1.42	2.73	2.16	2.60
Pb ppm	10.37	10.32	6.46	6.70	11.08	8.60	9.80
Rb ppm	67.7	66.3	35.4	35.3	70.5	53.0	65.1
Cs ppm	2.98	2.99	1.58	1.56	3.21	2.55	3.03
Sr ppm	222	226	457	475	222	319	304
Sc ppm	12.6	13.0	23.9	24.4	15.4	24.6	24.8

	AC11c	AC11f	AC-12	AC-14	AC-15	AC-18	AC-19
Section	**1**	**1**	**1**	**1**	**1**	**1**	**1**
SiO2	59.02	65.44	64.58	68.48	59.73	68.27	67.21
TiO2	1.30	0.98	1.08	0.73	1.34	0.71	0.85
Al2O3	15.38	15.04	15.88	14.87	15.76	14.80	15.37
FeO	6.51	3.64	4.05	3.26	6.66	3.15	3.46
Fe2O3	1.36	0.88	0.94	0.49	1.36	0.48	0.68
MnO	0.19	0.17	0.20	0.16	0.20	0.16	0.17
MgO	2.11	1.02	1.54	0.74	2.47	0.69	1.01
CaO	5.25	3.16	3.89	2.30	5.53	2.23	2.87
Na2O	4.10	4.75	4.97	5.20	4.21	5.16	5.24
K2O	2.24	2.79	2.45	2.98	2.13	3.03	2.73
P2O5	0.39	0.28	0.38	0.16	0.38	0.16	0.22
Total	97.84	98.14	99.95	99.38	99.76	98.84	99.81
FeO/MgO	1.89	2.22	1.63	2.64	1.65	2.74	2.09
Mg#	0.37	0.33	0.40	0.29	0.40	0.28	0.34
La ppm	23.82	28.31	25.23	28.03	22.96	28.42	26.67
Ce ppm	48.33	57.39	52.36	56.08	47.52	57.18	54.28
Pr ppm	6.29	7.33	6.75	7.03	6.15	7.16	6.93
Nd ppm	27.87	32.10	30.52	31.36	27.94	31.54	30.91
Sm ppm	7.89	8.64	8.36	8.29	7.56	8.63	8.25
Eu ppm	2.09	2.16	2.19	2.06	2.06	2.11	2.19
Gd ppm	7.99	8.77	8.36	8.48	7.86	8.51	8.38
Tb ppm	1.33	1.50	1.36	1.40	1.29	1.43	1.42
Dy ppm	8.17	9.26	8.52	8.87	7.94	9.06	8.79
Ho ppm	1.69	1.90	1.76	1.84	1.64	1.89	1.81
Er ppm	4.73	5.37	4.79	5.19	4.45	5.21	5.11
Tm ppm	0.67	0.78	0.72	0.79	0.66	0.80	0.76
Yb ppm	4.22	4.98	4.38	4.95	4.09	5.00	4.79
Lu ppm	0.67	0.78	0.71	0.81	0.66	0.82	0.78
Ba ppm	689	846	728	855	643	862	807
Th ppm	5.41	6.43	4.75	5.69	4.39	5.77	5.41
Nb ppm	13.97	16.62	13.90	16.03	12.90	16.15	15.29
Y ppm	46.69	52.80	47.02	50.65	44.05	51.61	50.12
Hf ppm	5.97	7.01	5.99	7.37	5.66	7.44	6.84
Ta ppm	0.93	1.09	0.95	1.11	0.90	1.12	1.06
Zr ppm	208	244	214	252	198	255	234
U ppm	2.19	2.67	2.32	2.75	2.11	2.76	2.61
Pb ppm	8.29	10.63	9.27	11.13	7.99	11.27	9.84
Rb ppm	56.2	69.0	56.4	69.6	52.0	70.0	62.5
Cs ppm	2.59	3.29	2.68	3.26	2.43	3.30	3.00
Sr ppm	317	252	301	207	329	214	260
Sc ppm	26.8	18.9	19.0	14.8	25.6	15.0	16.6

	AC-20	AC-21	AC-22	AC-37A	AC-37B	AC-37C	AC-37D
Section	**1**	**1**	**F**	**2**	**2**	**2**	**2**
SiO2	66.40	67.31	67.55	69.19	69.14	69.11	59.59
TiO2	0.87	0.85	0.83	0.52	0.55	0.53	1.39
Al2O3	15.15	15.24	15.53	15.01	15.18	15.04	16.15
FeO	3.66	3.33	3.50	2.10	2.21	2.09	5.56
Fe2O3	0.71	0.66	0.28	0.54	0.57	0.54	1.16
MnO	0.17	0.17	0.15	0.16	0.15	0.15	0.21
MgO	1.01	1.07	1.10	0.60	0.71	0.70	2.54
CaO	2.91	2.84	2.85	1.97	2.09	1.95	5.49
Na2O	5.10	5.22	5.10	5.27	5.61	5.40	4.76
K2O	2.72	2.75	2.98	2.91	2.88	2.91	1.69
P2O5	0.23	0.22	0.21	0.11	0.12	0.11	0.63
Total	98.94	99.66	100.08	98.38	99.21	98.53	99.17
FeO/MgO	2.21	1.90	1.85	2.19	1.95	1.87	1.34
Mg#	0.33	0.36	0.36	0.34	0.36	0.37	0.45
La ppm	26.15	26.67	27.74	27.32	26.58	26.75	20.71
Ce ppm	53.75	54.04	55.38	54.72	53.57	54.04	43.19
Pr ppm	6.75	6.89	7.07	6.81	6.71	6.81	5.76
Nd ppm	29.44	30.91	31.54	30.07	29.93	29.89	26.92
Sm ppm	8.01	8.30	8.35	7.90	7.90	7.87	7.25
Eu ppm	2.11	2.19	2.08	1.89	2.07	2.03	2.28
Gd ppm	8.17	8.47	8.37	8.04	7.90	8.02	7.53
Tb ppm	1.35	1.40	1.39	1.35	1.34	1.34	1.19
Dy ppm	8.49	8.70	8.79	8.32	8.15	8.34	7.19
Ho ppm	1.76	1.82	1.83	1.73	1.72	1.74	1.46
Er ppm	4.80	5.08	5.16	4.92	4.85	4.86	3.88
Tm ppm	0.73	0.77	0.76	0.75	0.72	0.75	0.58
Yb ppm	4.58	4.74	4.90	4.70	4.65	4.73	3.46
Lu ppm	0.74	0.77	0.80	0.77	0.76	0.78	0.57
Ba ppm	782	806	837	860	826	835	554
Th ppm	4.96	5.17	5.97	5.54	5.37	5.61	3.26
Nb ppm	14.87	15.34	16.86	15.17	14.82	15.19	9.84
Y ppm	48.66	50.97	50.53	50.04	48.25	49.05	40.29
Hf ppm	6.38	6.81	7.43	6.99	6.83	6.89	4.12
Ta ppm	1.01	1.04	1.16	1.02	1.00	1.07	0.68
Zr ppm	233	233	256	241	236	240	152
U ppm	2.43	2.50	2.93	2.63	2.57	2.74	1.55
Pb ppm	8.40	10.50	10.85	11.17	10.62	11.29	6.87
Rb ppm	62.2	64.9	71.8	65.5	64.3	66.7	37.1
Cs ppm	2.91	3.00	3.41	3.05	2.91	2.98	1.67
Sr ppm	259	259	231	213	228	219	470
Sc ppm	16.6	17.0	15.5	12.5	12.8	12.6	24.1

	ACAF1A1	ACAF1A2	ACAF1A3	ACAF1A4	ACAF1A5	ACAF1A6
Section	**8**	**8**	**8**	**8**	**8**	**8**
SiO2	69.27	69.91	68.69	58.97	59.76	68.13
TiO2	0.54	0.52	0.60	1.30	1.31	0.63
Al2O3	15.16	15.14	15.23	16.27	16.23	15.26
FeO	2.10	2.11	2.47	5.85	6.05	2.59
Fe2O3	0.54	0.55	0.63	1.19	1.24	0.66
MnO	0.15	0.15	0.15	0.20	0.20	0.15
MgO	0.68	0.63	0.67	2.67	2.64	0.77
CaO	2.02	1.96	2.28	5.95	5.82	2.41
Na2O	5.49	5.55	5.39	4.52	4.58	5.42
K2O	2.93	2.95	2.82	1.63	1.65	2.79
P2O5	0.12	0.11	0.15	0.55	0.58	0.17
Total	99.00	99.57	99.08	99.10	100.06	98.98
FeO/MgO	1.93	2.09	2.31	1.34	1.40	2.10
Mg#	0.37	0.35	0.33	0.45	0.44	0.35
La ppm	26.40	26.76	26.32	19.89	19.65	26.67
Ce ppm	54.15	54.56	52.95	41.09	40.60	53.48
Pr ppm	6.73	6.93	6.71	5.35	5.38	6.70
Nd ppm	29.43	30.25	29.55	24.55	25.18	29.36
Sm ppm	7.83	7.87	7.74	6.72	6.82	7.72
Eu ppm	2.06	2.08	2.07	2.09	2.13	2.11
Gd ppm	7.87	8.05	7.81	6.81	7.10	7.58
Tb ppm	1.32	1.35	1.32	1.13	1.15	1.32
Dy ppm	8.25	8.39	8.33	6.75	6.88	8.28
Ho ppm	1.75	1.76	1.73	1.42	1.43	1.70
Er ppm	4.84	4.95	4.86	3.76	3.87	4.72
Tm ppm	0.74	0.75	0.73	0.56	0.56	0.72
Yb ppm	4.66	4.69	4.60	3.36	3.46	4.55
Lu ppm	0.77	0.78	0.74	0.55	0.55	0.74
Ba ppm	840	849	829	533	524	828
Th ppm	5.51	5.53	5.30	3.12	3.18	5.30
Nb ppm	15.03	15.18	14.79	9.47	9.42	14.64
Y ppm	48.85	49.80	47.28	37.39	38.64	46.87
Hf ppm	6.88	6.93	6.63	3.95	4.07	6.43
Ta ppm	1.04	1.03	0.99	0.66	0.65	0.98
Zr ppm	240	241	233	147	149	230
U ppm	2.63	2.67	2.78	1.64	1.51	2.80
Pb ppm	11.14	11.15	10.63	6.61	6.67	10.64
Rb ppm	65.7	66.2	62.3	36.2	36.1	62.2
Cs ppm	2.97	2.99	2.98	1.68	1.61	2.94
Sr ppm	224	223	241	441	442	248
Sc ppm	12.9	12.6	14.3	26.7	25.7	14.6

Section	ACAF1A7 8	ACAF1A8 8	ACAF1A9 8	ACAF1B1 8	ACAF1C2 8	ACAF1D1 8	ACAF1D2 8
SiO2	58.84	69.64	68.89	69.52	59.92	58.38	58.68
TiO2	1.31	0.53	0.55	0.52	1.21	1.36	1.34
Al2O3	16.23	15.10	15.15	15.04	16.27	16.31	16.37
FeO	6.21	2.19	2.25	2.19	6.21	6.34	6.31
Fe2O3	1.26	0.57	0.58	0.57	1.20	1.27	1.26
MnO	0.20	0.15	0.15	0.15	0.19	0.21	0.20
MgO	2.73	0.54	0.63	0.52	2.69	2.80	2.81
CaO	5.97	1.98	2.13	1.94	5.67	6.17	6.23
Na2O	4.52	5.51	5.48	5.41	3.97	4.47	4.42
K2O	1.63	2.93	2.90	2.98	1.59	1.57	1.57
P2O5	0.55	0.11	0.12	0.11	0.43	0.57	0.56
Total	99.45	99.25	98.84	98.94	99.35	99.44	99.74
FeO/MgO	1.39	2.54	2.24	2.64	1.41	1.38	1.37
Mg#	0.44	0.31	0.33	0.30	0.44	0.44	0.44
La ppm	19.19	27.26	26.93	27.04	17.77	18.75	18.32
Ce ppm	39.63	54.33	54.08	53.73	36.68	39.16	38.42
Pr ppm	5.31	6.84	6.77	6.83	4.78	5.31	5.26
Nd ppm	24.49	29.52	29.23	30.19	22.11	24.65	23.92
Sm ppm	6.59	7.80	7.79	7.83	6.00	6.61	6.50
Eu ppm	2.10	2.06	2.05	2.05	1.92	2.13	2.07
Gd ppm	6.73	7.65	7.53	8.02	6.22	6.70	6.54
Tb ppm	1.13	1.34	1.33	1.33	1.06	1.11	1.09
Dy ppm	6.84	8.22	8.26	8.30	6.29	6.84	6.74
Ho ppm	1.41	1.72	1.75	1.74	1.30	1.37	1.34
Er ppm	3.75	4.80	4.77	4.91	3.44	3.69	3.66
Tm ppm	0.54	0.73	0.74	0.74	0.51	0.54	0.53
Yb ppm	3.30	4.70	4.65	4.66	3.11	3.28	3.24
Lu ppm	0.53	0.73	0.75	0.78	0.50	0.52	0.51
Ba ppm	530	842	855	854	516	506	506
Th ppm	3.12	5.54	5.39	5.53	2.98	2.96	2.88
Nb ppm	9.05	14.97	15.24	15.08	9.29	8.76	8.86
Y ppm	36.56	47.49	48.53	49.43	35.29	37.03	35.98
Hf ppm	3.85	6.64	6.63	6.90	3.89	3.80	3.80
Ta ppm	0.63	1.00	0.99	1.01	0.64	0.60	0.58
Zr ppm	147	241	238	241	151	143	141
U ppm	1.65	2.91	2.95	2.65	1.52	1.56	1.53
Pb ppm	6.41	11.09	10.90	11.14	6.23	6.22	6.03
Rb ppm	34.5	64.1	67.9	66.2	36.7	34.1	33.9
Cs ppm	1.62	3.05	3.13	2.99	1.60	1.55	1.56
Sr ppm	446	220	223	223	412	469	455
Sc ppm	26.4	12.7	13.3	12.7	27.9	28.1	28.1

	ACAF1E1	ACAF1E2	ACAF1E3	ACAF1E4	ACAF1E5	AC30	AC31
Section	8	8	8	8	8	H	H
SiO2	58.06	58.82	57.90	57.37	57.66	61.04	59.77
TiO2	1.38	1.34	1.39	1.39	1.40	1.24	1.22
Al2O3	16.37	16.25	16.38	16.44	16.46	15.39	15.74
FeO	6.64	6.51	6.60	6.75	6.51	6.11	6.23
Fe2O3	1.31	1.29	1.31	1.32	1.27	1.33	1.29
MnO	0.21	0.20	0.21	0.21	0.21	0.19	0.19
MgO	2.93	2.95	2.94	3.00	3.08	1.77	2.14
CaO	6.43	6.28	6.35	6.57	6.65	4.80	5.33
Na2O	4.38	4.37	4.48	4.33	4.28	4.26	3.98
K2O	1.50	1.52	1.52	1.47	1.44	2.48	2.24
P2O5	0.57	0.55	0.60	0.59	0.60	0.40	0.37
Total	99.78	100.08	99.67	99.43	99.56	99.00	98.50
FeO/MgO	1.38	1.35	1.37	1.37	1.29	2.12	1.79
Mg#	0.44	0.45	0.44	0.44	0.46	0.34	0.38
La ppm	17.92	18.60	18.39	18.08	17.59	26.16	24.20
Ce ppm	37.54	38.59	38.90	37.88	36.72	52.97	50.09
Pr ppm	5.04	5.06	5.14	4.99	5.01	6.91	6.39
Nd ppm	23.33	23.30	23.97	23.13	22.92	30.39	28.60
Sm ppm	6.28	6.39	6.54	6.28	6.32	8.37	7.63
Eu ppm	2.06	2.02	2.06	2.05	2.02	2.16	2.10
Gd ppm	6.51	6.36	6.53	6.56	6.42	8.77	8.05
Tb ppm	1.07	1.09	1.10	1.07	1.05	1.46	1.34
Dy ppm	6.53	6.53	6.63	6.52	6.52	8.82	8.11
Ho ppm	1.32	1.32	1.37	1.32	1.30	1.82	1.69
Er ppm	3.55	3.61	3.67	3.57	3.48	5.05	4.78
Tm ppm	0.51	0.52	0.53	0.52	0.50	0.72	0.67
Yb ppm	3.16	3.23	3.24	3.09	3.08	4.50	4.29
Lu ppm	0.50	0.50	0.51	0.49	0.49	0.71	0.68
Ba ppm	490	505	497	483	475	746	712
Th ppm	2.81	2.84	2.82	2.74	2.68	6.19	5.60
Nb ppm	8.50	8.69	8.50	8.30	8.11	15.39	14.78
Y ppm	34.71	35.34	35.27	35.02	34.41	49.60	46.22
Hf ppm	3.56	3.64	3.60	3.47	3.41	6.60	6.04
Ta ppm	0.59	0.59	0.58	0.57	0.56	1.02	0.97
Zr ppm	138	140	139	137	132	225	207
U ppm	1.49	1.46	1.50	1.43	1.40	2.52	2.31
Pb ppm	5.75	6.06	5.80	5.65	5.73	7.99	6.30
Rb ppm	32.2	32.6	32.3	32.0	30.6	63.9	62.0
Cs ppm	1.46	1.53	1.48	1.43	1.42	2.79	2.09
Sr ppm	460	449	459	470	462	304	320
Sc ppm	28.5	27.4	27.4	28.6	28.2	24.3	25.7

	AC32	AC33	AC34	97ANB45	98AC15A1	98AC15A2	98AC15C
Section	**H**	**H**	**H**	**B**	**S**	**S**	**S**
SiO2	59.94	60.21	60.46	67.88	56.84	56.21	63.75
TiO2	1.30	1.28	1.27	0.71	1.40	1.41	0.98
Al2O3	15.68	15.54	15.48	15.35	15.96	16.28	15.70
FeO	6.47	6.39	6.26	3.28	6.60	6.93	4.38
Fe2O3	1.37	1.35	1.33	0.32	1.30	1.33	1.00
MnO	0.19	0.19	0.19	0.15	0.21	0.21	0.18
MgO	1.83	1.83	1.86	0.85	2.97	3.17	1.63
CaO	4.97	4.89	4.92	3.01	6.41	6.78	4.08
Na2O	4.26	4.11	4.17	4.92	4.22	4.16	4.88
K2O	2.36	2.39	2.40	2.63	1.45	1.41	2.31
P2O5	0.40	0.39	0.40	0.18	0.60	0.59	0.33
Total	98.76	98.58	98.73	99.28	97.95	98.48	99.20
FeO/MgO	2.17	2.15	2.07	2.26	1.36	1.33	1.66
Mg#	0.34	0.34	0.35	0.32	0.45	0.45	0.40
La ppm	28.10	27.60	29.81	23.77	17.51	17.63	22.15
Ce ppm	53.66	55.53	55.33	46.41	36.78	36.93	45.41
Pr ppm	7.35	7.13	7.51	5.79	4.86	4.86	5.83
Nd ppm	31.91	31.13	32.77	24.75	22.53	22.70	26.07
Sm ppm	8.76	8.58	8.91	6.43	6.17	6.24	7.05
Eu ppm	2.22	2.21	2.21	1.75	1.98	2.00	1.92
Gd ppm	9.32	8.78	9.63	6.82	6.37	6.46	7.15
Tb ppm	1.52	1.50	1.56	1.16	1.06	1.04	1.21
Dy ppm	9.21	9.12	9.52	7.21	6.38	6.34	7.56
Ho ppm	1.93	1.87	1.96	1.50	1.31	1.32	1.57
Er ppm	5.29	5.17	5.36	4.31	3.55	3.59	4.36
Tm ppm	0.76	0.75	0.76	0.64	0.50	0.51	0.64
Yb ppm	4.65	4.57	4.75	4.11	3.09	3.13	4.13
Lu ppm	0.75	0.73	0.76	0.65	0.49	0.49	0.66
Ba ppm	757	747	733	786	478	484	705
Th ppm	5.89	5.66	6.06	6.13	3.30	3.12	5.19
Nb ppm	14.60	14.60	14.67	13.44	8.23	8.17	12.28
Y ppm	52.76	51.81	54.26	41.71	34.17	34.60	42.05
Hf ppm	6.21	6.30	6.37	6.17	3.54	3.45	5.51
Ta ppm	1.01	1.00	1.02	0.93	0.57	0.56	0.85
Zr ppm	218	221	219	214	126	122	199
U ppm	2.44	2.29	2.45	2.56	1.29	1.28	2.19
Pb ppm	6.74	8.14	10.82	10.26	4.43	4.04	9.05
Rb ppm	60.9	61.6	59.6	64.7	30.7	30.3	54.5
Cs ppm	2.85	2.85	2.77	2.92	1.39	1.39	2.58
Sr ppm	315	311	307	264	446	472	305
Sc ppm	25.8	25.6	25.6	14.5	27.3	29.7	18.9

Section	98AC19A3C	98AC19DC	98AC21B23	98AC7-OD6	99AC25G	99AC26G	99AC27G
SiO2	57.51	64.21	68.07	64.31	59.40	68.76	66.66
TiO2	1.40	0.77	0.53	0.81	1.28	0.69	0.86
Al2O3	16.07	16.54	14.98	15.71	15.47	14.81	15.15
FeO	5.99	3.42	2.15	3.66	6.27	3.38	3.40
Fe2O3	1.21	0.78	0.55	0.85	1.32	0.28	0.84
MnO	0.21	0.17	0.15	0.16	0.19	0.16	0.17
MgO	2.73	1.29	0.63	1.17	2.10	0.69	0.97
CaO	5.95	3.98	1.97	3.12	5.09	2.25	2.85
Na2O	4.44	4.95	5.26	4.61	4.13	5.21	5.09
K2O	1.57	2.19	2.89	2.93	2.34	3.09	2.74
P2O5	0.66	0.23	0.10	0.25	0.40	0.14	0.22
Total	97.75	98.53	97.28	97.57	97.98	99.46	98.95
FeO/MgO	1.34	1.64	2.13	1.94	1.83	2.85	2.18
Mg#	0.45	0.40	0.34	0.36	0.37	0.27	0.34
La ppm	20.07	21.68	26.79	29.71	25.46	27.54	26.83
Ce ppm	41.99	43.95	54.16	60.60	52.36	55.52	54.70
Pr ppm	5.53	5.50	6.80	7.53	6.73	6.97	6.97
Nd ppm	25.68	24.23	29.82	32.81	30.26	30.55	30.82
Sm ppm	6.95	6.54	7.74	8.42	8.23	8.09	8.14
Eu ppm	2.20	1.83	2.01	2.08	2.16	2.03	2.15
Gd ppm	7.13	6.51	7.61	8.16	8.41	8.00	8.18
Tb ppm	1.16	1.10	1.33	1.41	1.41	1.41	1.41
Dy ppm	7.07	6.98	8.41	8.74	8.65	8.93	8.94
Ho ppm	1.41	1.44	1.76	1.83	1.77	1.84	1.86
Er ppm	3.90	4.04	4.95	5.10	4.88	5.29	5.17
Tm ppm	0.55	0.59	0.74	0.75	0.71	0.79	0.77
Yb ppm	3.38	3.77	4.80	4.76	4.49	5.02	4.94
Lu ppm	0.54	0.61	0.77	0.77	0.71	0.82	0.78
Ba ppm	553	733	877	822	734	881	840
Th ppm	3.56	5.19	6.49	7.90	5.88	6.97	6.30
Nb ppm	9.19	11.96	14.89	17.77	14.58	16.03	15.51
Y ppm	37.58	38.87	47.50	49.17	47.77	50.16	50.04
Hf ppm	3.86	5.36	6.96	7.62	6.29	7.40	6.80
Ta ppm	0.64	0.84	1.02	1.20	0.99	1.09	1.06
Zr ppm	138	193	248	281	225	266	247
U ppm	1.44	2.15	2.64	3.27	2.42	2.89	2.60
Pb ppm	6.42	9.16	11.05	11.47	9.09	11.37	10.53
Rb ppm	34.4	54.8	65.3	77.2	60.6	72.5	66.4
Cs ppm	1.61	2.53	3.08	3.67	2.84	3.42	3.10
Sr ppm	474	320	222	279	333	206	264
Sc ppm	25.3	15.7	12.8	17.4	25.4	15.5	17.4

	99AC28	99AC29	99AC30	99AC33	99AC35	99AC45	99AC46
Section	**G**	**G**	**G**	**5**	**5**	**I**	**I**
SiO2	56.96	58.03	68.07	68.90	56.78	60.53	68.96
TiO2	1.14	1.35	0.58	0.54	1.40	1.30	0.53
Al2O3	16.87	16.37	15.06	15.07	16.27	15.80	15.15
FeO	7.24	6.57	2.43	2.21	7.06	5.95	2.03
Fe2O3	1.28	1.30	0.61	0.57	1.36	1.26	0.53
MnO	0.17	0.21	0.15	0.15	0.21	0.19	0.15
MgO	3.57	3.03	0.73	0.67	3.16	2.19	0.55
CaO	7.62	6.47	2.23	2.03	6.78	5.30	1.98
Na2O	3.19	4.44	5.15	5.36	4.17	4.24	5.44
K2O	1.64	1.53	2.89	2.98	1.42	2.31	2.91
P2O5	0.24	0.56	0.13	0.11	0.57	0.40	0.10
Total	99.93	99.86	98.03	98.59	99.19	99.47	98.33
FeO/MgO	1.23	1.32	2.08	2.07	1.36	1.67	2.31
Mg#	0.47	0.45	0.35	0.35	0.44	0.40	0.33
La ppm	17.06	18.68	26.44	27.11	17.66	24.04	26.71
Ce ppm	35.13	38.95	53.48	54.59	36.66	49.50	53.88
Pr ppm	4.51	5.14	6.75	6.88	4.84	6.36	6.75
Nd ppm	20.29	23.88	29.46	30.21	22.66	28.78	29.67
Sm ppm	5.50	6.51	7.73	7.77	6.20	7.74	7.67
Eu ppm	1.47	2.02	2.05	2.04	1.97	2.08	2.03
Gd ppm	5.68	6.72	7.56	7.74	6.37	7.92	7.58
Tb ppm	0.96	1.09	1.33	1.34	1.06	1.34	1.32
Dy ppm	6.08	6.75	8.27	8.55	6.45	8.34	8.39
Ho ppm	1.23	1.37	1.75	1.76	1.30	1.73	1.76
Er ppm	3.40	3.74	4.97	4.96	3.54	4.68	4.91
Tm ppm	0.49	0.54	0.73	0.74	0.50	0.69	0.74
Yb ppm	3.10	3.30	4.68	4.79	3.16	4.23	4.78
Lu ppm	0.49	0.53	0.75	0.78	0.50	0.68	0.78
Ba ppm	529	525	860	878	489	698	868
Th ppm	4.10	3.37	6.29	6.42	3.10	5.64	6.46
Nb ppm	9.70	8.74	14.69	15.02	8.03	13.78	15.03
Y ppm	32.72	36.04	47.07	47.98	34.45	45.45	47.66
Hf ppm	4.30	3.72	6.66	6.81	3.47	5.96	6.81
Ta ppm	0.69	0.61	1.00	1.01	0.55	0.95	1.01
Zr ppm	153	132	241	246	121	214	245
U ppm	1.64	1.38	2.53	2.61	1.24	2.29	2.61
Pb ppm	6.73	6.07	10.82	10.87	5.67	8.76	10.94
Rb ppm	42.8	33.3	64.7	66.7	30.4	58.0	66.5
Cs ppm	1.65	1.59	3.06	3.08	1.38	2.69	3.14
Sr ppm	331	466	240	232	471	328	221
Sc ppm	28.1	28.6	13.8	13.2	29.5	25.7	13.0

	99AC47A	99AC49	99AC50	99AC53	99AC55	99AC57	99AC59
Section	**I**	**I**	**I**	**I**	**K**	**K**	**K**
SiO2	58.47	60.50	62.17	58.20	68.76	57.94	58.28
TiO2	1.38	1.31	1.21	1.43	0.53	1.35	1.41
Al2O3	16.46	15.86	15.63	16.41	14.98	16.33	16.50
FeO	6.26	6.15	5.46	6.17	1.97	6.37	5.98
Fe2O3	1.25	1.29	1.20	1.23	0.51	1.26	1.20
MnO	0.21	0.19	0.19	0.21	0.15	0.21	0.21
MgO	2.89	2.27	1.81	2.92	0.54	2.95	2.85
CaO	6.30	5.42	4.69	6.38	1.96	6.48	6.23
Na2O	4.45	4.23	4.32	4.40	5.33	4.33	4.51
K2O	1.55	2.27	2.59	1.50	2.96	1.54	1.55
P2O5	0.61	0.39	0.41	0.64	0.10	0.55	0.66
Total	99.82	99.88	99.69	99.49	97.80	99.31	99.40
FeO/MgO	1.32	1.66	1.86	1.29	2.29	1.32	1.28
Mg#	0.45	0.40	0.37	0.46	0.33	0.45	0.46
La ppm	19.42	23.07	27.40	18.90	26.81	18.20	19.46
Ce ppm	40.38	47.78	55.87	39.32	54.07	38.13	40.42
Pr ppm	5.34	6.16	7.11	5.18	6.83	4.96	5.37
Nd ppm	24.73	27.64	31.93	24.05	29.64	23.14	24.85
Sm ppm	6.73	7.50	8.59	6.57	7.75	6.42	6.77
Eu ppm	2.12	2.04	2.21	2.10	2.04	2.02	2.15
Gd ppm	6.91	7.77	8.58	6.91	7.62	6.49	6.93
Tb ppm	1.15	1.31	1.47	1.12	1.33	1.07	1.13
Dy ppm	6.99	7.96	8.94	6.67	8.16	6.54	6.82
Ho ppm	1.42	1.64	1.86	1.38	1.76	1.33	1.42
Er ppm	3.84	4.51	5.04	3.61	4.81	3.53	3.66
Tm ppm	0.54	0.65	0.74	0.52	0.74	0.52	0.54
Yb ppm	3.36	4.11	4.69	3.20	4.68	3.22	3.32
Lu ppm	0.54	0.66	0.74	0.52	0.76	0.51	0.52
Ba ppm	538	666	777	514	858	508	528
Th ppm	3.50	5.27	6.34	3.32	6.30	3.28	3.33
Nb ppm	9.18	13.44	15.70	8.53	14.82	8.57	8.88
Y ppm	37.54	44.10	49.81	36.07	47.62	35.28	36.87
Hf ppm	3.86	5.75	6.82	3.62	6.85	3.69	3.71
Ta ppm	0.64	0.91	1.07	0.59	1.00	0.59	0.59
Zr ppm	136	207	245	129	245	130	133
U ppm	1.43	2.16	2.59	1.34	2.58	1.34	1.35
Pb ppm	6.35	8.33	9.98	5.81	10.84	5.98	6.11
Rb ppm	34.5	55.3	65.9	32.4	65.5	32.5	33.4
Cs ppm	1.58	2.54	3.03	1.46	3.04	1.48	1.52
Sr ppm	477	326	309	466	218	442	472
Sc ppm	28.3	25.7	22.9	26.9	12.5	27.0	25.8

	99AC75	99AC76	99AC77	99AC79	99AC80	99AC84	99AC-LBG
Section	**M**	**M**	**M**	**L**	**L**	**2**	**G**
SiO2	58.48	57.70	60.54	57.98	68.57	58.71	67.91
TiO2	1.38	1.43	0.57	1.37	0.54	1.44	0.53
Al2O3	16.47	16.48	16.49	16.47	14.91	16.28	15.79
FeO	5.94	6.44	4.29	6.30	2.07	5.85	3.34
Fe2O3	1.19	1.26	0.77	1.24	0.54	1.20	0.70
MnO	0.22	0.21	0.24	0.21	0.15	0.21	0.15
MgO	2.83	3.02	3.04	3.03	0.58	2.69	1.48
CaO	6.26	6.54	5.80	6.65	2.01	5.97	4.55
Na2O	4.39	4.26	2.70	4.29	5.39	4.58	3.27
K2O	1.57	1.46	1.67	1.48	2.90	1.59	1.73
P2O5	0.59	0.62	0.17	0.57	0.11	0.69	0.18
Total	99.31	99.42	96.27	99.60	97.77	99.21	99.63
FeO/MgO	1.28	1.30	0.86	1.27	2.24	1.33	1.38
Mg#	0.46	0.46	0.56	0.46	0.33	0.45	0.44
La ppm	19.09	18.77	16.02	18.06	27.05	20.00	23.39
Ce ppm	39.87	39.22	26.17	37.66	54.34	41.72	47.06
Pr ppm	5.24	5.18	3.27	4.97	6.86	5.49	5.42
Nd ppm	24.18	23.99	13.34	23.01	29.69	25.47	21.67
Sm ppm	6.56	6.63	3.10	6.32	7.77	6.94	4.35
Eu ppm	2.07	2.10	0.97	2.01	2.02	2.18	1.25
Gd ppm	6.80	6.89	2.84	6.51	7.74	7.06	3.65
Tb ppm	1.12	1.11	0.43	1.07	1.33	1.15	0.51
Dy ppm	6.69	6.65	2.59	6.45	8.43	6.96	2.77
Ho ppm	1.39	1.38	0.51	1.34	1.78	1.42	0.51
Er ppm	3.70	3.59	1.36	3.53	4.90	3.81	1.34
Tm ppm	0.54	0.51	0.20	0.51	0.74	0.55	0.19
Yb ppm	3.34	3.24	1.27	3.21	4.75	3.40	1.21
Lu ppm	0.53	0.51	0.21	0.51	0.78	0.53	0.19
Ba ppm	529	507	407	499	864	540	780
Th ppm	3.44	3.28	4.38	3.20	6.38	3.51	3.60
Nb ppm	8.75	8.64	3.94	8.30	14.81	9.18	8.70
Y ppm	36.36	35.96	15.18	34.91	47.65	37.54	14.28
Hf ppm	3.80	3.64	2.23	3.63	6.75	3.81	2.67
Ta ppm	0.61	0.59	0.30	0.59	1.01	0.64	0.59
Zr ppm	134	128	83	127	245	136	96
U ppm	1.40	1.32	1.24	1.30	2.59	1.42	0.81
Pb ppm	6.19	5.85	4.28	5.82	10.86	6.34	6.29
Rb ppm	33.9	31.5	42.9	31.7	65.3	34.5	46.1
Cs ppm	1.53	1.43	3.48	1.44	3.03	1.57	1.46
Sr ppm	451	467	402	456	220	470	448
Sc ppm	26.4	27.1	16.0	28.7	12.5	25.4	9.3

Appendix B: Plagioclase Analyses

Analyses were obtained using a Cameca SX-50 electron microprobe at the University of Alaska Fairbanks. Analytical conditions were 15 keV accelerating voltage, 10 na beam current, and a 10 μm spot size. Peak and background measurements were made for 10 seconds each. "Line number" refers to the analysis number in a particular microprobe session. "Host" refers to the rock type containing the analyzed sample. **CFE and** – caldera forming eruption andesite; **CFE RD** - caldera forming eruption rhyodacite; **L. Bk. Nose** – lower Black Nose pumice; **U. Bk. Nose** – upper Black Nose pumice; **Aniak. I** – Aniakchak I andesite; **HAB** – precaldera high-alumina basalt; **PreCald RD** – precaldera rhyodacite lava.

Host Line Numbers	98AC3A CFE and 28	98AC3A CFE and 29	98AC3A CFE and 30	98AC3A CFE and 31	98AC3A CFE and 32	98AC3A CFE and 33	98AC3A CFE and 34	98AC3A CFE and 35
SiO2	57.83	58.30	57.93	58.82	58.74	58.42	58.48	59.02
Al2O3	25.53	25.79	26.60	25.83	25.55	26.07	26.59	26.12
CaO	8.26	8.51	8.36	7.63	7.67	8.44	8.15	7.70
Na2O	6.90	7.10	7.02	7.14	7.24	7.08	7.05	6.95
K2O	0.30	0.30	0.29	0.34	0.30	0.30	0.36	0.37
FeO	0.32	0.40	0.54	0.34	0.57	0.41	0.32	0.32
Total	99.14	100.39	100.73	100.12	100.07	100.70	100.95	100.49
An	39.14	39.23	39.06	36.40	36.29	39.08	38.19	37.17
Ab	59.19	59.15	59.35	61.64	62.04	59.29	59.80	60.71
Or	1.67	1.62	1.59	1.96	1.68	1.63	2.01	2.12

Host Line Numbers	98AC3A CFE and 38	98AC3A CFE and 39	98AC3A CFE and 40	98AC3A CFE and 41	98AC3A CFE and 42	98AC3A CFE and 43	98AC3A CFE and 44	98AC3A CFE and 45
SiO2	57.62	56.94	57.53	57.63	57.82	58.91	60.80	58.26
Al2O3	26.26	26.54	26.28	26.66	26.77	26.41	24.79	26.58
CaO	8.81	8.89	8.43	8.65	8.64	8.09	6.52	8.10
Na2O	6.70	6.55	6.82	6.78	6.82	7.17	7.97	6.82
K2O	0.27	0.26	0.26	0.32	0.27	0.31	0.40	0.29
FeO	0.24	0.49	0.55	0.49	0.43	0.36	0.43	0.40
Total	99.90	99.69	99.86	100.52	100.74	101.25	100.91	100.45
An	41.47	42.20	39.97	40.61	40.55	37.74	30.45	38.99
Ab	57.04	56.31	58.55	57.62	57.96	60.55	67.34	59.35
Or	1.49	1.49	1.47	1.77	1.49	1.71	2.21	1.66

Host Line Numbers	98AC3A CFE and 48	98AC3A CFE and 49	98AC3A CFE and 50	98AC3A CFE and 51	98AC3A CFE and 52	98AC3A CFE and 53	98AC3A CFE and 54	98AC3A CFE and 55
SiO2	46.96	47.97	46.93	46.77	46.54	58.37	58.38	57.79
Al2O3	34.22	33.48	33.98	34.27	33.65	26.39	25.98	26.39
CaO	17.29	16.43	17.14	17.32	17.65	8.60	8.39	8.49
Na2O	1.78	2.16	1.93	1.75	1.79	7.01	7.03	6.92
K2O	0.06	0.04	0.01	0.02	0.04	0.30	0.25	0.31
FeO	0.67	0.83	0.71	0.96	0.88	0.44	0.50	0.35
Total	100.98	100.91	100.70	101.08	100.55	101.11	100.53	100.25
An	83.99	80.59	83.02	84.49	84.31	39.74	39.20	39.69
Ab	15.64	19.18	16.91	15.41	15.49	58.63	59.43	58.60
Or	0.37	0.23	0.07	0.10	0.20	1.63	1.36	1.71

Host	98AC3A CFE and	98AC3A CFE and	98AC3C CFE and	98AC3C CFE and	98AC3C CFE and	98AC3C CFE and	98AC3C CFE and
Line Numbers	36	37	58	59	60	61	62
SiO2	58.60	58.61	54.77	53.99	55.14	54.41	55.10
Al2O3	26.56	26.59	28.05	28.38	28.00	28.46	28.14
CaO	8.28	8.08	11.47	11.66	11.07	11.29	11.05
Na2O	6.86	7.04	5.39	5.06	5.47	5.16	5.29
K2O	0.29	0.32	0.18	0.17	0.18	0.16	0.17
FeO	0.43	0.37	0.35	0.61	0.48	0.59	0.47
Total	101.01	101.01	100.21	99.87	100.34	100.07	100.22
An	39.37	38.08	53.50	55.45	52.26	54.24	53.04
Ab	59.01	60.10	45.50	43.59	46.74	44.84	46.00
Or	1.62	1.82	1.00	0.95	1.00	0.92	0.95

Host	98AC3A CFE and	98AC3A CFE and	98AC3C CFE and	98AC3C CFE and	98AC3C CFE and	98AC3C CFE and	98AC3C CFE and
Line Numbers	46	47	66	67	68	69	70
SiO2	57.89	58.22	47.90	47.84	45.96	45.53	45.80
Al2O3	26.02	26.45	31.86	32.08	33.16	33.42	33.37
CaO	8.35	8.25	16.33	16.51	18.02	17.72	18.17
Na2O	7.39	6.94	2.37	2.45	1.35	1.65	1.49
K2O	0.30	0.27	0.05	0.05	0.02	0.04	0.02
FeO	0.52	0.39	0.60	0.65	0.93	0.78	0.81
Total	100.46	100.52	99.12	99.57	99.45	99.14	99.66
An	37.80	39.04	78.91	78.65	87.97	85.39	86.94
Ab	60.57	59.46	20.77	21.09	11.91	14.39	12.93
Or	1.62	1.50	0.32	0.26	0.12	0.23	0.13

Host	98AC3A CFE and	98AC3A CFE and	98AC3C CFE and	98AC3C CFE and	98AC3C CFE and	98AC3C CFE and	98AC3G CFE and
Line Numbers	56	57	79	80	81	82	83
SiO2	60.51	60.11	58.21	56.27	58.48	53.70	54.57
Al2O3	24.13	24.88	25.93	26.91	25.95	28.40	28.24
CaO	6.55	7.42	8.66	9.47	8.14	11.81	11.99
Na2O	7.98	7.50	6.61	6.21	6.98	4.56	5.01
K2O	0.39	0.32	0.23	0.25	0.25	0.27	0.16
FeO	0.28	0.68	0.59	0.39	0.54	0.89	0.63
Total	99.83	100.90	100.23	99.49	100.33	99.63	100.61
An	30.53	34.71	41.46	45.10	38.61	57.95	56.44
Ab	67.32	63.49	57.24	53.49	59.99	40.49	42.66
Or	2.15	1.80	1.30	1.41	1.40	1.56	0.90

Host	98AC3C CFE and	98AC3C CFE and	98AC3C CFE and	98AC3G CFE and	98AC3H CFE and	98AC3H CFE and	98AC3H CFE and
Line Numbers	63	64	65	87	88	89	90
SiO2	48.97	47.78	48.01	54.03	61.37	58.99	58.53
Al2O3	31.83	32.57	31.35	28.24	24.03	25.69	25.65
CaO	15.99	16.61	16.57	11.52	5.81	7.93	7.45
Na2O	2.42	2.15	2.31	5.14	8.18	7.23	7.33
K2O	0.05	0.03	0.08	0.14	0.38	0.26	0.31
FeO	0.63	0.56	0.76	0.58	0.24	0.57	0.24
Total	99.89	99.69	99.08	99.66	100.02	100.67	99.51
An	78.24	80.91	79.50	54.88	27.58	37.18	35.33
Ab	21.44	18.91	20.07	44.31	70.25	61.36	62.92
Or	0.32	0.18	0.43	0.80	2.16	1.46	1.75

Host	98AC3C CFE and	98AC3C CFE and	98AC3C CFE and	98AC3H CFE and	98AC3H CFE and	98AC3H CFE and	98AC3H CFE and
Line Numbers	71	72	78	95	96	97	98
SiO2	45.76	48.50	58.31	71.83	73.29	73.58	53.28
Al2O3	33.23	30.52	26.16	14.94	14.43	14.28	29.53
CaO	18.30	14.92	8.78	1.09	1.03	1.10	11.96
Na2O	1.35	3.22	6.72	5.06	4.64	4.62	4.90
K2O	0.03	0.13	0.28	3.94	3.87	3.99	0.14
FeO	0.91	1.36	0.25	2.19	1.76	2.17	0.65
Total	99.57	98.64	100.51	99.06	99.02	99.74	100.46
An	88.11	71.41	41.25	7.32	7.34	7.77	56.98
Ab	11.73	27.86	57.16	61.28	59.85	58.81	42.24
Or	0.16	0.73	1.59	31.40	32.81	33.42	0.78

Host	98AC3G CFE and	98AC3G CFE and	98AC3G CFE and	98AC3H CFE and	98AC3H CFE and	98AC3H CFE and	98AC3H CFE and
Line Numbers	84	85	86	103	104	105	106
SiO2	53.86	53.95	54.38	58.32	58.55	57.79	57.95
Al2O3	28.80	28.83	28.05	25.50	25.52	26.20	25.91
CaO	11.56	11.72	11.43	8.53	8.15	8.73	8.19
Na2O	5.07	5.29	5.18	6.78	6.69	6.75	6.79
K2O	0.12	0.13	0.15	0.25	0.28	0.23	0.25
FeO	0.69	0.50	0.63	0.47	0.29	0.37	0.41
Total	100.11	100.41	99.81	99.85	99.47	100.06	99.49
An	55.38	54.64	54.45	40.42	39.58	41.17	39.43
Ab	43.96	44.66	44.71	58.16	58.80	57.56	59.15
Or	0.67	0.70	0.84	1.42	1.62	1.27	1.42

Host	98AC3H CFE and	98AC3H CFE and	98AC3H CFE and	98AC3H CFE and	98AC3H CFE and	98AC3H CFE and	AC14 L. Bk Nose
Line Numbers	91	92	93	94	111	112	148
SiO2	57.76	71.86	72.82	73.30	58.96	58.58	59.32
Al2O3	25.48	13.82	14.53	14.43	25.51	25.92	25.97
CaO	7.97	1.53	1.29	1.11	7.88	8.00	8.05
Na2O	7.53	4.63	4.76	4.82	7.19	7.28	7.15
K2O	0.30	3.93	3.94	3.87	0.31	0.25	0.44
FeO	0.43	2.85	2.22	2.44	0.38	0.43	0.35
Total	99.47	98.62	99.56	99.97	100.23	100.46	101.28
An	36.30	10.52	8.87	7.71	37.08	37.25	37.45
Ab	62.07	57.43	58.98	60.39	61.20	61.35	60.14
Or	1.64	32.05	32.15	31.91	1.72	1.39	2.41

Host	98AC3H CFE and	98AC3H CFE and	98AC3H CFE and	98AC3H CFE and	AC14 L. Bk Nose	AC14 L. Bk Nose	AC14 L. Bk Nose
Line Numbers	99	100	101	102	154	155	156
SiO2	53.64	53.51	53.51	53.06	58.37	57.69	58.16
Al2O3	29.05	29.05	29.20	29.81	27.11	27.29	25.99
CaO	12.01	11.97	11.91	12.12	8.37	8.71	8.52
Na2O	4.93	4.70	5.08	4.67	6.48	6.42	6.78
K2O	0.14	0.12	0.16	0.10	0.33	0.34	0.30
FeO	0.80	0.66	0.57	0.56	0.60	0.42	0.55
Total	100.56	100.00	100.43	100.34	101.25	100.88	100.32
An	56.92	58.06	55.94	58.57	40.86	42.01	40.29
Ab	42.31	41.24	43.17	40.85	57.21	56.05	58.02
Or	0.77	0.70	0.89	0.58	1.93	1.94	1.70

Host	98AC3H CFE and	98AC3H CFE and	98AC3H CFE and	98AC3H CFE and	AC14 L. Bk Nose	AC14 L. Bk Nose	AC14 L. Bk Nose
Line Numbers	107	108	109	110	162	163	164
SiO2	56.27	58.66	58.77	58.94	58.65	58.63	57.12
Al2O3	26.94	25.94	25.56	24.90	25.63	25.40	26.50
CaO	9.39	8.35	8.28	7.88	8.33	7.88	8.90
Na2O	6.41	6.75	6.79	7.04	6.90	7.04	6.46
K2O	0.25	0.27	0.36	0.29	0.32	0.36	0.29
FeO	0.41	0.25	0.36	0.36	0.47	0.51	0.38
Total	99.66	100.22	100.13	99.41	100.31	99.81	99.64
An	44.14	39.97	39.45	37.58	39.31	37.44	42.52
Ab	54.47	58.47	58.49	60.77	58.87	60.52	55.86
Or	1.39	1.55	2.06	1.65	1.82	2.03	1.62

	AC14	AC14	AC14	AC14	AC14	AC14	AC14
Host	**L. Bk Nose**	**L. Bk Nose**	**L. Bk Nose**	**L. Bk Nose**	**L. Bk Nose**	**L. Bk Nose**	**L. Bk Nose**
Line Numbers	**149**	**150**	**151**	**152**	**153**	**170**	**171**
SiO2	58.80	58.99	58.28	58.43	58.58	57.82	69.43
Al2O3	26.07	26.02	26.06	26.60	26.78	26.39	15.04
CaO	8.20	7.72	7.73	8.38	7.96	8.51	1.97
Na2O	6.90	7.29	6.98	6.71	6.95	6.79	5.69
K2O	0.42	0.39	0.39	0.35	0.39	0.40	3.14
FeO	0.36	0.32	0.34	0.33	0.47	0.46	3.53
Total	100.75	100.72	99.77	100.80	101.13	100.36	98.79
An	38.71	36.10	37.12	40.01	37.91	40.01	12.30
Ab	58.95	61.73	60.67	57.98	59.87	57.76	64.35
Or	2.34	2.17	2.21	2.01	2.22	2.23	23.35

	AC14	AC14	AC14	AC14	AC14	AC14	AC14
Host	**L. Bk Nose**	**L. Bk Nose**	**L. Bk Nose**	**L. Bk Nose**	**L. Bk Nose**	**L. Bk Nose**	**L. Bk Nose**
Line Numbers	**157**	**158**	**159**	**160**	**161**	**178**	**179**
SiO2	57.53	58.06	59.05	57.80	57.69	57.66	61.56
Al2O3	26.34	26.02	25.03	25.92	26.25	26.69	23.33
CaO	8.79	8.54	7.82	8.40	8.71	8.34	6.58
Na2O	6.46	6.74	7.18	6.83	6.84	6.76	6.63
K2O	0.38	0.37	0.42	0.37	0.30	0.37	1.20
FeO	0.36	0.46	0.42	0.50	0.56	0.65	1.21
Total	99.85	100.19	99.92	99.82	100.36	100.46	100.51
An	41.99	40.34	36.68	39.62	40.63	39.69	32.88
Ab	55.87	57.60	60.97	58.29	57.72	58.23	60.00
Or	2.14	2.06	2.35	2.09	1.65	2.08	7.12

	AC14	AC14	AC14	AC14	AC14	AC14	AC14
Host	**L. Bk Nose**	**L. Bk Nose**	**L. Bk Nose**	**L. Bk Nose**	**L. Bk Nose**	**L. Bk Nose**	**L. Bk Nose**
Line Numbers	**165**	**166**	**167**	**168**	**169**	**186**	**187**
SiO2	58.14	57.36	58.59	59.28	57.91	58.04	58.26
Al2O3	26.77	26.78	26.31	25.85	26.69	26.64	26.56
CaO	9.01	8.39	7.78	7.74	8.31	8.47	8.15
Na2O	6.73	6.69	6.99	7.17	6.76	6.77	7.05
K2O	0.38	0.35	0.43	0.37	0.36	0.33	0.34
FeO	0.55	0.53	0.28	0.34	0.61	0.46	0.52
Total	101.57	100.10	100.39	100.75	100.63	100.71	100.88
An	41.66	40.10	37.15	36.57	39.61	40.12	38.22
Ab	56.27	57.91	60.39	61.37	58.35	58.02	59.87
Or	2.07	1.99	2.46	2.06	2.04	1.86	1.91

	AC14	AC14	AC14	AC14	AC14	AC14	AC14
Host	**L. Bk Nose**	**L. Bk Nose**	**L. Bk Nose**	**L. Bk Nose**	**L. Bk Nose**	**L. Bk Nose**	**L. Bk Nose**
Line Numbers	**172**	**173**	**174**	**175**	**176**	**177**	**194**
SiO2	59.05	58.83	57.63	58.23	58.43	58.18	60.01
Al2O3	25.60	23.68	26.38	26.29	26.56	26.28	25.29
CaO	7.96	7.07	8.68	7.93	8.57	8.62	7.05
Na2O	7.22	6.59	6.68	6.98	6.51	6.51	7.77
K2O	0.40	0.88	0.36	0.35	0.37	0.35	0.42
FeO	0.22	0.97	0.45	0.58	0.51	0.44	0.52
Total	100.45	98.02	100.19	100.36	100.95	100.37	101.06
An	37.01	35.27	40.96	37.84	41.19	41.43	32.62
Ab	60.77	59.48	57.01	60.20	56.67	56.58	65.04
Or	2.21	5.25	2.04	1.96	2.14	1.99	2.34

	AC14	AC14	AC14	AC14	AC14	AC14	AC14
Host	**L. Bk Nose**	**L. Bk Nose**	**L. Bk Nose**	**L. Bk Nose**	**L. Bk Nose**	**L. Bk Nose**	**L. Bk Nose**
Line Numbers	**180**	**181**	**182**	**183**	**184**	**185**	**203**
SiO2	57.73	57.51	58.06	57.50	58.98	58.25	69.77
Al2O3	26.71	26.96	26.65	27.35	25.60	26.28	15.17
CaO	9.18	8.84	8.56	8.60	7.43	7.81	2.21
Na2O	6.72	6.77	6.81	6.56	7.27	7.23	5.11
K2O	0.31	0.29	0.35	0.35	0.42	0.36	3.16
FeO	0.42	0.52	0.46	0.43	0.44	0.42	3.21
Total	101.08	100.89	100.90	100.79	100.14	100.36	98.64
An	42.30	41.24	40.19	41.17	35.24	36.62	14.54
Ab	55.98	57.16	57.84	56.87	62.37	61.36	60.72
Or	1.73	1.60	1.97	1.97	2.39	2.02	24.74

	AC14	AC14	AC14	AC14	AC14	AC14	AC34
Host	**L. Bk Nose**	**L. Bk Nose**	**L. Bk Nose**	**L. Bk Nose**	**L. Bk Nose**	**L. Bk Nose**	**Aniak. I**
Line Numbers	**188**	**189**	**190**	**191**	**192**	**193**	**211**
SiO2	58.02	58.36	58.92	58.79	58.84	59.08	55.58
Al2O3	27.40	26.55	26.29	26.87	26.10	25.93	28.39
CaO	8.49	8.33	8.18	8.51	7.95	7.52	10.54
Na2O	6.73	6.52	6.85	6.94	6.98	7.24	5.65
K2O	0.31	0.28	0.40	0.33	0.35	0.50	0.36
FeO	0.50	0.42	0.44	0.47	0.50	0.46	0.63
Total	101.45	100.45	101.09	101.92	100.73	100.73	101.15
An	40.37	40.73	38.86	39.66	37.86	35.45	49.74
Ab	57.88	57.66	58.86	58.49	60.14	61.75	48.27
Or	1.75	1.61	2.28	1.85	1.99	2.80	2.00

	AC14	AC14	AC14	AC14	AC14	AC14	AC14
Host	**L. Bk Nose**	**L. Bk Nose**	**L. Bk Nose**	**L. Bk Nose**	**L. Bk Nose**	**L. Bk Nose**	**L. Bk Nose**
Line Numbers	**195**	**196**	**197**	**199**	**200**	**201**	**202**
SiO2	59.05	58.00	57.93	57.90	59.71	59.43	59.20
Al2O3	26.36	27.07	27.14	26.96	25.93	25.95	26.16
CaO	7.81	8.42	8.85	8.18	7.23	7.56	7.60
Na2O	7.16	6.59	6.82	7.20	7.40	7.39	7.39
K2O	0.42	0.30	0.34	0.41	0.40	0.43	0.47
FeO	0.45	0.49	0.51	0.41	0.41	0.53	0.33
Total	101.25	100.87	101.58	101.05	101.08	101.30	101.15
An	36.71	40.69	40.99	37.73	34.25	35.24	35.29
Ab	60.94	57.61	57.13	60.05	63.48	62.36	62.14
Or	2.35	1.70	1.88	2.22	2.27	2.40	2.57

	AC34	AC34	AC34	AC34	AC34	AC34	AC34
Host	**Aniak. I**	**Aniak. I**	**Aniak. I**	**Aniak. I**	**Aniak. I**	**Aniak. I**	**Aniak. I**
Line Numbers	**204**	**205**	**206**	**207**	**208**	**209**	**210**
SiO2	56.13	55.54	56.04	54.76	57.05	57.19	55.79
Al2O3	28.47	28.51	28.05	28.57	27.07	27.15	28.20
CaO	10.10	10.68	9.85	10.12	9.12	9.39	10.07
Na2O	5.61	5.28	5.75	5.76	6.37	6.09	5.84
K2O	0.34	0.35	0.37	0.37	0.47	0.46	0.34
FeO	0.67	0.42	0.40	0.41	0.42	0.51	0.51
Total	101.32	100.79	100.45	99.97	100.50	100.79	100.74
An	48.91	51.71	47.61	48.22	42.99	44.82	47.87
Ab	49.12	46.25	50.28	49.71	54.35	52.59	50.21
Or	1.97	2.04	2.11	2.07	2.66	2.60	1.92

	AC34	AC34	AC34	AC34	AC34	AC34	AC34
Host	**Aniak. I**	**Aniak. I**	**Aniak. I**	**Aniak. I**	**Aniak. I**	**Aniak. I**	**Aniak. I**
Line Numbers	**212**	**213**	**214**	**215**	**216**	**217**	**218**
SiO2	56.37	55.64	55.22	55.63	54.70	54.43	54.66
Al2O3	28.54	28.39	28.27	28.38	28.80	29.05	28.93
CaO	10.28	10.38	10.58	10.54	11.35	11.11	11.11
Na2O	5.74	5.61	5.57	5.70	5.07	5.02	5.01
K2O	0.35	0.39	0.34	0.32	0.34	0.30	0.33
FeO	0.59	0.40	0.44	0.70	0.50	0.34	0.51
Total	101.86	100.81	100.41	101.29	100.75	100.25	100.54
An	48.74	49.43	50.24	49.64	54.23	54.08	54.05
Ab	49.28	48.34	47.87	48.57	43.86	44.19	44.04
Or	1.98	2.23	1.90	1.79	1.91	1.72	1.90

Host	AC34 Aniak. I	AC34 Aniak. I	AC34 Aniak. I	AC34 Aniak. I	AC34 Aniak. I	AC34 Aniak. I	AC34 Aniak. I
Line Numbers	219	220	221	222	223	224	225
SiO2	55.31	55.59	54.89	56.01	52.66	55.43	55.30
Al2O3	28.79	28.28	28.94	28.12	29.99	28.10	28.20
CaO	10.61	10.30	11.10	9.96	12.59	10.85	11.07
Na2O	5.49	5.61	5.17	5.63	4.40	5.65	5.20
K2O	0.31	0.33	0.29	0.39	0.19	0.35	0.30
FeO	0.65	0.31	0.36	0.47	0.60	0.42	0.30
Total	101.15	100.41	100.74	100.58	100.43	100.81	100.38
An	50.72	49.41	53.35	48.33	60.60	50.46	53.12
Ab	47.50	48.71	45.00	49.44	38.31	47.58	45.15
Or	1.78	1.88	1.65	2.24	1.09	1.96	1.73

Host	AC34 Aniak. I	AC34 Aniak. I	AC34 Aniak. I	AC34 Aniak. I	AC34 Aniak. I	AC34 Aniak. I	AC34 Aniak. I
Line Numbers	227	228	229	230	231	232	233
SiO2	52.30	55.27	55.54	55.74	52.26	49.79	49.94
Al2O3	29.62	28.79	28.31	28.05	30.21	29.94	32.17
CaO	12.97	10.87	10.43	10.13	13.03	14.20	14.82
Na2O	4.30	5.47	5.57	5.64	4.19	3.18	3.16
K2O	0.20	0.35	0.35	0.30	0.19	0.22	0.13
FeO	0.70	0.52	0.33	0.35	0.66	1.95	0.84
Total	100.09	101.28	100.55	100.21	100.54	99.29	101.06
An	61.78	51.30	49.83	48.95	62.52	70.21	71.59
Ab	37.08	46.71	48.17	49.33	36.40	28.47	27.64
Or	1.14	2.00	2.00	1.73	1.07	1.32	0.77

Host	AC34 Aniak. I	AC34 Aniak. I	AC34 Aniak. I	AC34 Aniak. I	AC34 Aniak. I	AC34 Aniak. I	AC34 Aniak. I
Line Numbers	235	236	237	238	239	240	241
SiO2	51.60	54.77	54.37	54.68	55.02	53.89	55.56
Al2O3	30.36	28.64	28.88	28.71	28.77	28.91	28.91
CaO	13.76	11.32	11.36	11.45	11.19	11.23	10.91
Na2O	3.72	5.28	4.95	5.14	5.13	4.97	5.23
K2O	0.13	0.37	0.27	0.32	0.29	0.28	0.34
FeO	0.84	0.39	0.41	0.64	0.49	0.41	0.66
Total	100.41	100.77	100.24	100.94	100.89	99.69	101.62
An	66.63	53.13	55.01	54.18	53.76	54.66	52.52
Ab	32.62	44.82	43.43	44.00	44.59	43.73	45.55
Or	0.74	2.05	1.56	1.82	1.65	1.61	1.93

	AC34	AC34	AC34	AC34	AC34	AC34	AC34
Host	**Aniak. I**	**Aniak. I**	**Aniak. I**	**Aniak. I**	**Aniak. I**	**Aniak. I**	**Aniak. I**
Line Numbers	**226**	**243**	**244**	**245**	**246**	**247**	**248**
SiO2	55.41	55.66	55.51	55.45	56.06	55.43	56.36
Al2O3	28.35	28.36	28.52	28.36	28.09	27.81	27.72
CaO	10.47	10.51	10.56	10.68	10.50	10.20	10.17
Na2O	5.36	5.33	5.68	5.25	5.57	5.55	5.98
K2O	0.32	0.30	0.34	0.34	0.37	0.34	0.32
FeO	0.25	0.38	0.42	0.39	0.40	0.42	0.38
Total	100.16	100.53	101.03	100.46	100.99	99.74	100.93
An	50.98	51.24	49.71	51.90	49.96	49.42	47.56
Ab	47.19	47.00	48.38	46.15	47.92	48.62	50.64
Or	1.83	1.75	1.91	1.94	2.11	1.96	1.79

	AC34	AC34	AC34	AC34	AC34	AC34	AC34
Host	**Aniak. I**	**Aniak. I**	**Aniak. I**	**Aniak. I**	**Aniak. I**	**Aniak. I**	**Aniak. I**
Line Numbers	**234**	**251**	**252**	**253**	**254**	**255**	**256**
SiO2	49.09	54.60	52.64	53.35	53.90	52.35	53.78
Al2O3	32.62	27.60	29.62	29.44	29.15	28.86	29.05
CaO	15.50	10.86	12.96	11.81	11.98	12.14	11.89
Na2O	2.53	5.50	4.32	4.63	4.73	4.47	4.78
K2O	0.12	0.30	0.19	0.20	0.22	0.28	0.27
FeO	0.79	0.61	0.71	0.80	0.64	0.71	0.61
Total	100.65	99.46	100.45	100.23	100.62	98.82	100.38
An	76.64	51.30	61.69	57.81	57.57	59.03	56.98
Ab	22.67	47.03	37.24	41.01	41.16	39.35	41.49
Or	0.69	1.67	1.08	1.18	1.27	1.62	1.53

	AC34	AC34	AC34	AC34	AC34	AC34	AC34
Host	**Aniak. I**	**Aniak. I**	**Aniak. I**	**Aniak. I**	**Aniak. I**	**Aniak. I**	**Aniak. I**
Line Numbers	**242**	**259**	**260**	**261**	**262**	**263**	**268**
SiO2	55.30	55.81	55.61	55.97	54.64	55.26	55.84
Al2O3	28.23	27.70	27.82	27.35	28.13	28.04	27.94
CaO	10.57	10.43	10.67	10.04	10.93	10.94	10.27
Na2O	5.49	5.56	5.38	6.00	5.42	5.27	5.89
K2O	0.27	0.38	0.36	0.38	0.35	0.30	0.34
FeO	0.54	0.59	0.37	0.33	0.61	0.72	0.50
Total	100.41	100.46	100.21	100.08	100.07	100.52	100.78
An	50.74	49.80	51.21	47.03	51.69	52.52	48.13
Ab	47.71	48.04	46.75	50.83	46.33	45.79	49.98
Or	1.56	2.17	2.04	2.14	1.97	1.69	1.88

Host	AC34 Aniak. I	AC34 Aniak. I	AC34 Aniak. I	AC34 Aniak. I	AC34 Aniak. I	AC34 Aniak. I	AC34 Aniak. I
Line Numbers	249	250	271	272	273	274	275
SiO2	56.20	55.60	55.74	56.76	55.70	54.41	55.39
Al2O3	27.74	28.25	27.39	27.09	27.59	28.51	27.81
CaO	10.14	9.97	10.63	9.77	10.76	11.27	10.74
Na2O	5.78	5.72	5.77	6.01	5.60	5.16	5.32
K2O	0.38	0.41	0.41	0.38	0.35	0.24	0.34
FeO	0.18	0.55	0.68	0.53	0.33	0.69	0.60
Total	100.42	100.50	100.62	100.55	100.33	100.27	100.21
An	48.20	47.93	49.29	46.30	50.49	53.94	51.69
Ab	49.67	49.74	48.44	51.57	47.56	44.71	46.37
Or	2.12	2.33	2.27	2.13	1.95	1.36	1.94

Host	AC34 Aniak. I	AC34 Aniak. I	AC34 Aniak. I	AC34 Aniak. I	AC34 Aniak. I	AC34 Aniak. I	AC34 Aniak. I
Line Numbers	257	258	279	280	281	282	283
SiO2	53.30	53.56	53.02	55.30	53.91	55.09	54.55
Al2O3	28.95	29.12	29.76	27.67	29.12	28.36	27.91
CaO	12.39	12.00	12.66	10.82	11.87	10.95	11.70
Na2O	4.72	4.83	4.22	5.58	4.86	5.15	5.11
K2O	0.26	0.22	0.21	0.33	0.24	0.34	0.32
FeO	0.65	0.57	0.60	0.60	0.51	0.27	0.52
Total	100.27	100.30	100.46	100.29	100.50	100.16	100.10
An	58.36	57.17	61.61	50.76	56.66	52.96	54.86
Ab	40.21	41.61	37.17	47.40	41.96	45.10	43.35
Or	1.43	1.23	1.22	1.84	1.38	1.94	1.79

Host	AC34 Aniak. I	AC34 Aniak. I	AC37A CFE RD	AC37A CFE RD	AC37A CFE RD	AC37A CFE RD	AC37A CFE RD
Line Numbers	269	270	288	289	290	291	292
SiO2	57.18	56.91	57.85	57.91	57.96	58.67	58.72
Al2O3	27.22	26.80	26.94	26.49	26.31	26.28	25.99
CaO	9.59	9.62	8.76	8.83	8.78	8.27	8.24
Na2O	6.27	6.27	6.68	6.73	6.69	6.80	6.75
K2O	0.40	0.44	0.32	0.33	0.27	0.33	0.31
FeO	0.59	0.26	0.47	0.34	0.34	0.31	0.29
Total	101.25	100.31	101.02	100.64	100.35	100.65	100.31
An	44.79	44.77	41.28	41.26	41.42	39.46	39.54
Ab	53.00	52.77	56.93	56.93	57.06	58.66	58.68
Or	2.21	2.46	1.79	1.81	1.52	1.88	1.78

Host	AC34 Aniak. I	AC34 Aniak. I	AC34 Aniak. I	AC37A CFE RD	AC37A CFE RD	AC37A CFE RD	AC37A CFE RD
Line Numbers	276	277	278	296	297	298	299
SiO2	55.09	56.40	55.63	58.83	58.39	58.78	58.24
Al2O3	28.00	27.23	27.52	26.29	26.37	25.89	26.51
CaO	11.32	9.71	10.09	8.33	8.35	7.90	8.37
Na2O	5.42	5.99	5.63	7.06	7.01	7.08	6.94
K2O	0.30	0.37	0.34	0.34	0.29	0.27	0.30
FeO	0.73	0.56	0.53	0.45	0.34	0.40	0.45
Total	100.85	100.25	99.75	101.29	100.74	100.32	100.82
An	52.68	46.28	48.79	38.72	39.04	37.57	39.32
Ab	45.69	51.63	49.24	59.42	59.37	60.90	59.00
Or	1.64	2.09	1.98	1.87	1.59	1.53	1.69

Host	AC37A CFE RD	AC37A CFE RD	AC37A CFE RD	AC37A CFE RD	AC37A CFE RD	AC37A CFE RD	AC37A CFE RD
Line Numbers	284	285	286	304	305	306	307
SiO2	59.74	58.19	58.15	54.64	55.84	55.64	61.62
Al2O3	24.20	25.50	26.50	28.48	28.02	28.57	24.57
CaO	7.55	8.12	8.66	11.11	9.89	10.95	7.21
Na2O	6.14	6.96	6.73	5.28	5.77	5.42	7.17
K2O	0.71	0.30	0.34	0.18	0.24	0.18	0.64
FeO	0.94	0.68	0.52	0.54	0.50	0.61	0.69
Total	99.28	99.75	100.92	100.24	100.24	101.37	101.89
An	38.71	38.53	40.75	53.20	48.00	52.19	34.41
Ab	56.97	59.76	57.33	45.76	50.64	46.78	61.98
Or	4.32	1.71	1.92	1.03	1.36	1.03	3.61

Host	AC37A CFE RD	AC37A CFE RD	AC37A CFE RD	AC37A CFE RD	AC37A CFE RD	AC37A CFE RD	AC37A CFE RD
Line Numbers	293	294	295	314	317	318	320
SiO2	58.77	57.79	58.75	58.63	59.91	57.33	58.32
Al2O3	26.03	26.37	26.48	26.17	25.68	26.70	26.59
CaO	7.93	8.26	8.01	7.33	6.83	8.21	8.63
Na2O	6.90	6.80	6.79	7.85	7.66	6.66	6.73
K2O	0.30	0.30	0.40	0.39	0.44	0.36	0.28
FeO	0.22	0.38	0.38	0.58	0.48	0.35	0.28
Total	100.15	99.90	100.81	100.95	101.00	99.62	100.82
An	38.19	39.50	38.54	33.29	32.20	39.67	40.83
Ab	60.09	58.80	59.18	64.57	65.34	58.24	57.61
Or	1.72	1.70	2.28	2.13	2.46	2.09	1.57

Host	AC37A CFE RD	AC37A CFE RD	AC37A CFE RD	AC37A CFE RD	94CNA04 HAB	94CNA04 HAB	94CNA04 HAB
Line Numbers	300	301	302	303	67	68	69
SiO2	56.06	55.46	55.23	58.78	48.16	43.99	50.29
Al2O3	27.70	28.22	28.10	26.34	31.59	34.54	30.94
CaO	10.12	10.83	10.31	7.96	16.21	19.40	14.45
Na2O	5.91	5.68	5.48	6.92	2.46	0.63	3.39
K2O	0.28	0.23	0.17	0.30	0.13	0.01	0.24
FeO	0.52	0.46	0.54	0.52	0.64	0.61	0.74
Total	100.59	100.89	99.84	100.83	99.18	99.18	100.05
An	47.84	50.65	50.47	38.18	0.78	0.94	0.69
Ab	50.56	48.05	48.52	60.09	0.21	0.06	0.29
Or	1.59	1.31	1.01	1.73	0.01	0.00	0.01

Host	AC37A CFE RD	AC37A CFE RD	AC37A CFE RD	AC37A CFE RD	94CNA04 HAB	94CNA04 HAB	94CNA04 HAB
Line Numbers	308	309	310	313	75	76	77
SiO2	61.25	61.12	60.11	58.57	46.20	47.77	47.75
Al2O3	24.14	24.65	24.95	26.33	32.74	32.11	31.41
CaO	5.95	6.07	6.88	7.98	17.22	16.23	15.65
Na2O	8.18	7.50	7.37	7.02	1.65	2.52	2.40
K2O	0.55	0.51	0.48	0.29	0.06	0.15	0.18
FeO	0.45	0.42	0.34	0.43	0.86	0.96	1.10
Total	100.52	100.26	100.13	100.62	98.73	99.73	98.50
An	27.82	29.97	33.09	37.96	0.85	0.77	0.77
Ab	69.14	67.02	64.18	60.42	0.15	0.22	0.21
Or	3.03	3.01	2.73	1.62	0.00	0.01	0.01

Host	94CNA04 HAB	94CNA04 HAB	94CNA04 HAB	94CNA04 HAB	94CNA04 HAB	94CNA04 HAB	94CNA04 HAB
Line Numbers	55	64	65	66	83	84	85
SiO2	46.66	47.98	47.54	47.50	44.30	49.74	49.43
Al2O3	32.91	31.67	32.49	31.67	33.82	30.11	30.81
CaO	17.43	15.88	16.33	16.10	18.22	14.32	14.54
Na2O	1.70	2.67	2.39	2.31	1.17	3.40	2.88
K2O	0.10	0.13	0.11	0.15	0.05	0.30	0.16
FeO	0.75	0.87	0.74	0.84	0.87	0.74	0.77
Total	99.56	99.20	99.59	98.57	98.43	98.62	98.58
An	0.84	0.76	0.79	0.79	0.89	0.69	0.73
Ab	0.15	0.23	0.21	0.20	0.10	0.30	0.26
Or	0.01	0.01	0.01	0.01	0.00	0.02	0.01

Host	94CNA04 HAB	94CNA04 HAB	94CNA04 HAB	94CNA04 HAB	94CNA04 HAB	94CNA04 HAB	94CNA04 HAB
Line Numbers	**70**	**71**	**72**	**73**	**74**	**91**	**92**
SiO2	47.88	50.47	48.82	50.29	51.05	44.84	47.00
Al2O3	32.45	30.43	30.59	30.58	30.04	34.71	32.21
CaO	16.12	13.92	15.15	14.56	13.37	19.29	16.38
Na2O	2.17	3.62	2.76	3.25	3.74	1.01	2.33
K2O	0.19	0.23	0.15	0.16	0.25	0.03	0.12
FeO	1.33	1.00	1.11	0.82	0.65	0.42	0.77
Total	100.14	99.66	98.59	99.66	99.10	100.29	98.81
An	0.79	0.67	0.75	0.71	0.65	0.91	0.79
Ab	0.19	0.32	0.25	0.29	0.33	0.09	0.20
Or	0.01	0.01	0.01	0.01	0.01	0.00	0.01

Host	94CNA04 HAB	94CNA04 HAB	94CNA04 HAB	94CNA04 HAB	94CNA04 HAB	94CNA05 HAB	94CNA05 HAB
Line Numbers	**78**	**79**	**80**	**81**	**82**	**99**	**100**
SiO2	49.53	50.06	48.73	49.96	49.61	52.59	51.81
Al2O3	31.05	31.02	31.34	30.36	31.03	28.91	28.38
CaO	14.41	14.70	15.42	14.12	14.69	13.53	12.91
Na2O	3.28	3.26	2.64	3.51	3.27	2.89	3.66
K2O	0.23	0.20	0.19	0.19	0.16	0.80	0.47
FeO	1.00	0.82	0.90	0.82	0.74	1.21	1.57
Total	99.50	100.05	99.23	98.96	99.50	99.93	98.80
An	0.70	0.71	0.75	0.68	0.71	0.69	0.64
Ab	0.29	0.28	0.23	0.31	0.28	0.27	0.33
Or	0.01	0.01	0.01	0.01	0.01	0.05	0.03

Host	94CNA04 HAB	94CNA04 HAB	94CNA04 HAB	94CNA04 HAB	94CNA04 HAB	94CNA05 HAB	94CNA05 HAB
Line Numbers	**86**	**87**	**88**	**89**	**90**	**107**	**108**
SiO2	48.01	43.84	48.15	43.96	45.78	53.99	48.98
Al2O3	32.67	34.49	31.73	34.63	34.23	27.83	31.90
CaO	16.66	19.50	16.18	19.04	17.97	11.41	16.04
Na2O	2.10	0.59	2.42	0.84	1.38	4.80	2.61
K2O	0.17	0.04	0.14	0.01	0.03	0.31	0.12
FeO	0.68	0.50	0.64	0.61	0.87	0.76	0.81
Total	100.28	98.96	99.26	99.09	100.26	99.11	100.46
An	0.81	0.95	0.78	0.93	0.88	0.56	0.77
Ab	0.18	0.05	0.21	0.07	0.12	0.42	0.23
Or	0.01	0.00	0.01	0.00	0.00	0.02	0.01

Host	94CNA04 HAB	94CNA04 HAB	94CNA05 HAB	94CNA05 HAB	94CNA05 HAB	94CNA05 HAB	94CNA05 HAB
Line Numbers	93	94	95	96	97	98	115
SiO2	49.20	49.11	51.31	53.62	49.34	46.93	50.44
Al2O3	31.24	31.41	29.66	28.43	31.48	32.55	28.10
CaO	15.46	15.34	13.79	12.13	15.14	17.14	13.72
Na2O	2.88	2.96	3.90	4.72	2.84	2.09	3.32
K2O	0.16	0.14	0.21	0.46	0.07	0.10	0.69
FeO	0.71	0.71	0.88	0.78	0.70	0.89	2.61
Total	99.65	99.67	99.75	100.14	99.58	99.71	98.88
An	0.74	0.74	0.65	0.57	0.74	0.81	0.67
Ab	0.25	0.26	0.33	0.40	0.25	0.18	0.29
Or	0.01	0.01	0.01	0.03	0.00	0.01	0.04

Host	94CNA05 HAB	94CNA05 HAB	94CNA05 HAB	94CNA05 HAB	94CNA05 HAB	94CNA05 HAB	94CNA05 HAB
Line Numbers	101	102	103	104	105	106	123
SiO2	52.33	46.51	52.37	49.38	48.61	51.10	49.65
Al2O3	29.61	33.31	28.88	29.76	31.39	29.95	30.63
CaO	13.57	17.59	12.77	14.69	15.96	14.41	14.91
Na2O	3.93	1.67	4.38	3.13	2.79	3.36	3.06
K2O	0.31	0.06	0.29	0.22	0.10	0.21	0.13
FeO	0.95	0.60	0.65	1.08	0.78	0.69	0.83
Total	100.70	99.74	99.35	98.26	99.62	99.71	99.20
An	0.64	0.85	0.61	0.71	0.76	0.69	0.72
Ab	0.34	0.15	0.38	0.27	0.24	0.29	0.27
Or	0.02	0.00	0.02	0.01	0.01	0.01	0.01

Host	94CNA05 HAB	94CNA05 HAB	94CNA05 HAB	94CNA05 HAB	94CNA05 HAB	94CNA05 HAB	92CNA22 HAB
Line Numbers	109	110	111	112	113	114	131
SiO2	48.71	51.33	48.55	53.74	47.35	54.89	45.41
Al2O3	29.12	29.81	31.88	28.05	32.97	23.55	34.06
CaO	15.05	13.91	15.91	11.73	17.19	10.98	18.23
Na2O	2.91	3.56	2.47	4.77	1.83	4.34	1.30
K2O	0.18	0.33	0.27	0.40	0.07	0.64	0.07
FeO	2.32	0.92	0.70	0.77	0.78	2.38	0.78
Total	98.29	99.86	99.78	99.46	100.19	96.80	99.84
An	0.73	0.67	0.77	0.56	0.84	0.56	0.88
Ab	0.26	0.31	0.22	0.41	0.16	0.40	0.11
Or	0.01	0.02	0.02	0.02	0.00	0.04	0.00

Host	94CNA05 HAB	94CNA05 HAB	94CNA05 HAB	94CNA05 HAB	94CNA05 HAB	94CNA05 HAB	94CNA05 HAB
Line Numbers	116	117	118	119	120	121	122
SiO2	51.91	49.83	53.56	54.12	52.80	48.22	51.77
Al2O3	25.32	27.52	28.31	27.75	28.79	26.85	28.75
CaO	13.17	14.39	12.34	12.18	12.50	13.86	13.66
Na2O	3.00	2.25	4.49	4.42	4.20	2.50	3.83
K2O	0.78	0.50	0.32	0.37	0.29	0.31	0.39
FeO	3.37	3.47	0.66	0.76	0.67	5.55	1.34
Total	97.55	97.97	99.68	99.59	99.25	97.28	99.73
An	0.67	0.76	0.59	0.59	0.61	0.74	0.65
Ab	0.28	0.21	0.39	0.39	0.37	0.24	0.33
Or	0.05	0.03	0.02	0.02	0.02	0.02	0.02

Host	94CNA05 HAB	94CNA05 HAB	94CNA05 HAB	94CNA05 HAB	94CNA05 HAB	94CNA05 HAB	94CNA05 HAB
Line Numbers	124	125	126	127	128	129	130
SiO2	53.53	49.59	50.78	53.50	52.89	47.42	53.13
Al2O3	28.64	28.55	29.44	28.64	29.05	32.42	24.07
CaO	12.59	14.94	14.25	12.28	12.43	16.85	11.13
Na2O	4.27	2.82	3.46	4.36	4.78	2.26	3.12
K2O	0.34	0.26	0.15	0.41	0.30	0.06	1.62
FeO	0.63	2.85	0.78	0.75	0.72	0.90	4.95
Total	100.00	99.00	98.87	99.95	100.17	99.91	98.03
An	0.61	0.73	0.69	0.59	0.58	0.80	0.59
Ab	0.37	0.25	0.30	0.38	0.40	0.19	0.30
Or	0.02	0.01	0.01	0.02	0.02	0.00	0.10

Host	92CNA22 HAB	92CNA22 HAB	92CNA22 HAB	92CNA22 HAB	92CNA22 HAB	92CNA22 HAB	92CNA22 HAB
Line Numbers	132	133	134	135	136	137	138
SiO2	46.93	46.86	46.13	45.12	48.54	46.50	46.44
Al2O3	33.63	33.55	33.97	34.22	31.93	33.35	33.15
CaO	17.55	17.90	18.08	17.98	16.40	17.71	17.52
Na2O	2.01	1.97	1.46	1.37	2.29	1.59	1.74
K2O	0.07	0.04	0.03	0.03	0.11	0.02	0.06
FeO	0.94	1.00	0.90	0.79	1.05	0.97	0.71
Total	101.14	101.33	100.57	99.52	100.33	100.14	99.63
An	0.82	0.83	0.87	0.88	0.79	0.86	0.84
Ab	0.17	0.17	0.13	0.12	0.20	0.14	0.15
Or	0.00	0.00	0.00	0.00	0.01	0.00	0.00

Host	92CNA22 HAB	92CNA22 HAB	92CNA22 HAB	92CNA22 HAB	92CNA22 HAB	92CNA22 HAB	92CNA22 HAB
Line Numbers	139	140	141	142	143	144	145
SiO2	44.97	46.21	46.73	45.52	45.57	47.86	47.41
Al2O3	35.10	34.14	33.19	34.13	34.10	33.05	31.83
CaO	19.40	17.90	17.24	18.27	18.35	16.74	16.82
Na2O	0.92	1.75	1.90	1.31	1.22	2.35	2.46
K2O	0.03	0.04	0.08	0.05	0.06	0.09	0.07
FeO	0.77	0.91	0.97	0.71	0.93	0.97	0.80
Total	101.19	100.95	100.11	99.99	100.23	101.06	99.39
An	0.92	0.85	0.83	0.88	0.89	0.79	0.79
Ab	0.08	0.15	0.17	0.11	0.11	0.20	0.21
Or	0.00	0.00	0.00	0.00	0.00	0.00	0.00

Host	92CNA22 HAB	92CNA22 HAB	92CNA22 HAB	92CNA22 HAB	92CNA22 HAB	92CNA22 HAB	92CNA22 HAB
Line Numbers	147	148	149	150	151	152	153
SiO2	47.36	48.41	49.66	46.57	46.76	47.18	45.95
Al2O3	33.17	32.39	30.74	32.69	33.76	33.77	34.29
CaO	17.13	16.00	14.88	16.92	17.57	17.61	18.38
Na2O	1.96	2.57	3.11	2.13	1.85	1.80	1.42
K2O	0.07	0.11	0.24	0.13	0.05	0.07	0.04
FeO	0.57	0.90	1.78	0.84	0.92	1.06	0.83
Total	100.26	100.37	100.41	99.28	100.91	101.49	100.92
An	0.82	0.77	0.72	0.81	0.84	0.84	0.88
Ab	0.17	0.22	0.27	0.18	0.16	0.16	0.12
Or	0.00	0.01	0.01	0.01	0.00	0.00	0.00

Host	92CNA22 HAB	92CNA22 HAB	92CNA22 HAB	92CNA22 HAB	92CNA22 HAB	92CNA22 HAB	92CNA22 HAB
Line Numbers	155	156	157	158	159	160	161
SiO2	47.53	46.27	45.69	47.23	47.54	46.85	47.27
Al2O3	32.76	33.62	34.53	33.34	33.25	34.22	33.26
CaO	16.85	17.84	18.14	17.26	16.84	17.41	16.91
Na2O	2.25	1.71	1.47	2.04	2.34	1.74	2.04
K2O	0.08	0.06	0.02	0.06	0.06	0.03	0.07
FeO	0.91	0.69	1.00	0.87	0.66	1.17	0.80
Total	100.38	100.20	100.85	100.80	100.68	101.42	100.36
An	0.80	0.85	0.87	0.82	0.80	0.85	0.82
Ab	0.19	0.15	0.13	0.18	0.20	0.15	0.18
Or	0.00	0.00	0.00	0.00	0.00	0.00	0.00

Host	92CNA22 HAB	92CNA22 HAB	92CNA22 HAB	92CNA22 HAB	99AC26 PreCald RD	99AC26 PreCald RD
Line Numbers	146	163	164	165	166	167
SiO2	45.62	46.50	52.27	45.40	58.25	58.41
Al2O3	35.10	33.22	29.92	34.47	25.96	25.61
CaO	18.50	17.62	12.90	18.43	8.14	7.89
Na2O	1.18	1.59	4.34	1.36	6.76	6.63
K2O	0.05	0.04	0.13	0.09	0.42	0.40
FeO	0.77	0.82	1.01	0.84	0.40	0.45
Total	101.22	99.79	100.56	100.59	99.94	99.39
An	0.89	0.86	0.62	0.88	0.39	0.39
Ab	0.10	0.14	0.38	0.12	0.59	0.59
Or	0.00	0.00	0.01	0.00	0.02	0.02

Host	92CNA22 HAB	99AC26 PreCald RD	99AC26 PreCald RD	99AC26 PreCald RD	99AC26 PreCald RD	99AC26 PreCald RD
Line Numbers	154	171	172	173	174	175
SiO2	45.16	59.65	58.75	57.82	58.54	58.24
Al2O3	34.79	24.62	25.44	26.25	25.69	25.50
CaO	18.64	6.90	8.12	8.64	7.74	7.93
Na2O	1.22	7.29	6.84	6.69	6.79	6.70
K2O	0.02	0.68	0.54	0.50	0.56	0.43
FeO	0.91	0.54	0.40	0.49	0.43	0.35
Total	100.74	99.69	100.10	100.38	99.75	99.15
An	0.89	0.33	0.38	0.40	0.37	0.39
Ab	0.11	0.63	0.59	0.57	0.59	0.59
Or	0.00	0.04	0.03	0.03	0.03	0.02

Host	92CNA22 HAB	99AC26 PreCald RD	99AC26 PreCald RD	99AC26 PreCald RD	99AC26 PreCald RD	99AC26 PreCald RD
Line Numbers	162	179	180	181	182	183
SiO2	47.06	59.38	58.47	59.35	75.33	57.20
Al2O3	33.32	25.11	25.45	25.42	11.77	25.55
CaO	16.92	7.56	7.99	7.50	0.66	8.71
Na2O	2.17	7.13	6.98	7.07	3.78	6.70
K2O	0.07	0.46	0.33	0.44	4.75	0.30
FeO	0.80	0.32	0.39	0.44	2.28	0.38
Total	100.35	99.96	99.61	100.22	98.59	98.85
An	0.81	0.36	0.38	0.36	0.05	0.41
Ab	0.19	0.61	0.60	0.61	0.52	0.57
Or	0.00	0.03	0.02	0.03	0.43	0.02

Host	99AC26 PreCald RD	99AC26 PreCald RD	99AC26 PreCald RD	99AC26 PreCald RD	99AC26 PreCald RD	99AC26 PreCald RD
Line Numbers	**168**	**169**	**170**	**187**	**188**	**189**
SiO2	60.38	58.48	58.46	58.06	57.50	58.36
Al2O3	24.48	25.63	25.73	26.26	26.39	25.38
CaO	6.84	8.59	8.42	8.47	8.65	8.29
Na2O	7.54	6.50	6.37	6.64	6.30	6.70
K2O	0.51	0.36	0.44	0.42	0.31	0.38
FeO	0.59	0.41	0.44	0.48	0.37	0.40
Total	100.33	99.97	99.87	100.34	99.53	99.52
An	0.32	0.41	0.41	0.40	0.42	0.40
Ab	0.65	0.57	0.56	0.57	0.56	0.58
Or	0.03	0.02	0.03	0.02	0.02	0.02

Host	99AC26 PreCald RD	99AC26 PreCald RD	99AC26 PreCald RD	99AC26 PreCald RD	99AC26 PreCald RD	99AC26 PreCald RD
Line Numbers	**176**	**177**	**178**	**195**	**196**	**197**
SiO2	59.30	58.02	57.54	57.63	58.78	58.32
Al2O3	25.22	26.08	26.53	25.62	25.60	25.27
CaO	7.33	8.69	9.17	8.22	7.79	8.45
Na2O	7.32	6.63	6.51	6.80	7.01	7.06
K2O	0.67	0.45	0.28	0.36	0.46	0.51
FeO	0.36	0.57	0.51	0.36	0.44	0.38
Total	100.21	100.43	100.54	98.99	100.08	99.99
An	0.34	0.41	0.43	0.39	0.37	0.39
Ab	0.62	0.57	0.55	0.59	0.60	0.59
Or	0.04	0.03	0.02	0.02	0.03	0.03

Host	99AC26 PreCald RD	99AC26 PreCald RD	99AC26 PreCald RD	97ANB45 PreCald RD	97ANB45 PreCald RD	97ANB45 PreCald RD
Line Numbers	**184**	**185**	**186**	**243**	**244**	**245**
SiO2	60.08	57.47	58.64	58.30	54.70	52.89
Al2O3	24.34	26.37	25.34	25.86	27.51	29.26
CaO	6.33	9.11	8.03	8.38	10.38	12.25
Na2O	7.51	6.36	6.64	6.76	5.56	4.63
K2O	0.71	0.43	0.53	0.46	0.21	0.20
FeO	0.58	0.45	0.37	0.71	0.55	0.69
Total	99.57	100.19	99.55	100.47	98.91	99.93
An	0.30	0.43	0.39	0.40	0.50	0.59
Ab	0.65	0.54	0.58	0.58	0.49	0.40
Or	0.04	0.02	0.03	0.03	0.01	0.01

Host	99AC26 PreCald RD	99AC26 PreCald RD	99AC26 PreCald RD	99AC26 PreCald RD	99AC26 PreCald RD	97ANB45 PreCald RD
Line Numbers	**190**	**191**	**192**	**193**	**194**	**251**
SiO2	58.24	59.16	59.61	58.15	57.50	53.21
Al2O3	25.54	25.17	24.67	25.84	26.07	28.94
CaO	8.61	7.84	7.36	8.22	8.58	12.42
Na2O	6.60	7.03	7.21	7.08	6.45	4.63
K2O	0.50	0.45	0.62	0.44	0.34	0.17
FeO	0.51	0.40	0.61	0.62	0.47	0.49
Total	100.01	100.05	100.08	100.35	99.41	99.85
An	0.41	0.37	0.35	0.38	0.42	0.59
Ab	0.56	0.60	0.62	0.59	0.56	0.40
Or	0.03	0.03	0.04	0.02	0.02	0.01

Host	99AC26 PreCald RD	99AC26 PreCald RD	99AC26 PreCald RD	97ANB45 PreCald RD	97ANB45 PreCald RD	97ANB45 PreCald RD
Line Numbers	**198**	**199**	**200**	**241**	**242**	**259**
SiO2	59.25	58.19	58.29	53.77	52.79	54.68
Al2O3	25.34	25.65	25.60	28.23	29.83	27.86
CaO	7.77	8.29	8.82	11.34	12.35	10.98
Na2O	6.83	6.39	6.43	4.76	4.50	5.20
K2O	0.53	0.38	0.34	0.17	0.11	0.23
FeO	0.47	0.49	0.56	0.55	0.47	0.65
Total	100.19	99.39	100.04	98.82	100.04	99.61
An	0.37	0.41	0.42	0.56	0.60	0.53
Ab	0.60	0.57	0.56	0.43	0.39	0.46
Or	0.03	0.02	0.02	0.01	0.01	0.01

Host	97ANB45 PreCald RD	97ANB45 PreCald RD	97ANB45 PreCald RD	97ANB45 PreCald RD	97ANB45 PreCald RD	97ANB45 PreCald RD
Line Numbers	**246**	**247**	**248**	**249**	**250**	**267**
SiO2	98.01	52.62	56.48	56.02	54.13	56.33
Al2O3	1.04	29.39	26.07	27.32	27.94	26.57
CaO	0.03	12.54	9.38	9.98	11.02	9.72
Na2O	0.55	4.56	6.06	6.13	5.29	5.94
K2O	0.00	0.16	0.28	0.19	0.25	0.28
FeO	0.04	0.54	0.47	0.49	0.62	0.61
Total	99.67	99.82	98.73	100.12	99.25	99.45
An	0.03	0.60	0.45	0.47	0.53	0.47
Ab	0.97	0.39	0.53	0.52	0.46	0.52
Or	0.00	0.01	0.02	0.01	0.01	0.02

Host	97ANB45 PreCald RD	97ANB45 PreCald RD	97ANB45 PreCald RD	97ANB45 PreCald RD	97ANB45 PreCald RD	97ANB45 PreCald RD
Line Numbers	**252**	**253**	**254**	**255**	**256**	**257**
SiO2	55.26	54.65	54.82	56.37	54.51	59.64
Al2O3	27.60	28.62	27.37	27.13	28.01	23.97
CaO	10.38	11.07	10.65	9.67	11.07	7.64
Na2O	5.34	5.44	5.44	6.01	5.16	6.27
K2O	0.18	0.18	0.21	0.27	0.23	0.67
FeO	0.39	0.41	0.55	0.34	0.63	0.83
Total	99.16	100.38	99.03	99.79	99.62	99.01
An	0.51	0.52	0.51	0.46	0.54	0.39
Ab	0.48	0.47	0.47	0.52	0.45	0.57
Or	0.01	0.01	0.01	0.02	0.01	0.04

Host	97ANB45 PreCald RD	97ANB45 PreCald RD	97ANB45 PreCald RD	97ANB45 PreCald RD	97ANB45 PreCald RD	97ANB45 PreCald RD
Line Numbers	**260**	**261**	**262**	**263**	**264**	**265**
SiO2	54.32	55.42	54.24	55.45	57.09	54.51
Al2O3	28.87	27.44	28.59	27.21	25.72	27.26
CaO	11.53	10.26	10.88	10.81	8.63	10.21
Na2O	5.05	5.62	5.30	5.31	6.33	5.63
K2O	0.18	0.23	0.23	0.21	0.34	0.30
FeO	0.45	0.43	0.48	0.48	0.66	0.33
Total	100.40	99.41	99.73	99.47	98.78	98.24
An	0.55	0.50	0.52	0.52	0.42	0.49
Ab	0.44	0.49	0.46	0.46	0.56	0.49
Or	0.01	0.01	0.01	0.01	0.02	0.02

Host	97ANB45 PreCald RD	97ANB45 PreCald RD	97ANB45 PreCald RD	97ANB45 PreCald RD	97ANB45 PreCald RD	97ANB45 PreCald RD
Line Numbers	**268**	**269**	**270**	**271**	**272**	**273**
SiO2	54.61	54.66	54.83	54.98	55.02	55.01
Al2O3	28.79	28.19	28.21	28.47	28.13	28.60
CaO	10.91	11.07	10.91	10.55	10.94	10.25
Na2O	5.38	5.37	5.48	5.60	5.38	5.77
K2O	0.23	0.19	0.25	0.25	0.18	0.23
FeO	0.60	0.54	0.64	0.60	0.48	0.43
Total	100.52	100.02	100.31	100.45	100.13	100.28
An	0.52	0.53	0.52	0.50	0.52	0.49
Ab	0.47	0.46	0.47	0.48	0.47	0.50
Or	0.01	0.01	0.01	0.01	0.01	0.01

Host	97ANB45 PreCald RD	97ANB45 PreCald RD	97ANB45 PreCald RD	97ANB45 PreCald RD	97ANB45 PreCald RD	97AC22 PreCald RD
Line Numbers	258	275	276	277	278	279
SiO2	56.33	54.64	51.74	55.47	54.52	55.68
Al2O3	26.73	28.76	30.89	28.21	28.65	26.93
CaO	9.27	11.36	12.91	10.43	10.79	9.62
Na2O	6.16	5.16	4.25	5.64	5.44	5.99
K2O	0.31	0.12	0.13	0.20	0.23	0.33
FeO	0.62	0.62	0.64	0.57	0.54	0.54
Total	99.42	100.65	100.57	100.51	100.16	99.09
An	0.45	0.54	0.62	0.50	0.52	0.46
Ab	0.54	0.45	0.37	0.49	0.47	0.52
Or	0.02	0.01	0.01	0.01	0.01	0.02

Host	97ANB45 PreCald RD	97AC22 PreCald RD	97AC22 PreCald RD	97AC22 PreCald RD	97AC22 PreCald RD	97AC22 PreCald RD
Line Numbers	266	283	284	285	286	287
SiO2	54.82	56.61	56.60	55.73	55.26	54.96
Al2O3	27.75	27.35	26.59	27.29	27.75	27.87
CaO	10.68	9.51	9.15	9.78	9.98	10.50
Na2O	5.59	6.13	5.80	5.85	5.57	5.70
K2O	0.23	0.28	0.29	0.33	0.31	0.25
FeO	0.69	0.45	0.57	0.51	0.52	0.40
Total	99.75	100.33	99.01	99.48	99.38	99.69
An	0.51	0.45	0.46	0.47	0.49	0.50
Ab	0.48	0.53	0.53	0.51	0.49	0.49
Or	0.01	0.02	0.02	0.02	0.02	0.01

Host	97ANB45 PreCald RD	97AC22 PreCald RD	97AC22 PreCald RD	97AC22 PreCald RD	97AC22 PreCald RD	97AC22 PreCald RD
Line Numbers	274	293	294	295	296	297
SiO2	56.62	56.01	55.62	55.47	56.69	54.67
Al2O3	27.16	27.69	27.21	27.77	26.75	27.63
CaO	9.19	10.26	9.59	10.65	9.31	10.48
Na2O	6.10	5.43	5.98	5.46	6.28	5.32
K2O	0.31	0.34	0.35	0.26	0.32	0.22
FeO	0.55	0.49	0.40	0.58	0.36	0.47
Total	99.94	100.23	99.17	100.19	99.71	98.79
An	0.45	0.50	0.46	0.51	0.44	0.51
Ab	0.54	0.48	0.52	0.47	0.54	0.47
Or	0.02	0.02	0.02	0.01	0.02	0.01

Host	97AC22 PreCald RD	97AC22 PreCald RD	97AC22 PreCald RD	97AC22 PreCald RD	97AC22 PreCald RD	97AC22 PreCald RD
Line Numbers	280	281	282	301	302	303
SiO2	57.30	57.12	53.27	54.19	56.60	56.90
Al2O3	26.87	26.13	29.01	27.82	26.64	26.89
CaO	9.12	8.16	11.69	11.33	9.31	8.99
Na2O	6.32	6.52	4.93	5.25	6.25	6.22
K2O	0.33	0.36	0.22	0.24	0.34	0.35
FeO	0.53	0.49	0.58	0.55	0.41	0.55
Total	100.47	98.79	99.70	99.38	99.55	99.90
An	0.44	0.40	0.56	0.54	0.44	0.44
Ab	0.55	0.58	0.43	0.45	0.54	0.54
Or	0.02	0.02	0.01	0.01	0.02	0.02

Host	97AC22 PreCald RD	97AC22 PreCald RD	97AC22 PreCald RD	97AC22 PreCald RD	97AC22 PreCald RD	97AC22 PreCald RD
Line Numbers	288	289	291	309	310	311
SiO2	54.98	55.45	70.89	56.73	55.10	56.58
Al2O3	27.40	27.44	15.68	26.50	27.18	26.69
CaO	10.33	9.51	2.05	9.06	9.96	9.15
Na2O	5.58	5.58	5.00	6.24	5.66	6.18
K2O	0.31	0.31	3.52	0.39	0.26	0.36
FeO	0.55	0.64	1.56	0.46	0.47	0.50
Total	99.16	98.94	98.69	99.39	98.62	99.45
An	0.50	0.48	0.13	0.44	0.49	0.44
Ab	0.49	0.51	0.59	0.54	0.50	0.54
Or	0.02	0.02	0.27	0.02	0.02	0.02

Host	97AC22 PreCald RD	97AC22 PreCald RD	97AC22 PreCald RD	97AC30 Aniak. I	97AC30 Aniak. I	97AC30 Aniak. I
Line Numbers	298	299	300	317	318	319
SiO2	55.53	55.42	54.99	49.86	55.08	51.29
Al2O3	28.00	27.48	27.92	30.97	27.85	29.02
CaO	10.38	10.06	10.29	14.68	10.90	13.05
Na2O	5.49	5.46	5.60	3.29	5.24	3.83
K2O	0.32	0.25	0.25	0.17	0.41	0.18
FeO	0.38	0.47	0.55	0.87	0.46	0.59
Total	100.10	99.14	99.61	99.84	99.94	97.96
An	0.50	0.50	0.50	0.70	0.52	0.65
Ab	0.48	0.49	0.49	0.29	0.45	0.34
Or	0.02	0.01	0.01	0.01	0.02	0.01

	97AC22	97AC22	97AC22	97AC22	97AC22	97AC30
Host	**PreCald RD**	**PreCald RD**	**PreCald RD**	**PreCald RD**	**PreCald RD**	**Aniak. I**
Line Numbers	**304**	**305**	**306**	**307**	**308**	**325**
SiO2	56.17	57.00	56.54	56.32	57.38	55.19
Al2O3	27.63	25.88	26.45	26.55	25.82	28.01
CaO	9.93	8.89	8.97	9.56	8.26	10.87
Na2O	5.76	6.19	5.95	6.04	6.55	5.33
K2O	0.27	0.36	0.28	0.31	0.55	0.34
FeO	0.44	0.37	0.42	0.61	0.55	0.50
Total	100.20	98.69	98.61	99.37	99.10	100.24
An	0.48	0.43	0.45	0.46	0.40	0.52
Ab	0.50	0.55	0.54	0.52	0.57	0.46
Or	0.02	0.02	0.02	0.02	0.03	0.02

	97AC22	97AC22	97AC22	97AC22	97AC30	97AC30
Host	**PreCald RD**	**PreCald RD**	**PreCald RD**	**PreCald RD**	**Aniak. I**	**Aniak. I**
Line Numbers	**312**	**313**	**314**	**315**	**316**	**333**
SiO2	56.56	58.37	57.84	56.28	55.32	49.83
Al2O3	26.64	26.03	26.35	25.94	27.47	31.12
CaO	9.28	8.41	8.41	8.86	10.50	14.87
Na2O	5.89	6.41	6.20	6.01	5.47	3.28
K2O	0.32	0.38	0.29	0.39	0.39	0.16
FeO	0.52	0.53	0.33	0.50	0.41	1.02
Total	99.21	100.13	99.43	97.98	99.56	100.27
An	0.46	0.41	0.42	0.44	0.50	0.71
Ab	0.52	0.57	0.56	0.54	0.47	0.28
Or	0.02	0.02	0.02	0.02	0.02	0.01

	97AC30	97AC30	97AC30	97AC30	97AC30	97AC30
Host	**Aniak. I**	**Aniak. I**	**Aniak. I**	**Aniak. I**	**Aniak. I**	**Aniak. I**
Line Numbers	**320**	**321**	**322**	**323**	**324**	**341**
SiO2	56.76	54.13	53.80	54.58	56.89	55.26
Al2O3	26.03	28.44	28.82	28.52	25.63	27.68
CaO	8.64	11.07	12.09	11.31	9.00	10.51
Na2O	6.07	5.15	4.50	4.94	5.53	5.47
K2O	0.70	0.32	0.25	0.30	0.65	0.34
FeO	0.48	0.35	0.42	0.54	0.78	0.59
Total	98.68	99.47	99.88	100.17	98.49	99.85
An	0.42	0.53	0.59	0.55	0.46	0.50
Ab	0.54	0.45	0.40	0.43	0.51	0.48
Or	0.04	0.02	0.01	0.02	0.04	0.02

	97AC30	97AC30	97AC30	97AC30	97AC30	97AC30	97AC30
Host	**Aniak. I**	**Aniak. I**	**Aniak. I**	**Aniak. I**	**Aniak. I**	**Aniak. I**	**Aniak. I**
Line Numbers	**326**	**327**	**328**	**329**	**330**	**331**	**332**
SiO2	54.80	54.97	54.02	55.65	54.94	55.48	98.04
Al2O3	27.21	27.62	28.18	27.68	27.85	27.74	0.82
CaO	10.00	10.38	10.62	10.20	10.69	10.09	0.01
Na2O	5.46	5.38	5.12	5.48	5.38	5.71	0.38
K2O	0.39	0.33	0.32	0.42	0.29	0.34	0.30
FeO	0.48	0.46	0.33	0.57	0.33	0.59	0.20
Total	98.34	99.14	98.60	99.99	99.48	99.96	99.76
An	0.49	0.51	0.52	0.49	0.51	0.48	0.01
Ab	0.49	0.47	0.46	0.48	0.47	0.50	0.65
Or	0.02	0.02	0.02	0.02	0.02	0.02	0.34

	97AC30	97AC30	97AC30	97AC30	97AC30	97AC30	97AC30
Host	**Aniak. I**	**Aniak. I**	**Aniak. I**	**Aniak. I**	**Aniak. I**	**Aniak. I**	**Aniak. I**
Line Numbers	**334**	**335**	**336**	**337**	**338**	**339**	**340**
SiO2	54.76	52.84	55.09	52.73	55.42	54.67	55.01
Al2O3	27.50	29.32	27.76	29.15	27.18	27.18	28.14
CaO	10.38	12.64	10.58	12.47	10.29	10.99	10.85
Na2O	5.49	4.29	5.54	4.43	5.41	5.37	5.34
K2O	0.37	0.26	0.34	0.22	0.39	0.32	0.34
FeO	0.51	0.65	0.43	0.43	0.58	0.51	0.37
Total	99.02	100.00	99.74	99.43	99.27	99.04	100.04
An	0.50	0.61	0.50	0.60	0.50	0.52	0.52
Ab	0.48	0.37	0.48	0.39	0.48	0.46	0.46
Or	0.02	0.02	0.02	0.01	0.02	0.02	0.02

	97AC30	97AC30	97AC30	97AC30	97AC30	97AC30	97AC30
Host	**Aniak. I**	**Aniak. I**	**Aniak. I**	**Aniak. I**	**Aniak. I**	**Aniak. I**	**Aniak. I**
Line Numbers	**342**	**343**	**344**	**345**	**346**	**347**	**348**
SiO2	55.94	53.55	55.20	55.43	55.91	55.74	54.57
Al2O3	26.94	28.48	27.21	27.14	27.12	27.53	27.86
CaO	9.43	11.89	10.22	10.14	9.92	9.83	10.56
Na2O	5.69	4.74	5.48	5.67	5.63	5.69	5.56
K2O	0.42	0.31	0.50	0.46	0.46	0.41	0.37
FeO	0.52	0.40	0.42	0.53	0.35	0.48	0.42
Total	98.94	99.39	99.04	99.37	99.39	99.69	99.33
An	0.47	0.57	0.49	0.48	0.48	0.48	0.50
Ab	0.51	0.41	0.48	0.49	0.49	0.50	0.48
Or	0.02	0.02	0.03	0.03	0.03	0.02	0.02

	97AC30	97AC30	97AC30	97AC30	97AC30	97AC30	97AC33
Host	**Aniak. I**	**Aniak. I**	**Aniak. I**	**Aniak. I**	**Aniak. I**	**Aniak. I**	**Aniak. I**
Line Numbers	**349**	**350**	**351**	**352**	**353**	**354**	**355**
SiO2	55.02	53.26	54.34	54.62	50.57	54.48	55.41
Al2O3	27.41	27.82	28.02	28.45	30.06	27.79	27.39
CaO	10.39	11.41	10.90	10.99	13.94	10.77	10.61
Na2O	5.57	4.89	5.28	5.19	3.68	5.57	5.23
K2O	0.30	0.34	0.30	0.33	0.27	0.33	0.37
FeO	0.53	0.55	0.49	0.46	0.55	0.42	0.52
Total	99.23	98.28	99.34	100.03	99.07	99.36	99.53
An	0.50	0.55	0.52	0.53	0.67	0.51	0.52
Ab	0.48	0.43	0.46	0.45	0.32	0.47	0.46
Or	0.02	0.02	0.02	0.02	0.02	0.02	0.02

	97AC33	97AC33	97AC33	97AC33	97AC33	97AC33	97AC33
Host	**Aniak. I**	**Aniak. I**	**Aniak. I**	**Aniak. I**	**Aniak. I**	**Aniak. I**	**Aniak. I**
Line Numbers	**357**	**358**	**359**	**361**	**362**	**363**	**364**
SiO2	55.08	55.20	56.03	54.65	55.31	55.11	53.91
Al2O3	27.41	27.54	27.50	27.38	27.52	27.08	28.02
CaO	10.76	10.74	10.17	10.29	10.91	10.45	11.87
Na2O	5.41	5.34	5.82	5.36	5.10	5.53	4.78
K2O	0.31	0.30	0.42	0.31	0.25	0.34	0.27
FeO	0.43	0.54	0.41	0.38	0.48	0.50	0.55
Total	99.39	99.66	100.34	98.37	99.58	99.00	99.41
An	0.51	0.52	0.48	0.51	0.53	0.50	0.57
Ab	0.47	0.47	0.50	0.48	0.45	0.48	0.42
Or	0.02	0.02	0.02	0.02	0.01	0.02	0.02

	97AC33	97AC33	97AC33	97AC33	97AC33	97AC33	97AC33
Host	**Aniak. I**	**Aniak. I**	**Aniak. I**	**Aniak. I**	**Aniak. I**	**Aniak. I**	**Aniak. I**
Line Numbers	**367**	**368**	**369**	**370**	**371**	**372**	**373**
SiO2	54.45	55.11	54.99	54.39	54.59	54.82	54.79
Al2O3	27.71	27.31	28.00	28.47	27.55	28.00	27.83
CaO	10.97	10.92	11.03	11.21	10.60	11.13	10.80
Na2O	5.18	4.92	5.18	4.99	5.47	5.04	5.34
K2O	0.29	0.31	0.37	0.31	0.29	0.27	0.29
FeO	0.47	0.38	0.36	0.61	0.44	0.48	0.41
Total	99.07	98.94	99.92	99.98	98.93	99.74	99.46
An	0.53	0.54	0.53	0.54	0.51	0.54	0.52
Ab	0.45	0.44	0.45	0.44	0.48	0.44	0.46
Or	0.02	0.02	0.02	0.02	0.02	0.02	0.02

Host	97AC33 Aniak. I	97AC33 Aniak. I	97AC33 Aniak. I	97AC33 Aniak. I	97AC33 Aniak. I	97AC33 Aniak. I
Line Numbers	356	375	376	377	378	379
SiO2	56.15	54.54	52.05	55.92	56.24	55.65
Al2O3	26.98	27.14	29.69	27.22	27.34	27.49
CaO	9.95	11.17	13.39	10.32	10.26	10.41
Na2O	5.61	5.33	3.98	5.35	5.58	5.32
K2O	0.35	0.28	0.32	0.35	0.33	0.36
FeO	0.42	0.60	0.40	0.44	0.48	0.32
Total	99.47	99.06	99.83	99.60	100.22	99.55
An	0.49	0.53	0.64	0.51	0.49	0.51
Ab	0.49	0.46	0.34	0.47	0.49	0.47
Or	0.02	0.02	0.02	0.02	0.02	0.02

Host	97AC33 Aniak. I	97AC33 Aniak. I	97AC33 Aniak. I	97AC33 Aniak. I	97AC33 Aniak. I	97AC33 Aniak. I
Line Numbers	366	380	381	382	383	384
SiO2	54.89	55.95	55.41	53.61	56.47	55.95
Al2O3	27.54	27.52	27.13	28.71	26.95	27.03
CaO	11.11	10.40	10.34	11.75	9.62	10.27
Na2O	5.28	5.53	5.68	4.82	6.01	5.58
K2O	0.37	0.31	0.31	0.23	0.47	0.35
FeO	0.48	0.41	0.51	0.51	0.44	0.42
Total	99.67	100.13	99.39	99.64	99.97	99.60
An	0.53	0.50	0.49	0.57	0.46	0.49
Ab	0.45	0.48	0.49	0.42	0.52	0.49
Or	0.02	0.02	0.02	0.01	0.03	0.02

Host	97AC33 Aniak. I	97AC33 Aniak. I	97AC33 Aniak. I	97AC33 Aniak. I	97AC33 Aniak. I
Line Numbers	374	385	386	388	389
SiO2	55.47	54.19	55.35	54.57	54.06
Al2O3	27.30	28.20	27.79	27.88	29.03
CaO	10.23	11.07	10.80	10.57	11.89
Na2O	5.42	4.95	5.46	5.43	4.63
K2O	0.34	0.29	0.32	0.32	0.31
FeO	0.41	0.48	0.55	0.41	0.77
Total	99.17	99.18	100.27	99.18	100.69
An	0.50	0.54	0.51	0.51	0.58
Ab	0.48	0.44	0.47	0.47	0.41
Or	0.02	0.02	0.02	0.02	0.02

Appendix C: Pyroxene Analyses

Analyses were obtained using a Cameca SX-50 electron microprobe at the University of Alaska Fairbanks. Analytical conditions were 15 keV accelerating voltage, 10 na beam current, and a 10 μm spot size. Peak and background measurements were made for 10 seconds each. "Line number" refers to the analysis number in a particular microprobe session. "Host" refers to the rock type containing the analyzed sample. **CFE and** – caldera forming eruption andesite; **CFE RD** - caldera forming eruption rhyodacite; **L. Bk. Nose** – lower Black Nose pumice; **U. Bk. Nose** – upper Black Nose pumice; **Aniak. I** – Aniakchak I andesite; **HAB** – precaldera high-alumina basalt; **PreCald RD** – precaldera rhyodacite lava.

Host	ACAF1B1 CFE RD	ACAF1B1 CFE RD	ACAF1B1 CFE RD	ACAF1B1 CFE RD	ACAF1A8 CFE RD	ACAF1A8 CFE RD
Line Number	171.00	226.00	243.00	300.00	331.00	339.00
SiO2	51.96	53.16	53.59	53.45	52.67	52.69
TiO2	0.26	0.26	0.45	0.13	0.19	0.22
Al2O3	0.49	0.58	0.48	0.32	0.81	0.68
Fe2O3	1.12	0.00	0.00	0.00	0.00	0.00
FeO	20.58	19.85	20.08	20.14	20.47	19.77
MnO	1.92	1.91	1.84	2.28	2.20	1.87
MgO	21.25	22.06	22.69	22.11	21.41	21.59
CaO	1.45	1.31	1.39	1.40	1.38	1.70
Na2O	0.00	0.02	0.05	0.00	0.00	0.03
K20	0.04	0.00	0.00	0.02	0.04	0.04
Total	99.06	99.16	100.57	99.85	99.16	98.59
Mg#	64.80	66.46	66.82	66.19	65.08	66.06

Host	ACAF1A8 CFE RD	ACAF1A8 CFE RD	99AC26 PreCald RD	99AC26 PreCald RD	99AC26 PreCald RD	99AC26 PreCald RD
Line Number	365.00	413.00	836.00	852.00	858.00	862.00
SiO2	52.49	53.05	50.89	51.75	51.68	52.76
TiO2	0.22	0.24	0.26	0.42	0.22	0.22
Al2O3	0.34	0.31	0.72	0.71	0.56	0.72
Fe2O3	0.35	0.00	2.70	2.31	2.19	1.85
FeO	20.02	20.00	21.27	20.14	21.85	19.58
MnO	2.10	1.82	1.57	1.39	1.57	1.79
MgO	21.71	21.20	20.07	21.53	20.26	21.94
CaO	1.49	1.25	1.81	1.68	1.61	2.02
Na2O	0.05	0.05	0.04	0.04	0.06	0.03
K20	0.00	0.00	0.00	0.01	0.04	0.02
Total	98.77	97.93	99.33	99.98	100.05	100.93
Mg#	65.90	65.39	0.61	0.64	0.61	0.66

Host	99AC26 PreCald RD	ACAF1A8 CFE RD	99AC26 PreCald RD	99AC26 PreCald RD	99AC26 PreCald RD	99AC26 PreCald RD
Line Number	873.00	350.00	878.00	884.00	885.00	889.00
SiO2	52.39	53.13	52.01	51.94	52.45	51.97
TiO2	0.09	0.13	0.16	0.20	0.33	0.16
Al2O3	0.60	0.52	0.48	0.61	0.51	1.26
Fe2O3	2.85	0.00	3.61	3.65	3.96	2.02
FeO	22.35	20.70	20.33	20.95	20.93	13.33
MnO	1.67	1.92	1.70	1.65	1.50	0.89
MgO	20.41	21.32	21.59	21.02	21.47	15.08
CaO	1.70	1.25	1.45	1.68	1.65	15.57
Na2O	0.03	0.02	0.00	0.00	0.05	0.27
K20	0.00	0.04	0.00	0.03	0.01	0.00
Total	102.10	99.04	101.32	101.76	102.85	100.55
Mg#	0.61	64.73	0.64	0.62	0.63	0.65

Host	99AC26 PreCald RD	99AC26 PreCald RD	99AC26 PreCald RD	99AC26 PreCald RD	97ANB45 PreCald RD	97ANB45 PreCald RD
Line Number	907.00	918.00	934.00	944.00	667.00	668.00
SiO2	51.93	51.99	52.96	52.43	52.53	51.96
TiO2	0.20	0.20	0.19	0.28	0.17	0.34
Al2O3	0.47	0.62	0.42	0.68	0.72	1.58
Fe2O3	2.24	2.00	0.25	2.28	1.94	3.98
FeO	20.95	21.44	23.31	21.67	18.64	13.06
MnO	1.25	1.53	1.31	1.54	1.16	0.88
MgO	21.16	20.79	20.51	20.90	23.08	23.99
CaO	1.60	1.69	1.68	1.68	1.41	4.13
Na2O	0.06	0.03	0.02	0.06	0.05	0.10
K20	0.00	0.00	0.01	0.02	0.00	0.01
Total	99.87	100.30	100.67	101.54	99.70	100.04
Mg#	0.63	0.62	0.61	0.62	0.68	0.74

Host	99AC26 PreCald RD	97ANB45 PreCald RD	97ANB45 PreCald RD	97ANB45 PreCald RD	97ANB45 PreCald RD	97ANB45 PreCald RD
Line Number	898.00	676.00	677.00	678.00	684.00	685.00
SiO2	51.23	53.20	53.30	52.43	51.97	52.05
TiO2	0.25	0.11	0.22	0.13	0.34	0.20
Al2O3	0.66	0.52	0.63	0.64	1.00	0.74
Fe2O3	3.11	3.73	2.07	3.18	2.20	3.44
FeO	21.84	16.59	17.20	16.06	21.02	20.23
MnO	1.56	1.37	1.08	0.95	1.37	1.39
MgO	20.08	24.52	24.52	23.89	21.10	21.93
CaO	1.63	1.46	1.38	2.30	1.73	1.37
Na2O	0.05	0.05	0.03	0.05	0.05	0.00
K20	0.00	0.00	0.02	0.02	0.00	0.00
Total	100.40	101.54	100.45	99.65	100.78	101.35
Mg#	0.61	0.71	0.71	0.71	0.63	0.64

Host	97ANB45 PreCald RD	97ANB45 PreCald RD	97ANB45 PreCald RD	97ANB45 PreCald RD	97ANB45 PreCald RD	97ANB45 PreCald RD
Line Number	671.00	699.00	710.00	729.00	773.00	804.00
SiO2	52.12	49.99	53.49	54.27	53.15	52.99
TiO2	0.34	0.86	0.21	0.24	0.33	0.41
Al2O3	1.33	3.12	1.20	1.84	0.97	1.21
Fe2O3	2.68	3.53	1.81	0.58	1.82	2.47
FeO	11.47	8.35	16.51	17.73	17.11	17.62
MnO	0.89	0.89	0.80	1.11	0.88	1.19
MgO	19.70	14.57	25.18	23.52	24.63	24.07
CaO	11.26	18.61	1.49	1.43	1.42	1.50
Na2O	0.15	0.33	0.00	0.45	0.03	0.03
K20	0.01	0.00	0.01	0.13	0.01	0.00
Total	99.94	100.25	100.70	101.30	100.35	101.48
Mg#	0.73	0.72	0.72	0.70	0.71	0.70

Host	97ANB45 PreCald RD	97ANB45 PreCald RD	97ANB45 PreCald RD	97ANB45 PreCald RD	97AC22 PreCald RD	97AC22 PreCald RD
Line Number	690.00	694.00	813.00	831.00	958.00	979.00
SiO2	52.74	53.22	53.45	53.01	52.44	52.74
TiO2	0.20	0.27	0.24	0.30	0.28	0.08
Al2O3	0.57	0.55	1.79	0.95	0.98	0.71
Fe2O3	0.98	2.47	3.54	2.32	3.31	3.12
FeO	22.31	16.73	14.10	18.92	17.31	18.43
MnO	1.42	1.20	0.59	1.22	1.04	1.39
MgO	21.20	24.78	26.52	23.24	23.88	23.20
CaO	1.33	1.34	1.58	1.51	1.58	1.44
Na2O	0.00	0.02	0.03	0.02	0.00	0.03
K20	0.00	0.00	0.02	0.02	0.01	0.00
Total	100.76	100.57	101.84	101.52	100.84	101.14
Mg#	0.62	0.71	0.75	0.67	0.69	0.68

Host	97ANB45 PreCald RD	97AC22 PreCald RD	97AC22 PreCald RD	97AC22 PreCald RD	97AC22 PreCald RD	97AC22 PreCald RD
Line Number	805.00	1011.00	1028.00	1031.00	985.00	993.00
SiO2	52.06	53.04	52.94	52.38	52.94	52.25
TiO2	0.41	0.28	0.22	0.24	0.22	0.13
Al2O3	1.52	0.64	0.77	0.84	0.60	0.49
Fe2O3	4.20	1.69	1.72	2.27	2.02	4.38
FeO	16.13	18.34	19.13	18.31	17.59	14.77
MnO	1.21	1.37	1.25	1.35	1.27	1.14
MgO	24.20	23.60	23.07	22.77	23.66	23.66
CaO	1.46	1.45	1.41	1.57	1.74	3.26
Na2O	0.05	0.00	0.03	0.09	0.05	0.08
K20	0.04	0.01	0.02	0.05	0.00	0.01
Total	101.28	100.44	100.55	99.88	100.07	100.16
Mg#	0.71	0.69	0.67	0.68	0.70	0.72

Host	97AC22 PreCald RD	97AC22 PreCald RD	97AC22 PreCald RD	97AC22 PreCald RD	97AC22 PreCald RD	97AC22 PreCald RD
Line Number	998.00	1055.00	1065.00	1079.00	1036.00	1050.00
SiO2	53.29	52.26	51.51	52.99	52.51	52.80
TiO2	0.33	0.22	0.52	0.19	0.44	0.31
Al2O3	0.78	0.85	1.60	0.68	1.03	0.68
Fe2O3	2.16	1.97	2.89	3.29	2.98	2.61
FeO	18.21	19.57	17.68	17.57	18.34	20.28
MnO	1.19	1.33	0.88	1.29	1.21	1.46
MgO	23.89	22.35	22.67	23.88	23.07	22.30
CaO	1.50	1.50	2.28	1.53	1.79	1.44
Na2O	0.02	0.00	0.04	0.04	0.03	0.00
K20	0.01	0.01	0.00	0.00	0.03	0.03
Total	101.37	100.06	100.06	101.47	101.43	101.93
Mg#	0.69	0.66	0.68	0.69	0.68	0.65

Host	97AC22 PreCald RD	97AC22 PreCald RD	97AC22 PreCald RD	97AC22 PreCald RD	97AC22 PreCald RD	97AC19 U. Bk. Nose
Line Number	1051.00	1083.00	1084.00	1080.00	1082.00	1559.00
SiO2	52.70	52.48	52.94	53.07	52.95	51.90
TiO2	0.24	0.24	0.28	0.17	0.31	0.28
Al2O3	1.00	0.60	0.69	0.63	0.75	0.54
Fe2O3	2.83	2.34	1.63	2.13	2.40	1.37
FeO	18.32	18.83	18.88	18.71	18.12	21.68
MnO	1.52	1.40	1.10	1.40	1.16	1.72
MgO	22.94	22.29	22.99	23.14	23.74	20.57
CaO	1.86	2.07	1.90	1.53	1.49	1.54
Na2O	0.02	0.07	0.02	0.05	0.02	0.05
K20	0.01	0.00	0.02	0.02	0.00	0.01
Total	101.44	100.33	100.45	100.85	100.95	99.66
Mg#	0.68	0.67	0.68	0.68	0.69	0.62

	97AC19	97AC19	97AC19	97AC19	97AC19	97AC30
Host	**U. Bk. Nose**	**U. Bk. Nose**	**U. Bk. Nose**	**U. Bk. Nose**	**U. Bk. Nose**	**Aniakchak I**
Line Number	1581.00	1596.00	1585.00	1574.00	1579.00	1311.00
SiO2	51.69	52.11	51.85	51.98	52.47	50.83
TiO2	0.35	0.28	0.37	0.37	0.20	0.17
Al2O3	0.55	0.54	0.68	0.61	0.55	0.29
Fe2O3	2.35	1.76	1.07	2.35	1.08	2.58
FeO	20.70	20.77	21.57	19.76	20.89	28.10
MnO	1.48	1.57	1.35	1.44	1.73	1.28
MgO	21.21	21.27	20.65	21.88	21.45	16.32
CaO	1.66	1.63	1.47	1.56	1.51	1.74
Na2O	0.01	0.05	0.12	0.05	0.02	0.04
K20	0.00	0.00	0.05	0.02	0.00	0.01
Total	99.98	99.97	99.18	100.03	99.91	101.35
Mg#	0.63	0.64	0.63	0.65	0.64	0.50

	97AC30	97AC30	97AC30	97AC30	97AC30	97AC30
Host	**Aniakchak I**	**Aniakchak I**	**Aniakchak I**	**Aniakchak I**	**Aniakchak I**	**Aniakchak I**
Line Number	1337.00	1350.00	1358.00	1362.00	1314.00	1329.00
SiO2	52.68	51.28	51.11	52.50	50.14	52.49
TiO2	0.60	0.33	0.22	0.41	0.09	0.62
Al2O3	1.23	0.79	0.32	0.77	0.35	1.16
Fe2O3	1.89	2.35	2.39	1.28	1.90	3.01
FeO	18.14	23.40	28.02	21.82	28.47	18.46
MnO	0.74	0.88	1.03	0.79	1.24	0.61
MgO	23.72	19.43	16.54	21.41	14.51	23.45
CaO	1.85	1.95	1.78	1.80	3.31	1.82
Na2O	0.00	0.05	0.07	0.00	0.05	0.03
K20	0.00	0.00	0.06	0.02	0.00	0.00
Total	100.85	100.46	101.55	100.81	100.05	101.65
Mg#	0.69	0.59	0.50	0.63	0.47	0.68

	97AC30	97AC30	97AC33	97AC33	97AC30	97AC30
Host	**Aniakchak I**	**Aniakchak I**	**Aniakchak I**	**Aniakchak I**	**Aniakchak I**	**Aniakchak I**
Line Number	1408.00	1434.00	1456.00	1475.00	1370.00	1384.00
SiO2	52.75	50.94	52.32	51.11	51.21	51.62
TiO2	0.47	0.20	0.35	0.06	0.29	0.30
Al2O3	0.88	0.61	0.86	0.98	0.56	0.62
Fe2O3	2.91	1.58	3.12	3.36	2.65	2.47
FeO	18.90	25.61	19.87	25.01	25.43	23.12
MnO	1.04	1.03	1.04	1.05	0.85	0.91
MgO	23.00	17.85	21.83	18.27	18.34	19.88
CaO	1.80	1.90	2.33	1.88	1.94	1.85
Na2O	0.05	0.03	0.02	0.03	0.00	0.03
K20	0.02	0.02	0.00	0.00	0.03	0.00
Total	101.80	99.76	101.74	101.74	101.29	100.82
Mg#	0.67	0.55	0.65	0.55	0.55	0.59

	97AC33	97AC33	97AC33	97AC33	97AC33
Host	**Aniakchak I**	**Aniakchak I**	**Aniakchak I**	**Aniakchak I**	**Aniakchak I**
Line Number	1512.00	1513.00	1524.00	1551.00	1490.00
SiO2	53.07	51.56	51.15	51.50	52.67
TiO2	0.30	0.28	0.17	0.59	0.13
Al2O3	0.97	0.70	0.55	0.75	1.35
Fe2O3	2.20	1.87	2.11	1.97	1.75
FeO	18.73	23.63	25.09	24.70	20.36
MnO	0.97	1.03	1.06	1.21	1.05
MgO	23.22	19.47	18.40	18.95	21.08
CaO	1.76	1.86	1.77	1.86	2.27
Na2O	0.07	0.03	0.02	0.01	0.21
K20	0.02	0.00	0.00	0.00	0.08
Total	101.32	100.44	100.31	101.54	100.95
Mg#	0.68	0.59	0.56	0.57	0.64

Appendix D: Iron – Titanium Oxide Analyses

Analyses were obtained using a Cameca SX-50 electron microprobe at the University of Alaska Fairbanks. Analytical conditions were 15 keV accelerating voltage, 10 na beam current, and a 10 μm spot size. Peak and background measurements were made for 10 seconds each. "Line number" refers to the analysis number in a particular microprobe session. "Host" refers to the rock type containing the analyzed sample. **CFE and** – caldera forming eruption andesite; **CFE RD** - caldera forming eruption rhyodacite; **L. Bk. Nose** – lower Black Nose pumice; **U. Bk. Nose** – upper Black Nose pumice; **Aniak. I** – Aniakchak I andesite; **HAB** – precaldera high-alumina basalt; **PreCald RD** – precaldera rhyodacite lava.

Sample ID	99AC26 ilm 1	99AC26 mt 1	99AC26 ilm 3	99AC26 mt 3	99AC26 ilm 8	99AC26 mt 8
Host	**PreCald RD**	**PreCald RD**	**PreCald RD**	**PreCald RD**	**PreCald RD**	**PreCald RD**
SiO2	0.18	0.20	0.13	0.17	0.05	0.11
TiO2	47.69	19.77	48.11	23.69	47.03	19.97
Al2O3	0.11	1.98	0.12	1.48	0.14	1.73
Cr2O3	0.01	0.04	0.00	0.05	0.00	0.09
Fe2O3	9.57	28.38	9.36	21.93	10.20	27.80
FeO	38.66	47.12	38.74	50.71	37.44	46.74
MnO	1.18	0.94	1.19	1.02	1.34	1.09
MgO	1.83	1.21	1.95	1.23	2.00	1.19
Total	99.24	99.65	99.60	100.28	98.21	98.72

Sample ID	97ANB45 ilm 6	97ANB45 mt 6	AC22 ilm 1	AC22 mt 1	AC22 ilm 2	AC22 mt 2
Host	**PreCald RD**	**PreCald RD**	**PreCald RD**	**PreCald RD**	**PreCald RD**	**PreCald RD**
SiO2	0.03	0.05	0.03	0.14	0.00	0.17
TiO2	45.13	20.15	45.75	15.03	46.55	15.37
Al2O3	0.16	1.93	0.18	2.53	0.06	2.61
Cr2O3	0.03	0.00	0.08	0.00	0.01	0.01
Fe2O3	13.73	28.81	10.18	35.57	11.90	35.98
FeO	35.71	47.11	35.85	42.04	36.78	42.97
MnO	0.83	0.78	0.89	0.68	0.83	0.62
MgO	2.28	1.56	2.49	1.36	2.38	1.38
Total	97.89	100.39	95.46	97.35	98.52	99.10

Sample ID	AC22 ilm 3	AC22 mt3	AC22 ilm 4	AC22 mt 4	AC22 ilm 6	AC22 mt 6
Host	**PreCald RD**	**PreCald RD**	**PreCald RD**	**PreCald RD**	**PreCald RD**	**PreCald RD**
SiO2	1.14	0.08	0.02	3.00	0.00	0.15
TiO2	45.86	19.84	44.68	19.62	43.34	14.57
Al2O3	0.21	1.85	0.15	2.78	0.22	2.73
Cr2O3	0.02	0.04	0.00	0.03	0.06	0.05
Fe2O3	9.89	27.26	12.13	20.89	15.11	36.33
FeO	36.60	46.07	34.25	50.09	31.77	40.48
MnO	0.91	0.70	0.97	0.70	0.88	0.61
MgO	2.86	1.51	2.79	1.70	3.55	2.12
Total	97.49	97.34	94.98	98.80	94.93	97.04

Sample ID	ACAF1A8 ilm	ACAF1A8 mt	ACAF1E1 ilm1	ACAF1E1 mt1	AC36b ilm1	AC36b mt1
Host	**CFE and**	**CFE and**	**CFE and**	**CFE and**	**CFE and**	**CFE and**
SiO2	0.03	0.12	0.13	0.09	0.00	0.00
TiO2	43.54	10.99	12.48	12.10	45.34	11.61
Al2O3	0.23	2.22	4.00	3.81	0.24	2.11
Cr2O3	0.00	0.00	0.02	0.05	0.00	0.06
Fe2O3	16.94	43.81	41.84	41.68	16.91	44.51
FeO	31.71	36.33	36.03	35.14	32.69	37.22
MnO	1.37	1.20	0.53	0.67	1.76	1.34
MgO	3.46	2.26	4.67	4.59	3.62	2.27
Total	97.28	96.92	99.70	98.13	100.56	99.11

Sample ID	AC36b ilm2	AC36b mt2	AC36a ilm2	AC36a mt2	AC36a ilm4	AC36a mt4	AC19 mt1
Host	CFE and	CFE and	CFE RD	CFE RD	CFE RD	CFE RD	U. Bk. Nose
SiO2	0.06	0.07	0.03	0.03	0.02	0.02	0.02
TiO2	43.48	11.29	42.49	11.66	44.46	11.52	43.20
Al2O3	0.27	2.16	0.20	2.19	0.23	2.20	0.29
Cr2O3	0.00	0.00	0.11	0.06	0.12	0.00	0.00
Fe2O3	18.42	42.53	16.84	44.33	16.86	43.51	16.56
FeO	31.38	36.41	30.83	37.56	32.25	37.12	30.73
MnO	1.55	1.13	1.34	1.30	1.48	1.19	1.03
MgO	3.56	2.15	3.45	2.20	3.60	2.13	3.99
Total	98.72	95.74	95.28	99.34	99.02	97.70	95.81

Sample ID	AC19 ilm1	AC14 ilm2	AC14 mt2	AC14 ilm3	AC14 mt3	AC14 ilm4	AC14 mt4
Host	U. Bk. Nose	L. Bk. Nose	L. Bk. Nose	L. Bk. Nose	L. Bk. Nose	L. Bk. Nose	L. Bk. Nose
SiO2	0.09	0.08	0.04	0.05	0.07	0.00	0.01
TiO2	13.06	44.29	14.35	45.30	14.62	45.39	15.44
Al2O3	2.47	0.24	2.02	0.21	2.13	0.21	2.05
Cr2O3	0.04	0.03	0.00	0.00	0.00	0.00	0.01
Fe2O3	39.22	13.25	35.19	13.30	36.50	13.77	36.44
FeO	37.60	32.91	38.74	33.70	40.02	33.53	40.77
MnO	1.03	1.32	1.00	1.28	1.07	1.32	1.32
MgO	2.76	3.17	2.09	3.26	2.01	3.29	2.15
Total	96.27	95.29	93.43	97.10	96.42	97.51	98.19

Appendix E: Outcrop Locations and Notes

Additional field data not explicitly mentioned in the text. Section letter designations correspond to the lettered locations on figure 2. Data collected July 1997, June 1998, and August 1999.

Section A: *57.25N, 158.37W*

Mixed ignimbrite in beach lagoon 18 mile north of Pt. Heiden. 1.5 meters exposed primary material. Segregation pipes present throughout. Maximum rhyodacite: 37 cm; maximum andesite: 28 cm

Section B: *56.90N, 158.43W*

Gradual transition from rhyodacite to mixed to andesite ignimbrite in Barabara Creek. Andesite portion contains both juvenile and lithic blocks up to 50 cm. Rhyodacite and mixed portions are lithic poor. Maximum rhyodacite: 30 cm

Section C: *56.82N, 158.45W*

Andesite ignimbrite on western flanks of the caldera, south of Birthday Creek. Very fine grained, contains thin (10 cm) lenses of rhyodacitic lapilli, and zones of lithic enrichment. 8 meters of ignimbrite overlain by 2 meters of sandy stream deposits. Rare andesite blocks up to 50 cm.

Section D: *57.03N, 158.05W*

Rhyodacite ignimbrite overlain by agglutinated andesite ignimbrite. Pumice at base of rhyodacite is equant, but becomes more lenticular towards the top of the unit. Andesite is dense and glassy.

Section E: *56.93N, 158.26W*

Dark gray glassy rhyodacitic lava flow on northwest flank of caldera. No lithic breccia present on top of the flow.

Section F: *56.94N, 158.01W*

Dark gray, glassy rhyodacite lava flow on northeast flank of caldera. Overlain by lithic breccia and postcaldera tephras.

Section G: *56.92N, 158.07W*

Glassy precaldera rhyodacite lava dome, exposed in caldera walls near the rim. Flow banding and joints at steep angles suggest the exposure represents a vent.

Section H: *56.88N, 158.20W*

Moderately welded precaldera andesite ignimbrite (Aniakchak I) in Birthday Creek at caldera rim. Juvenile clasts are flattened. Vertical joints from base to top; overlain by lithic breccia. Top of ignimbrite is eroded. Maximum andesite: 1 m

Section I: *56.86N, 158.26W*

Both Aniakchak I and CFE ignimbrites present in Birthday Creek valley walls. Aniakchak I and CFE are separated by an indurated lahar deposit. CFE rhyodacite maximum size: 30 cm. maximum lithic size in CFE rhyodacite ignimbrite is ~5 cm. CFE andesite is commonly agglutinated with clasts larger than 1 m.

Section J: *56.84N, 158.31W*

Moderately indurated andesite ignimbrite in Birthday Creek, near 600 ft. elevation contour. Four meters vertically from the stream there is a horizon of large andesite and lithic blocks. Maximum andesite: 50 cm. Maximum lithic: 1 m. Top of the outcrop is ~ 80 to 90 % lithic blocks.

Section K: *56.84N, 158.19W*

Rhyodacite ignimbrite near head of Plenty Bear Creek, ~30 – 40 m thick. Maximum rhyodacite: 20 cm; maximum lithic: 5 cm. Overlain by andesite-bearing lithic breccia. Lithics in breccia are a meter or more in length; maximum andesite: 20 cm

Section L: *56.84N, 158.08W*

Rhyodacite ignimbrite at head of Wind Creek, west side of The Garden Wall, about 30 m thick. Overlain by andesite-bearing lag breccia. Maximum lithic: > 1 m; Maximum andesite: 30 cm.

Section M: *56.81N, 158.03W*

Andesite ignimbrite in Cub Creek, east side of The Garden Wall, about 15 m thick. ~1 m thick agglutinated layer of andesite at the top of the exposure. Contains scarce, very rounded rhyodacite lapilli, around 3 cm in diameter. Coarse grained precaldera lava beneath andesite ignimbrite.

Section N: *56.75N, 158.22W*

Andesite ignimbrite in Plenty Bear Valley, 8 km north of the Meshik River, 24 m thick. Maximum andesite up to 1 meter in upper 2 meters of ignimbrite. top two meters may be a separate flow unit. Lower portion contains a small percentage of small rounded rhyodacite clasts.

Section P: *56.71N, 158.04W*

Mixed ignimbrite exposure east of Shoe Creek, at the base of the Aleutian Mountain Range, 14 m thick. Maximum andesite: 23 cm; maximum rhyodacite: 48 cm; maximum lithic 16 cm.

Section Q: *56.69N, 158.07W*

Mixed ignimbrite exposure west of Shoe Creek, at the base of the Aleutian Mountain Range, 22 m thick.

Section R: *56.61N, 158.24W*

Small outcrop in Blue Violet Creek 7.5 km south of Meshik River. 40 cm thick series of thin, fine ash layers at creek level, overlain by rhyodacite ignimbrite. 1.5 m of rhyodacite ignimbrite exposed. Overlain by mixed ignimbrite, but contact is covered. Total thickness is 11 m thick.

Section S: *56.96N, 157.92W*

Thick section of massive mixed ignimbrite, overlain by andesite ignimbrite along Lava Creek, just west of Jaw Mountain. The two ignimbrite units are separated by a 1 m thick lithic breccia layer. Large cliffs in the ignimbrite are formed at outside of bends in the creek. Immediately to the south, an incipiently welded layer of mixed ignimbrite forms a spectacular waterfall in Lava Creek

Section T: *56.79N, 157.94W*

Thin layer (~3 m thick) of andesite ignimbrite near west margin of Meshik Lake. Found in a site excavated by National Park Service archaeological party (lead by Richard Van der Hoek). Maximum andesite: 30 cm; maximum rhyodacite: 3 cm. Overlain by 1.5 to 2 meters of postcaldera tephras.

Section U: *56.78N, 157.80W*

Mixed ignimbrite in Albert Johnson Creek, 5 km east of Meshik Lake. Exposure shows mixed ignimbrite has filled a pre-existing channel. Underlain by several precaldera tephras and soils.

Section V: *56.68N, 157.88W*

Valley-filling mixed ignimbrite deposit on Pacific shoreline in Kujulik Bay. Overlies a cobble rich mud flow deposit. Most of the exposure contains large pumice blocks (maximum pumice: 30 cm, maximum lithic: 10 cm). Two thinner layers near the top of

progressively smaller pumice fragments. Overlain by lithic-rich andesite ignimbrite, 1 m thick; maximum andesite 4 cm, maximum lithic: 3 cm.